12th DELTA User Meeting

&

Annual Report 2016

Dortmund
30. November 2016

Edited by C. Sternemann, R. Wagner,
D. Lützenkirchen-Hecht (2016)

November 2016

Preface

Dear reader, dear colleague,

at the time DELTA went into user operation in 2004/2005, only 5 beamlines were in operation. Since then, a dynamic development of the machine and the installed beamlines and instruments took place. The recent restart of BL1 with a new lithography scanner, the implemantation of a setup for micro-tomography at BL2 (see page 13) as well as the finalized ordering and purchase of a new wiggler insertion device for the hard X-ray beamlines 8, 9 and 10 together with the recent progresses at the short pulse facility are indicators for the ongoing improvements and renewals of the synchrotron source. In this context, a workshop for the future development of DELTA took place in July this year, and there was a general agreement to continue and broaden the research activities here.

In this context, it is noteworthy to mention that the international visibility of the research carried out at DELTA is not only documented in peer-reviewed publications and numerous conference talks and posters, for example at the International Conference on Surface X-ray and Neutron Scattering in Stony Brook (USA), the European Powder Diffraction Conference in Bari (Italy) or the International Particle Accelerator Conference IPAC 201 Busan (Korea) to highlight just a few, but also in the increasing number of foreign scientists who conducted their experiments at DELTA. In the past year, we have had guests from Slovenia, Croatia, Poland, Switzerland, the UK, Japan as well as the first African user from Nigeria. Those cooperations are also expressing the huge demand for synchrotron measurements worldwide, and justify the investments for the operation of the machine and the beamlines.

Thus we would like to thank for the manifold support of DELTA by the involved universities and research institutions, the different funding agencies and also the local government. We are looking forward to the upcoming beamtime periods, hoping that they will be as productive and successful as during the past year!

Christian Sternemann, Ralph Wagner & Dirk Lützenkirchen-Hecht

Contents:

Instrumentation

Status of and future plans for DELTA and its short-pulse facility

P. Ungelenk*

on behalf of the DELTA machine group:
A. Althaus, W. Brembt, B. Büsing, G. Dahlmann, T. Dybiona, A. Erpelding, J. Friedl, P. Hartmann, B. Hippert, B. Isbarn, S. Khan, V. Kniss, P. Kortmann, S. Kötter, D. Krieg, N. Lockmann, C. Mai, A. Meyer auf der Heide, R. Niemczyk, B. Riemann, D. Rohde, H.-P. Ruhl, D. Schirmer, G. Schmidt, T. Schulte-Eickhoff, G. Shayeganrad, M. Sommer, M. Suski, and T. Weis

Center for Synchrotron Radiation (DELTA), TU Dortmund University, Germany

DELTA[1] is a 1.5-GeV electron storage ring operated as a synchrotron light source by the TU Dortmund University. Distributed along the 115-m circumference (Fig. 1), synchrotron radiation is provided by bending magnets, a superconducting asymmetric wiggler (SAW), a permanent-magnet undulator (U55), and an electromagnetic undulator (U250). Since 2011, a short-pulse facility for coherent sub-picosecond light pulses in the vacuum-ultraviolet (VUV) and Terahertz (THz) regimes has been established[2,3]. This article reports the status of and future plans for DELTA and its short-pulse facility with emphasis on new results and developments since the last DELTA user meeting in November 2015[4].

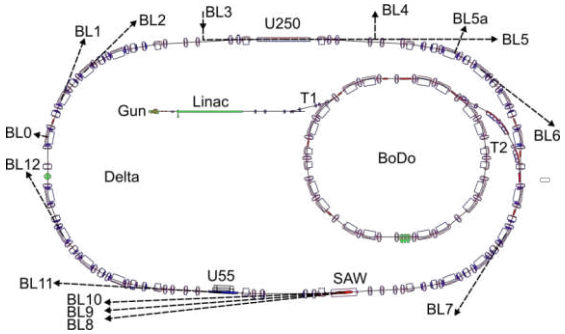

Figure 1: Layout of DELTA (see text for details; source: [5], modified).

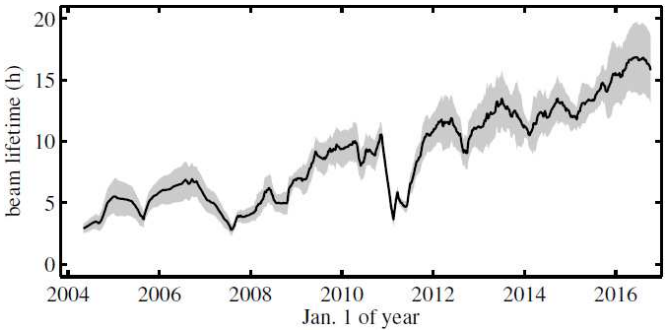

Figure 2: Beam lifetime at 100 mA averaged over 20 days. The FWHM of the fluctuations is indicated in grey.

The availability of DELTA (ratio of prospective to actual time of beamshutter clearance) during the first three quarters of 2016 amounts to 95.7 %, which is a significant increase compared to 2015 and 2014, respectively. Since the last venting of part of the storage ring in 2011, the beam lifetime (measured at 100 mA) has continuously increased from below 5 hours to an average of (16.5 ± 3.0) hours in 2016 (Fig. 2) – mainly due to radiation-induced cleaning of the vessel surface but also due to an improved vertical alignment of the storage ring magnets. A new 7-T wiggler with 10 periods was ordered, which will replace the aging SAW leading to increased intensities and photon energies at beamlines BL8, BL9, and BL10. The new wiggler requires an upgrade of the storage-ring RF system, and a second RF cavity as well as a corresponding solid-state amplifier was also ordered.

Following the suggestion of the Machine and Experiments Committee (MEC), a workshop on the future of DELTA was held in Dortmund on July 15, 2016. The near future will be dominated by the wiggler and RF upgrade as well as by the implementation of the EEHG scheme for the short-pulse facility (see below). Looking further ahead (10 to 20 years), ideas for a competitive and innovative future accelerator at the DELTA site were collected, one of them being a linear accelerator serving a free-electron laser (FEL). Such a facility could be built in parallel to the continued operation of DELTA and would allow for femtosecond FEL pulses in the extreme UV range. In addition, low-energy electron bunches could be used for time-resolved electron diffraction and to study advanced accelerator concepts such as dielectric wakefield acceleration.

The current short-pulse facility[2,3] at DELTA is based on the so-called coherent harmonic generation (CHG) scheme[6,7]. Here, 50-fs light pulses from an 800-nm short-pulse laser system are employed to modulate the electron energy and density of a short central slice of the 100-ps electron bunches in a first section of the undulator U250 (Fig. 1) leading to a series of microbunches. These microbunches coherently emit an ultrashort light pulse in the second half of the U250, which is tuned to a harmonic of the laser wavelength. The off-energy electrons then vacate the central slice when passing the magnet lattice of the storage ring, which leads to the coherent emission of broadband pulses in the THz regime a few meters downstream of the U250.

* peter.ungelenk@tu-dortmund.de

With a routine operation of the short-pulse facility on about 50 days per year, DELTA currently is the only storage ring offering ultrashort and coherent pulses in the VUV range on a regular basis. CHG pulses at 400 nm (3 eV), 200 nm (6 eV), and 133 nm (9 eV) are routinely generated and detected at the diagnostics beamline BL4 or VUV beamline BL5, and pulses at a minimum wavelength of 80 nm (15 eV) were observed at BL5. On several occasions, CHG and THz pulses were generated during standard user operation of DELTA by injecting a high-current single bunch on top of the standard multibunch fill of the storage ring (hybrid mode). Previously observed effects of an RF phase modulation, which is employed during user operation to damp beam instabilities and increase the beam lifetime, on the CHG and THz signals were analyzed based on the Hamiltonian theory of beam dynamics[8,9].

The spectra of 400-nm and 200-nm CHG pulses under variation of the laser and undulator parameters were studied extensively at the in-air diagnostics beamline BL4 employing a Czerny-Turner-type monochromator followed by an avalanche photodiode or a fast-gated intensified CCD (iCCD) camera[10]. With the recent installation of an evacuated chamber at BL4, first light at 133 nm was observed on a scintillating screen[11]. A new second- and third-harmonic generation unit suitable for vacuum has been prepared[12], which will soon allow a more efficient conversion of the seed laser wavelength before the laser-electron interaction, leading to increased CHG pulse energies and improved quality at higher harmonics.

A first successful pump-probe experiment at BL5 was recently performed employing a fraction of the seed pulses to excite a copper sample and advanced/delayed CHG pulses at 133 nm (9 eV) to probe the temporal evolution of the induced space charge effect on photoelectron spectroscopy[13].

The instrumentation at the THz beamline BL5a has been extended by several time-resolving detectors and two Fourier transform spectrometers, and detailed studies of the THz spectra and the temporal evolution of the THz pulses over several revolutions of the modulated electron bunch in the storage ring were performed[14,15]. A permanent and optimized setup for generating narrowband coherent THz radiation pulses is currently under construction following a first successful test and a first user experiment[16,17]. A fiber laser system is currently under commissioning and a corresponding electro-optical far-field detection setup is under preparation[18], which will allow to directly study the electric field of the THz pulses.

In order to reach even shorter wavelengths at the DELTA short-pulse facility, an upgrade employing the so-called echo enabled harmonic generation (EEHG) scheme[19] is under preparation[20]. Using two new undulators and magnetic chicanes in addition to the existing U250, a more complex laser-induced density modulation in the central slice of the electron bunch (see above) will contain frequency components at much higher harmonics allowing to generate ultrashort coherent pulses at even shorter wavelengths. In order to create a 20-m straight section in the northern area of DELTA for these additional components, existing 3° and 7° bending magnets will be replaced by 10° bending magnets (Fig. 3). A new magnetic layout and corresponding optics have been found[21,22] as well as a concept for the efficient use of existing vacuum chambers[23] in addition to new undulator and dipole chambers. Both new undulators and corresponding power supplies have arrived, and the accuracy of the magnetic field was studied using a new test bench equipped with a hall probe[24]. Vacuum chambers for the undulators were ordered, and a possible design for one of the new chicanes was recently worked out[25].

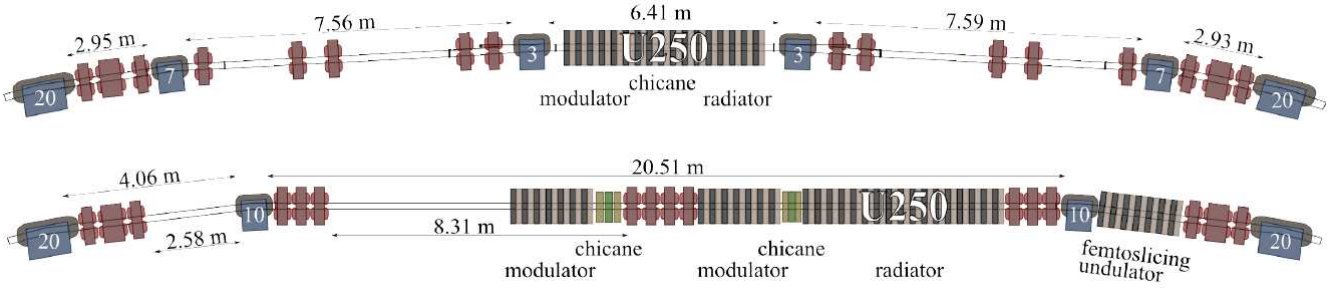

Figure 3: Present (top) and future (bottom) magnetic layout of the short-pulse facility in the northern area of DELTA [21].

In summary, the beam availability and lifetime at DELTA during the past year were more than satisfactory, and continued studies and optimization of the laser-electron interaction, the CHG, and the THz pulses were performed at the DELTA short-pulse facility. Preparations for a new superconducting wiggler, an upgrade of the storage-ring RF system, and the implementation of EEHG at the short-pulse facility are progressing at a good pace. With the workshop on the future of DELTA, fruitful discussions about the mid- and long-term future have begun, aiming at strengthening the competitive position of DELTA in the areas of photon science and accelerator physics as well as of education in both fields.

References

[1] D. Schirmer et al., *Status of the Synchrotron Light Source DELTA*, in Proceedings of the 9th European Particle Accelerator Conference, 2296 (Lucerne, 2004).

[2] S. Khan et al., *Coherent Harmonic Generation at DELTA: A New Facility for Ultrashort Pulses in the VUV and THz Regime*, Synchrotron Radiation News 24, 18 (2011).

[3] S. Khan et al., *Generation of Ultrashort and Coherent Synchrotron Radiation Pulses at DELTA*, Synchrotron Radiation News 26, 25 (2013).

[4] C. Sternemann et al., Proceedings of the 11th DELTA User Meeting (TU Dortmund, 2014).

[5] D. Schirmer, *Synchrotron radiation sources at DELTA*, DELTA Int. Rep. 001-05 (University of Dortmund, 2009).

[6] R. Coisson and F. de Martini, *Free-Electron Coherent Relativistic Scatterer for UV Generation*, in Free-Electron Generators of Coherent Radiation, Physics of Quantum Electronics 9 (Addison-Wesley Publishing Company, Massachusetts, 1982).

[7] R. Prazeres et al., *Coherent harmonic generation in the vacuum ultraviolet spectral range on the storage ring ACO*, Nuclear Instruments and Methods in Physics Research Section A 272, 68 (1988).

[8] M. Jebramcik et al., *Coherent Harmonic Generation in the Presence of Synchronized RF Phase Modulation at DELTA*, in Proceedings of the 7th International Particle Accelerator Conference, 2847 (Busan, 2016).

[9] M. Jebramcik, *RF Phase Modulation in the Context of Coherent Harmonic Generation at the DELTA Storage Ring*, master's thesis (TU Dortmund, 2016).

[10] S. Khan et al., *Spectral Studies of Ultrashort and Coherent Radiation Pulses at the DELTA Storage Ring*, in Proceedings of the 7th International Particle Accelerator Conference, 2851 (Busan, 2016).

[11] F. Götz, *Verbesserung der Diagnosemöglichkeiten an der Kurzpulsquelle bei DELTA*, master's thesis (TU Dortmund, 2016).

[12] N. Lockmann, master's thesis (TU Dortmund, in preparation).

[13] M. Plötzing et al., *Time- and angle-resolved photoemission experiments on Cu(111) at BL5*, these proceedings (TU Dortmund, 2016).

[14] P. Ungelenk, *Generation and Detection Schemes for Laser-Induced Coherent Terahertz Radiation at the Electron Storage Ring DELTA*, dissertation (TU Dortmund, 2015).

[15] C. Mai et al., *Time-resolved Spectral Observation of Coherent THz Pulses at DELTA*, in Proceedings of the 7th International Particle Accelerator Conference, 105 (Busan, 2016).

[16] J. Raasch et al., *Tunable narrowband THz radiation for the investigation of the frequency-dependent picosecond response of YBCO detectors*, in Proceedings of the 10th DELTA User Meeting, 5 (TU Dortmund, 2014).

[17] P. Ungelenk et al., *Continuously tunable narrowband pulses in the THz gap from laser-modulated electron bunches in a storage ring*, Physical Review Accelerators and Beams (manuscript submitted for publication).

[18] R. Niemczyk, *Konstruktion eines Aufbaus für elektrooptische Fernfeld-Messungen an der Terahertz-Strahllinie bei DELTA*, master's thesis (TU Dortmund, 2016).

[19] D. Xiang and G. Stupakov, Echo-enabled harmonic generation free electron laser, Physical Review Special Topics – Accelerators and Beams 12, 030702 (2009).

[20] S. Hilbrich et al., *Plans for an EEHG-based Short-Pulse Facility at the DELTA Storage Ring*, Proceedings of the 37th International Free Electron Laser Conference, 363 (Daejeon, 2015).

[21] S. Hilbrich, *Studies of the DELTA Lattice in View of a Future Short-Pulse Facility Based on Echo-Enabled Harmonic Generation*, master's thesis (TU Dortmund, 2015).

[22] R. Molo, dissertation (TU Dortmund, in preparation).

[23] F.H. Bahnsen, *Auslegung von Vakuumkomponenten für eine EEHG-basierte Kurzpulsquelle bei DELTA*, master's thesis (TU Dortmund, 2016).

[24] D. Zimmermann, *Aufbau eines Magnetmessstandes zur Feldvermessung von Undulatoren bei DELTA*, master's thesis (TU Dortmund, 2016).

[25] E. Schneider, *Aufbau Auslegung einer elektromagnetischen Schikane für die EEHG-Kurzpulsquelle bei DELTA*, bachelor thesis (TU Dortmund, 2016).

The new Lithography Scanner of BL1 at DELTA

Jennifer Bolle[1], Michael Paulus[1], Christian Sternemann[1], Georg Jülicher[1], Thorsten Witt[1], Joachim Schulz[2], Thomas Beckenbach[2], Pascal Meyer[3] and Metin Tolan[1].
[1]Fakultät Physik/DELTA, TU Dortmund, D-44221 Dortmund, Germany
[2] microworks GmbH, Schnetzlerstr 9, 76137 Karlsruhe, Germany
[3] Karlsruhe Institute of Technology, Institute of Microstructure Technology, Hermann-von-Helmholtz-Platz 1,76344 Eggenstein-Leopoldshafen

---

Deep x-ray lithography is a method to produce microstructures with a lateral resolution in the µm-range. It is a part of the so called LIGA process. The LIGA (**Li**thographie, **G**alvanik, **A**bformung) process features three steps: lithography, electroplating and molding.
X-ray lithography uses shadow projection to transfer an absorber (mask) pattern into a thick x-ray sensitive polymer [1]. The polymer (resist) is deposited on a substrat, e.g. silicon or graphite. The x-ray mask consists of a gold absorber on an x-ray transparent membrane, e.g. titanium or graphite. The exposed areas of the polymer change the molecular weight by a chemical process. After development, the exposed area (positive resist) or the unexposed area (negative resist) is removed. Then the metal part is created via electroplating, which then can be used in several ways, for example for the last step of the LIGA-process, the molding [2]. This method offers a way to fabricate high precision micromechanical parts.
A new x-ray lithography scanner was implemented at the BL 1. The scanner (DEX01) consists of a control unit, the working chamber and a filter system. A picture of the working chamber is shown in Figure 1 (a). A vacuum pump evacuates the working chamber within ten minutes to a pressure of 10^{-3} mbar. A beryllium entrance window limits the synchrotron beam horizontally to the size of the 4 inch wafer. The filter system consists of five pneumatic cylinders, which move the respective filters into the beam. One filter was converted to a beamshutter, which can be controlled via the control unit. The filter consists of a lead strip and protects the sample from radiation befor the exposure is started. The exposure dose is calculated with the DoseSim

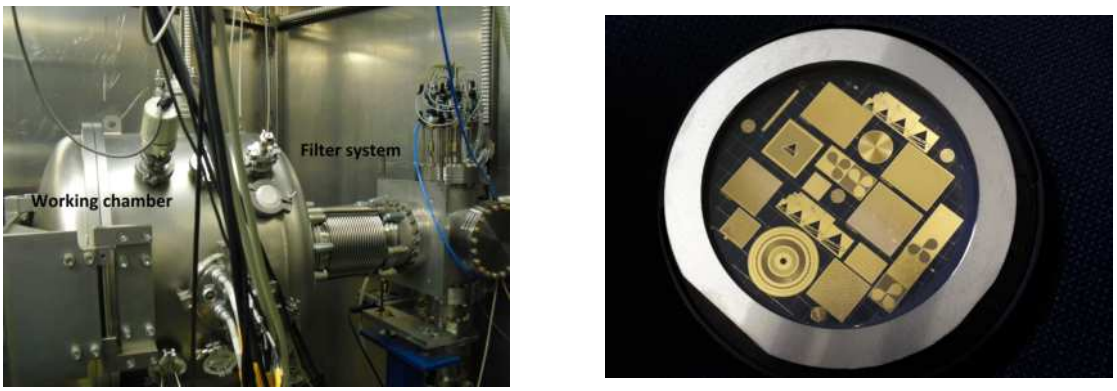

Figure 1: (a) Working chamber and filter system, (b) Mask consists of a goldabsorber and a graphite membrane

program [4]. A motor is used to move the wafer and mask vertically into the synchrotron beam. After the exposure the wafer is baked out with a PEB (post exposure bake) program. This

initiates the cross linking of the polymer.
In the test exposures the optimal exposure parameters were determined. We exposed testwafers at different conditions (e.g use of different filters, different bottom dose and investigation of thermal expansion by using a water cooling system). First, the difference between the structure quality of an exposure with a nickel filter (10 µm), an aluminum filter (30 µm) and the optimal bottom dose is probed. Here, a new mask with a 20 µm gold absorber of a 200 µm graphite membrane is used (fig. 1 (b)). The first exposures with a resist named mrx-50 (a negative resist, which is based on SU-8) on silicon wafers were performed successfully. The exposure with a bottom dose of 80 J/cm^3 leads to the best results. The exposuretime depends on the used filter and the resist thickness, but is typically near 15 minutes. The exposure with the aluminum filter shows after the electroplating resist residues.
The exposure with the nickel filter results in high quality structures (fig. 2). The structure exhibits sharp edges, but the wall of the structures shows high roughness (fig. 2 (a)). This is due to the mask membrane (graphite) [3]. The investigation of the thermal expansion revealed

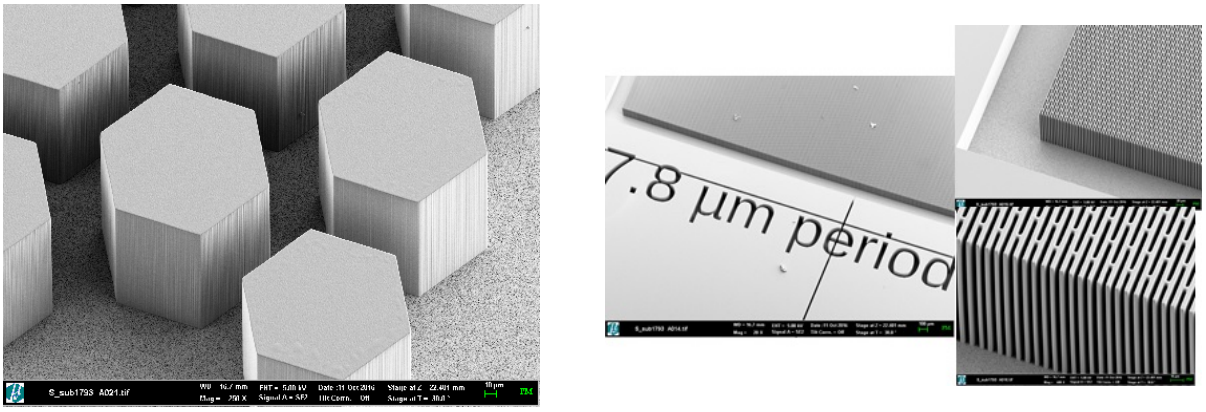

Figure 2: (a) SEM image of a structured area, (b) SEM image of a grid with a 7.8 µm period

that structure quality is not affected. The lithography scanner at BL 1 is ready to produce high quality microstructures with industrial standard.
We acknowledge the Delta machine group for providing synchrotron radiation and technical support and thanks to BESSY, Berlin, for the provided Lithography Scanner.

References

[1] G Feiertag et al. „Fabrication of photonic crystals by deep x-ray lithography“. In: Applied Physics Letters 71.11 (1997), S. 1441–1443.
[2] E.W. Becker et al. „Fabrication of microstructures with high aspect ratios and great structural heights by synchrotron radiation lithography, galvanoforming, and plastic moulding (LIGA process)“. In: Microelectronic engineering 4.1 (1986), S. 35–56.
[3] G Aigeldinger et al. „Influence of mask substrate materials on resist sidewall roughness in deep X-ray lithography“. In: Microsystem Technologies 14.2 (2008), S. 277–286.
[4] Pascal Meyer. „Fast and accurate X-ray lithography simulation enabled by using Monte Carlo method. New version of DoseSim: a software dedicated to deep X-ray lithography (LIGA)“. In: Microsystem technologies 18.12 (2012), S. 1971–1980.

Development of a Scanning Reflection X-ray Microscope (SRXM)

A. Schümmer[1], M. Gilbert[1], C. Jansing[1], H.-Ch. Mertins[1],
R. Adam[2], C. M. Schneider[2], L. Juschkin[3], U. Berges[4]

[1] University of Applied Sciences, Münster Stegerwaldstraße 39, 48565 Steinfurt, Germany
[2] Forschungszentrum Jülich, Wilhelm-Johnen-Straße, 52428 Jülich, Germany
[3] Rhein Westfälische Technische Hochschule Aachen, Templergraben 55, 52062 Aachen, Germany
[4] DELTA / TU Dortmund Maria-Goeppert-Mayer-Straße 2, 44227 Dortmund

Theoretical and experimental work started within a new project of a scanning reflection x-ray microscope (SRXM) designed for beamline 12 at DELTA. The operation in reflection mode will allow the study of surfaces and interfaces even of thick samples. It also will enable imaging of magnetic domains in buried layers exploiting magneto-optical reflection spectroscopy like XMLD and XMCD. Working at the DELTA beamline 12 in the extreme ultraviolet (EUV) regime, EUV synchrotron radiation near the 3p absorption edges of 3d transition metals about 50eV – 70eV, results in sufficient reflected intensities, which are about two orders of magnitude larger than those at the respective 2p edges due to the higher reflectivity in the EUV regime [1, 2].

The setup of our projected SRXM shown in Fig 1.It consists of a high-resolution zone plate that focuses the beam on a small spot of 250 nm diameter on the surface of the sample, more details about the mechanical properties see Tab.1. A central beam stop (CBS) is implemented in the zone plate to block zero order radiation. In contrast to STXM the sample is illuminated in gazing incidence (Tab. 1). This angle allows magneto-optical reflection spectroscopy as T-MOKE, L-MOKE or XMLD. The contrast depends on the orientation between the light's linear polarization vector and the magnetization direction. This will enable the detection of magnetic domains of ferromagnetic and anti-ferromagnetic materials.

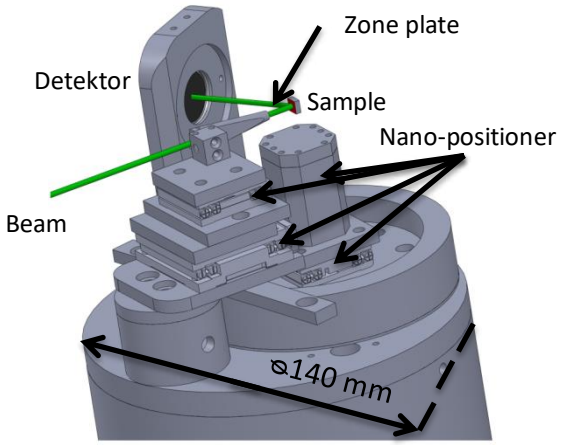

Fig. 1 Setup of SRXM

Property	Scanning horizontal	Scanning vertical	Re focusing	Angle to surface normal
Value	-/+10 mm in 50nm Steps	+12 mm In 100 nm Steps	0-20mm in 50 nm Steps	0°-45° (1°accurancy)

Tab 1 – Mechanical properties of the designed SRXM

As High resolution EUV optic a zone plate with a resolution of 250 nm will be used. A zone plate structure has been calculated with respect to the energy range (40-70 eV) and energy resolution (400) of BL12, resulting in a zone plate of 0.4 mm diameter with a focal length of 5 mm (@60eV) and an outermost zone width of 250 nm. A shift in energy results in a shift in focal length and depth of focus (Tab 2).

λ [nm]	F [mm]	DOF [µm]
17(70)	5,88	14,7
20(60)	5	12,5
25(50)	4	10,0

Tab 2: Variation of DOF and focal length with respect to the wavelength(E/ΔE 400)

Two types of zone plates are considered the Structure material is either PMMA on a 50-200nm thin Si_3N_4 window. With gold the zone structure shows low transmission (Fig 2,4)which results in an efficiency of 10%. For zone structures of PMMA transmission is increased (Fig 2) and phase shift is the dominating process (Fig 3) which depends on structure thickness and energy. To obtain a phase shift near 180° a thickness of 160nm PMMA is chosen, resulting in efficiency values (Fig 4) higher than for gold structures. The disadvantage of PMMA structures over gold structures is the higher ageing process of PMMA due to absorption of radiation, resulting in shorter lifetimes. This will be analyzed by exposing PMMA layers to the BL 12 beam.

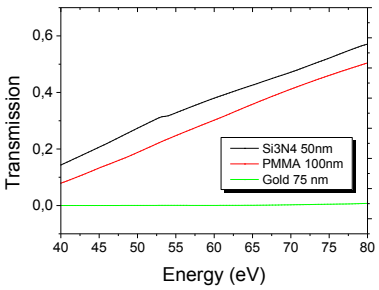

Fig. 2: Transmission of different AU, PMMA and Si_3N_4 in the range of 40.80eV

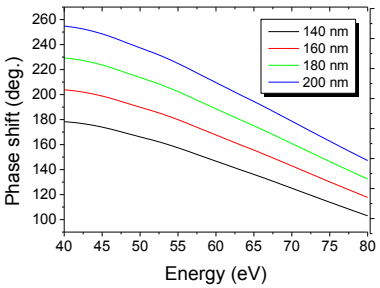

Fig. 3: Phase shift by PMMA of different thicknesses

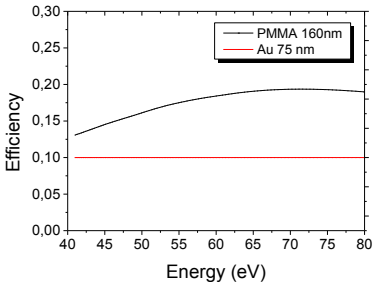

Fig. 4: Diffraction efficiency of the 1. order Au and a PMMA grating

Challenges

Despite the relatively high reflectance of metallic samples in the EUV a high photon flux is needed. Therefore, the scanning method has been selected since a smaller photon flux is required compared to the full field imaging. High resolution zone plates with a spatial resolution near 250 nm result in short focal length of about 4-6 mm in the EUV region. This limits the mechanical operation range of samples and detectors. Aberrations due to the incidence angles change the shape and the size of the focus spot on the sample. Also the zone plate fabrication is challenging due to the fragile samples and unknown parameters like PMMA aging.

Outlook

The next step will be the assembling of all microscope components at BL12. Within the next year the PMMA lifetime will analyzed and different zone plates tested, the resolution of the microscope will be determined and with these data new optimized zone plates will be fabricated.

[1] M. F. Tesch, M. C. Gilbert, H.-Ch. Mertins, D. E. Bürgler, U. Berges, and C. M. Schneider "X-ray magneto-optical polarization spectroscopy: an analysis from the visible region to the x-ray regime"., Applied Optics 52, 4294-4310 doi: 10.1364/AO.52.004294 (2013)

[2] H.-C. Mertins, S. Valencia, A. Gaupp, W. Gudat, P.M. Oppeneer; C.M. Schneider „Magneto-optical polarisation spectroscopy with soft X-rays" Appl. Phys. A80,1011-1020 (2005)

[3] Greg Denbeaux, Peter Fischer, Farhad Salmassi, Kathleen Dunn, James Evertsen „Reflection Mode Imaging with High Resolution X-ray Microscopy" Proc. 8th Int.Conf. X-ray Microscopy IPAP Conf. Series 7 pp.375-376 (2006)

[4] Settimio Mobilio, Federico Boscherini, Carlo Menengihini „Synchrotron Radiation" Springer ISBN 978-3-642-55314-1 (2015)

[5] The Center for x-ray Optics "http://www.cxro.lbl.gov/"

Commissioning of a high temperature heater cell for in-situ ReflEXAFS studies of steel surfaces under variable reductive gas atmospheres

B. Bornmann[1], D. Wulff[2], R. Wagner[1], D. Lützenkirchen-Hecht[1], K. Möhwald[2], R. Frahm[1]

[1] Fakultät 4 – Physik, Bergische Universität Wuppertal, Gaußstraße 20, 42119 Wuppertal.
[2] Institut für Werkstoffkunde, Leibniz Universität Hannover, Bereich Füge- und Oberflächentechnik (FORTIS), Stockumer Str. 28, 58453 Witten.

High temperature brazing is conducted at temperatures T > 900°C and is preferably done in a conveyor belt furnace. Here the solder only wets the workpiece and forms stable bonds if there is no oxide layer on the surface. Therefore it is crucial to choose a reductive gas atmosphere and temperature in the furnace. Up to now this is usually done with a mixture of nitrogen and 4% hydrogen as a reducing agent at T ≈ 1000°C. However, it is preferred to reduce the amount of expensive reductive gases and to reduce the temperature in order to lower the stress in the soldered parts. Lately, the use of monosilane (SiH_4) in the ppm range instead of hydrogen was introduced and showed promising results [1, 2]. For this a fundamental understanding of the surface chemistry and structure is necessary to optimize the brazing process.

In order to allow in-situ analysis of surface characteristics with EXAFS in reflection and fluorescence as well as XRD, a high temperature cell was constructed (see Fig. 1). It consists of a vacuum chamber with a base pressure of p ≈ 10^{-6} mbar to minimize contaminations. It contains a boron nitride/pyrolytic graphite heater with Nb shielding which accepts cylindric samples of about 6 mm height and a diameter of up to 20 mm. All components close to the hot part of the system are chosen to withstand an oxidizing (N_2 6.0) and reductive atmosphere (N_2 + SiH_4) at T < 1200°C. The gas inlet on the top of the chamber directs the gas flow to the sample surface. The gas outlet on the bottom conducts the processed gas over a lambda probe to measure the oxygen concentration. The gas composition is regulated via mass flow controllers from a mixture of nitrogen 6.0 and nitrogen 5.0 with 0.5% of SiH_4 resulting in a SiH_4 concentration in the final mix of 1-5000 ppm. The system is controlled through a dedicated control rack inside the experimental hutch which can be fully controlled from outside.

After first tests in the laboratory, the system was installed at BL10 in October 2016 to perform commissioning under experimental conditions and record first spectra in November. The chamber was integrated into the diffractometer to adjust the height and angle of the sample surface relative to the beam. The samples were made from 1.4301 (X5CrNi18-10) and 1.4571 (X6CrNiMoTi17-12-2) stainless steel with surfaces polished to a roughness below 50 nm and Cr, Fe and Ni being the elements investigated. As for the soldering the chemical composition especially of the surface is important, the measurements could not be carried out in the conventional transmission mode but had to be done in reflection. By varying the angular position relative to the critical angle θ_c < 1° the penetration depth of the x-rays into the surface can be chosen from a few to some 100 nm. By that it is possible to receive the information provided by common XAFS (e.g. chemical composition, oxidation states) depending on the sample depth. First Fe K-edge spectra of the 1.4301 steel at T = 30°C and

700°C with 40 ppm SiH_4 in N_2 are shown in Fig. 2 which were measured with a beam size of 3 mm x 0.15 mm horizontally and vertically. $\theta = 0.326°$ with $\theta_c = 0.429°$ for Fe at 6.9 keV corresponds to a sampling depth of about 5 nm. While the spectrum at 30°C is somehow similar to the Fe_2O_3 reference, the spectrum at 700°C shows some shifts towards the Fe metal reference. However, both spectra consist of more than one component and Fe reduction at 700°C is not yet complete. A more detailed analysis of the measurements will be done soon. As the surface reflectivity vanishes at T > 700 °C measurements at higher T were not possible. A fluorescence detector as well as further improvements to the system will be added for higher temperatures and future beam times.

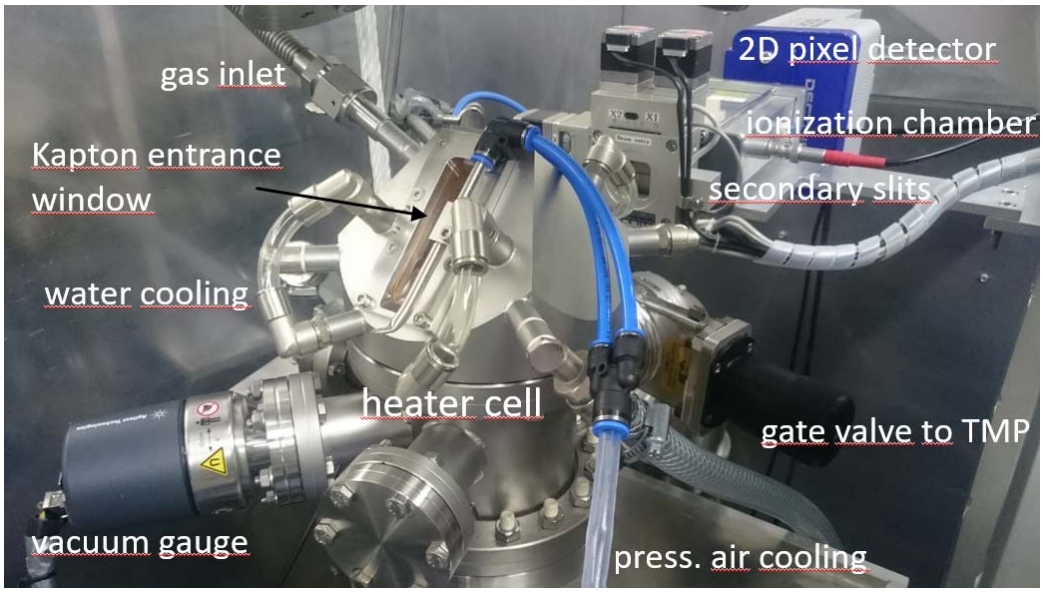

Figure 1: Heater cell inside the diffractometer with Kapton windows and cooling hoses. Secondary slits, an ionization chamber and a 2D pixel detector can be seen in the back.

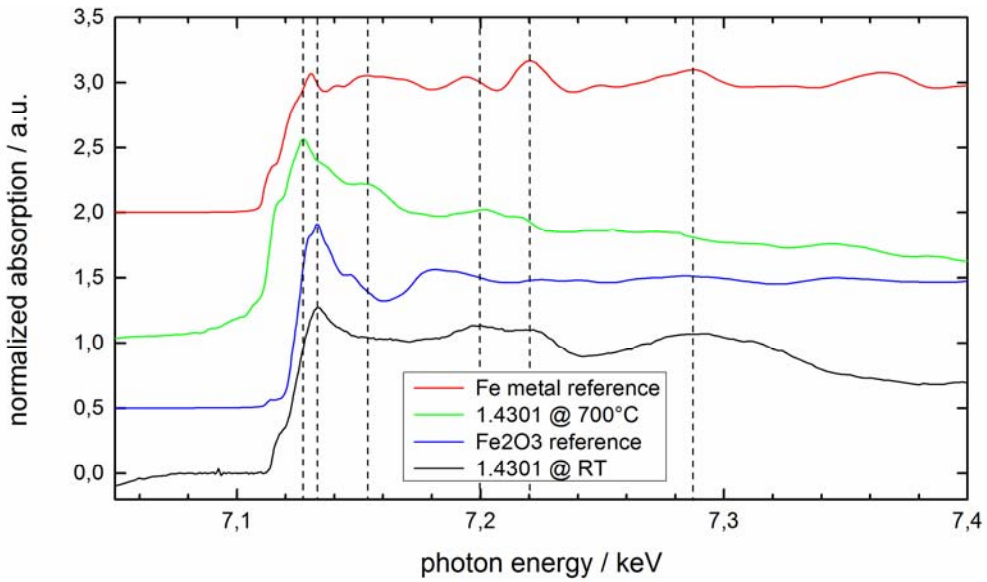

Figure 2: Normalized Fe K-edge spectra of the measured 1.4301 steel sample at T = 30, 700°C in comparison to Fe metal and Fe_2O_3 references.

References

[1] D. Lützenkirchen-Hecht et al., J. Mater. Sci. 49 (2014), 5454-5461.

[2] U. Holländer et al., Euro ECAA, Conference on Aluminium Science and Technology, Bremen, October 5 – 7, 2011, http://www.dgm.de/past/2011/ecaa.

Installation of a micro-tomography setup at beamline BL 2

Jan Nysar[1], Michael Paulus[1], Christian Sternemann[1], Felix Beckmann[2], Georg Jülicher[1], Thorsten Witt[1], Thorsten Brenner[1], Ulf Berges[1], Metin Tolan[1]

[1] Fakultät Physik/E1/DELTA, TU Dortmund, D-44221 Dortmund

[2] Institute of Materials Research, Helmholtz-Zentrum Geesthacht, D-21502 Geesthacht

Computed tomography (CT) is an imaging technique to investigate the inner structure of material without destroying the object or sample. It creates slice images through an object providing 3D information. For CT, usually X-radiation in the energy range of 10 keV to 150 keV is used to receive projections of the object from multiple angles. At microscopic scale it is called Micro Computed Tomography (µCT), which is an interesting method e.g. for materials science, biology (e.g. research on insects) or medical science.
The µCT apparatus, that is going to be operated at beamline BL 2, was previously used by HZG at beamline BW2 of the storage ring DORIS III at DESY in Hamburg. The basic instrument was built by the TU Dortmund and transferred to DESY in 1998 [Bec98].

The source of radiation at BL 2 is a bending magnet with a critical energy of 2.2 keV. The radiation passes through a vacuum window and a silicon absorber. So the low energy part of the spectrum is removed and x-ray radiation with sufficient intensity in the energy range of 10-35 keV is provided.
As in radiography, CT uses projections through an object, but from multiple angles in an 180° angular range. Each projection represents the line integrals of the attenuation coefficient along the path of incident photons through the irradiated object. Since different kind of matter have varying attenuation coefficients, the projections contain information about the material they went through. The photons, that passed through the sample, are then absorbed by an luminescent screen behind the sample, which converts the X-rays into visible light. This visible light passes through a lens system and gets detected by a CCD camera. From a full data set of parallel projections (180° measurement) the information about the material in one slice can be reconstructed using mathematical algorithms and an image of this slice can be created [Sla99]. With multiple slices a 3D-image can be generated.

Right now the experiment is not ready for use, since the modification of BL 2 is still in progress. Parts of the beamline have already been replaced to make the piping less complicated and less prone to leakage. A new collimator has been installed to provide a beamsize of 30 mm x 9,2 mm at the sample. For further reduction of the beamsize to the actual size of the sample a slit system is going to be installed right in front of the CT. Furthermore, a fastshutter will be mounted to protect the sample and CCD. There are also plans on exchanging the beryllium window with a titan or aluminium window, to eliminate the risk of releasing poisonous beryllium dust in case of a window rupture.

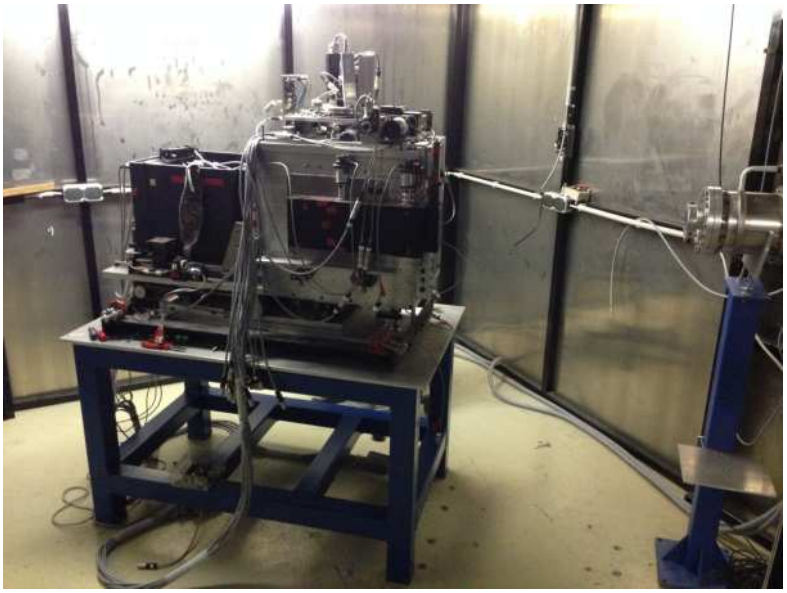

Figure 1: Microtomography apparatus inside the hutch of BL 2

The checking of the µCT apparatus, that is shown in fig. 1, is also going on: all motors for moving the CT and adjusting the CCD and lens have been tested. The former CCD camera has been replaced: The new camera is a MaxCam CM8-3E from FLI with a Kodak, KAF-1602E, 1536 x 1024 pixel sensor. Pixel size is 9 x 9 μm^2 so the maximum sample size will be about 15 mm (or 30 mm with the 360° mode, that moves the centre of rotation to one side of the FOV [Don06].)
The control system of the tomography apparatus has to be established and the whole safety and interlock system has to be installed. First calibration measurements are expected to be possible in February or March 2017.

We acknowledge DELTA machine group for support and thank the HZG for providing the CT apparatus.

References

[Bec98] Felix Beckmann. "Entwicklung, Aufbau und Anwendung eines Verfahrens der Phasenkontrast-Mikrotomographie mit Röntgen-Synchrotronstrahlung". PhD thesis. Universität Dortmund, 1998.

[Don06] Tilman Donath. "Quantitative X-ray Microtomography with Synchrotron Radiation". PhD thesis. GKSS-Forschungszentrum Geesthacht, 2006.

[Sla99] Avinash C. Kak; Malcom Slaney. *Principles of Computerized Tomographic Imaging*. 1999.

Soft X-ray Spectroscopy

Time- and energy-resolved photoemission experiments on Cu(111) at beamline 5 at DELTA

M. Plötzing[1,2], S. Döring[1,2], S. Xiao[2], P. Ungelenk[3], G. Shayeganrad[3], C. Mai[3], A. Meyer auf der Heide[3], M. Gehlmann[1,2], S. Cramm[1], L. Plucinski[1,2], U. Bovensiepen[2], S. Khan[3], C.M. Schneider[1,2]

[1] Peter Grünberg Institut, PGI-6, Forschungszentrum Jülich GmbH, 52425 Jülich, Germany
[2] Experimentalphysik - Universität Duisburg-Essen, Lotharstr. 1, 47057 Duisburg, Germany
[3] DELTA - TU Dortmund, Maria-Goeppert-Mayer-Str. 2, 44227 Dortmund, Germany

(10th November 2016)

For the first time, the ultrashort photon pulses which are produced by the DELTA storage ring using the coherent harmonic generation (CHG) scheme [1] were used for time-resolved photoelectron spectroscopy experiments at the endstation of beamline 5 (BL5) [2]. Here, the storage ring contains only one single 100 ps electron bunch. Moreover, a 3 eV, 50 fs driving laser pulse interacts with a central slice of this bunch inside an undulator at every $\approx$ 2600th revolution leading to the emission of a coherent sub-picosecond CHG pulse at a harmonic of the driving laser.

In our experiments, we probed the surface state of Cu(111) with 9 eV synchrotron radiation. In the CHG operation mode of DELTA, we can use our delay-line detector to select either the signal created from the CHG pulses, which have a repetition rate of 1 kHz, or from the remaining single-bunch signals of spontaneous synchrotron light pulses every 386 ns. Moreover, we introduced 1.5 eV pump pulses, which are naturally synchronized with the CHG pulses as they are split off from the driving laser pulses. Their arrival time can be adjusted by changing their path length with respect to the CHG pulses. Negative delays ($\Delta t < 0$) represent the situation that the CHG pulses arrive before the pump pulses. The point of zero delay between both pulses was estimated based on a two-photon absorption measurement in a SiC photodiode using the pump pulses and the 3 eV driving laser pulses for the CHG radiation. The latter copropagate with the synchrotron radiation into BL5.

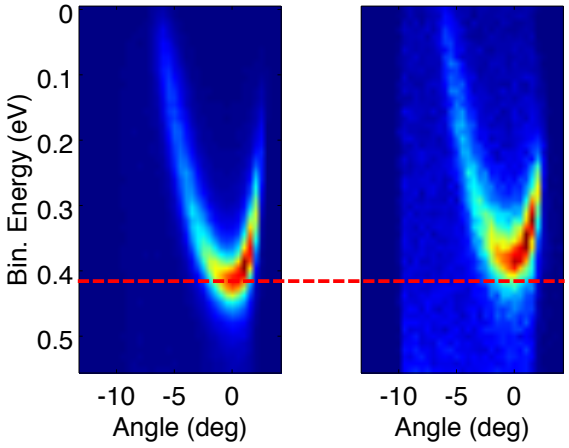

Figure 1: Angle-resolved photoemission spectra of the Cu(111) surface state. Left: Data obtained by excitation with spontaneous synchrotron radiation, which is not influenced by space-charge from electrons created by 1.5 eV pump pulses (see text). Right: The same measurement, but now observing photoelectrons excited by the CHG radiation. Here, the space-charge from the pump-induced electrons (created at $\Delta t = -100$ ps) leads to a clear shift in energy.

It is well-known that intense 1.5 eV pulses can be used to create photoelectrons based on multiphoton excitation [3]. We use this fact to create an electron cloud with the pump pulse, which interacts with photoelectrons emitted by the CHG light via Coulomb

repulsion. Note that the temporal distance between the pulses of spontaneous radiation and the pump pulse is large enough (minimum distance: 386 ns$\pm\Delta t$) to avoid significant distortion due to the resulting space-charge from the additional electron cloud. The influence of these pump-induced space-charge effects decays on a time scale of several ns as we will show later. Therefore, the data obtained with spontaneous radiation represent the undisturbed situation.

The left side of Fig. 1 shows the ARPES intensity from the Cu(111) surface state measured with spontaneous radiation, whereas the right side displays ARPES data extracted from the same measurement, but now focusing on the photoelectrons emitted by the CHG radiation. During the measurements, a significant amount of additional electrons was created by the pump pulses, delayed by $\Delta t = -100$ ps with respect to the CHG pulses. The resulting space-charge causes an energy shift of the photoemission spectrum excited by the CHG pulses as indicated by the red horizontal lines. Here, the shift has a size of 37 meV.

Furthermore, we studied the dependence of the energy shift on the delay between the CHG and the pump pulses. For this purpose, angle-resolved spectra as shown in Fig. 1 are measured and integrated over all angles. Then, the energy shift is determined by fitting the angle-integrated data and extracting the peak position. Figure 2 summarizes the observed energy shifts for different delays. Measurements were first performed with increasing (black data points) and then with decreasing delays (red data points). Both

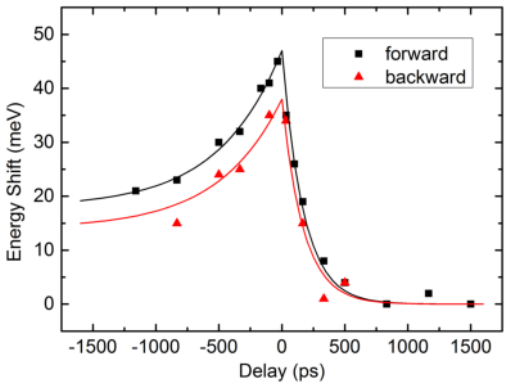

Figure 2: Energy shift of the "pumped" photoemission spectra recorded with CHG radiation relative to the "unpumped" spectra recorded with spontaneous synchrotron light. The data is plotted as a function of the delay between pump and CHG pulses. The lines are drawn to guide the eye.

curves show a similar shape, but a different size of the effect. The latter can be partly attributed to a slow decay of the intensity of the 1.5 eV pump pulses with time during the measurement ($< 5\,\%$) and therefore a small decrease of the number of pump-induced photoelectrons. In addition, the CHG pulses always contain a background of spontaneous radiation, which is simultaneously emitted but has a longer pulse duration (≈ 100 ps). With increasing measurement time and thus decreasing electron current in the storage ring, this background continuously changed from 16 % to 24 % for our results. Since the longer pulse duration of the spontaneous radiation leads to a less distinct influence of space-charge effects, this can result in a difference in the extracted energy shifts. However, the shape of the curves in general agrees with previous work [4,5] and reflects the Coulomb interaction between the photoelectrons generated by the CHG and the pump pulses. We explain the small deviations between our data and the published results by differences in

the photon energy.
In sum, our results demonstrate that both spatial (mm scale) as well as temporal (± 30 ps) overlap between the CHG and the 1.5 eV pump pulses is achieved in the experiment. Moreover, the feasibility of pump-probe photoemission experiments at BL5 at DELTA is shown.

[1] S. Khan et al., *Generation of Ultrashort and Coherent Synchrotron Radiation Pulses at DELTA*, Synchrotron Radiat. News **26**, 25 (2013).

[2] L. Plucinski et al., *A hemispherical photoelectron spectrometer with 2-dimensional delay-line detector and integrated spin-polarization analysis*, J. Electron. Spectrosc. Relat. Phenom. **181**, 215 (2010).

[3] D. M. Riffe et al., *Femtosecond thermionic emission from metals in the space-charge-limited regime*, J. Opt. Soc. Am. B **10**, 1424 (1993).

[4] L.-P. Oloff et al., *Time-resolved HAXPES at SACLA: probe and pump pulse-induced space-charge effects*, New J. Phys. **16**, 123045 (2014).

[5] M. Plötzing et al., *Spin-resolved photoelectron spectroscopy using femtosecond extreme ultraviolet light pulses from high-order harmonic generation*, Rev. Sci. Instrum. **87**, 043903 (2016).

Structure determination of silicene nanoribbons on Ag(110)

P. Espeter[1,2,*], C. Keutner[1,2], F. Kleimeier[3], P. Roese[1,2],K. Shamout[1,2], G. Wenzel[3], U. Berges[1,2], H. Zacharias[3], C. Westphal[1,2]

[1] Experimentelle Physik I - Technische Universität Dortmund, Otto-Hahn-Str. 4, D-44227 Dortmund
[2] DELTA - Technische Universität Dortmund, Maria-Goeppert-Mayer-Str. 2, D-44227 Dortmund
[3] Fakultät Physik - WWU Münster, Wilhelm-Klemm-Str. 10, D-48149 Münster
[*] corresponding author: philipp.espeter@tu-dortmund.de

Since the advent of graphene much interest arises in graphene analoga from the carbon group. One of the most famous representative is silicene. Like graphene silicene is known to crystallize in different configurations depeding on the growth conditions. For example silicene sheets grow onto an Ag (111) substrate and silicene nanoribbons grow onto Ag (110) substrates. Whereas the structure of silicene sheets on Ag(111) substrate is already well known [1] the structure of silicene nanoribbons is still not clear. A multiplicity of theoretical simulations [2] and scanning tunneling microscopy [3] studies yielded several possible structure models, still, the structure is under discussion. Since photoelectron spectrocopy (XPS) and photoelectron diffraction (XPD) are surface sensitive tools for structure analysis we perform XPS and XPD measurements on silicon nanoribbons on Ag(110) substrate to asses the suggested structure models and present further improvements based on our measurements. The sample is illuminated with monochromatic X-rays, provided by the U55 PGM Beamline 11 at

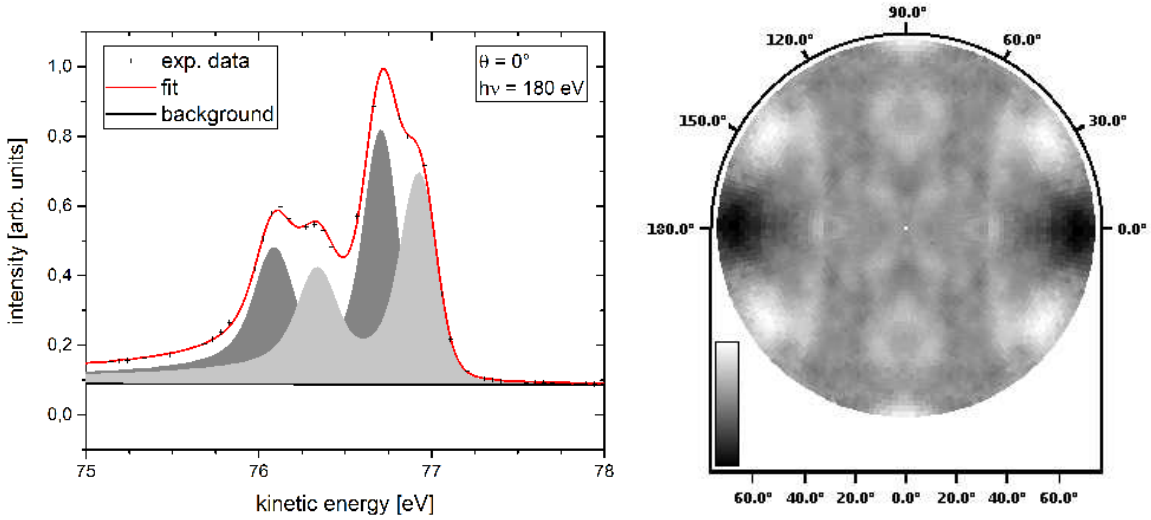

Figure 1: High-resolution XPS spectra of Silicon-2p-signal (left) and measured XPD pattern of the Silicon-2p-signal(right).

DELTA. The photoelectron spectra are recorded as a function of azimuthal and polar angle [4]. The high-resolution XPS spectra provide information concerning the chemical bonding of silver and silicon. The observed anisotropic modulations recorded in the XPD pattern provide information about the local environment of the emitting atoms.
The XPD analysis is performed by three iterating steps, first generating a structure model, second simulation of the XPD pattern by using the MSPHD programm and third comparison with the experimental data [5]. As the degree of accordance the reliability-factor (R-factor) is used, where a R-factor of 0 means exact accordance and a R-factor of 2 means exact anticorrelation. A sufficient accordance between the experimental and simulated data is reached if the R-factor is less than 0.1 [6].
The XPS signal of the Silicon-2p-signal, displayed in figure 1, shows the same characteristic silicene signature as reported by other authors. It consists of to components which are seperated by about 0.3 eV. This is in good agreement with previous works [7]. The XPD pattern is depicted in figure 1.

Comparison between simulated XPD pattern of about 40 structures proposed by other authors and the measured pattern resulted in R-factors of about $R > 0.2$. The multiplicity of the suggested structures ranges from rectangular over pentagonal to hexagonal, armchair or zig-zag terminated edges and from planar over buckled to stacked. However we demonstrate a structure that fits to the experimental data. Starting with the hexagonal arm-chair terminated buckeld silicene structure we applied some structural modifications. In particular distances and bonding angles within the silicene layer, the silicene to substrate distance as well as the orientation between the substrate and the silicene. This yielded a R-factor of $R = 0.09$. The correspondig structure model is pictured in figure 2. Nevertheless

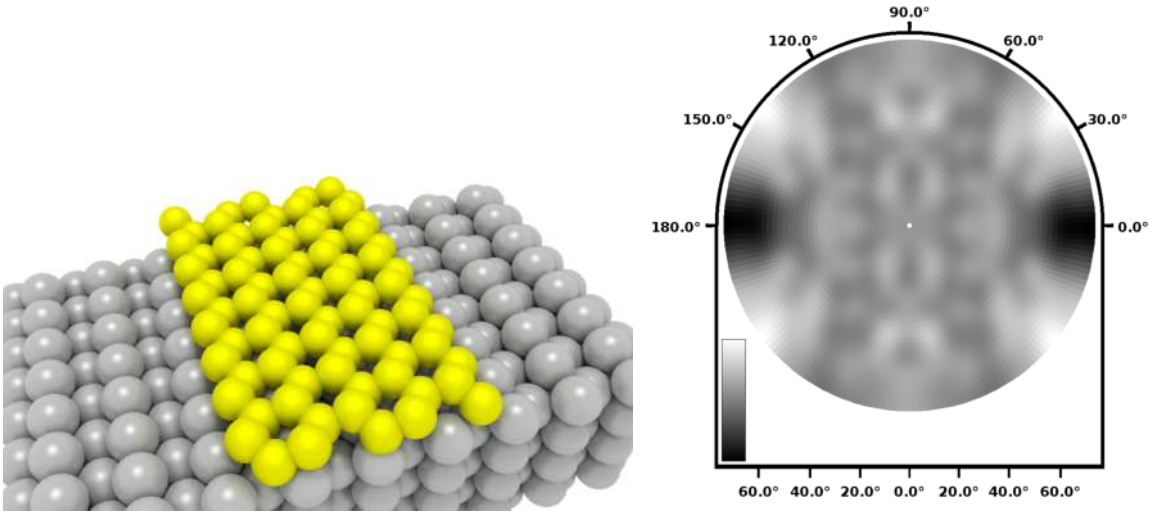

Figure 2: Simulated XPD pattern of Silicon-2p-signal (left) and the corresponding structure model (right).

further investigations of the silver silicon interaction have to be performed in the future.

References

[1] P. Vogt, P. De Padova, C. Quaresima, J. Avila, E. Frantzeskakis, M. C. Asensio, A. Resta, B. Ealet and G. Le Lay, *Silicene: Compelling Experimental Evidence for Graphenelike Two-Dimensional Silicon*, Phys. Rev. Lett. **108**, 155501 (2012).

[2] G.-m. He, *Atomic structure of Si nanowires on Ag(110): A density-functional theory study*, Phys. Rev. B **73**, 035311 (2006).

[3] B. Aufray, A. Kara, S. Vizzini, H. Oughaddou, C. LÃ©andri, B. Ealet and G. Le Lay, *Graphene-like silicon nanoribbons on Ag(110): A possible formation of silicene*, Applied Physics Letters **96** (2010).

[4] C. Westphal, *The study of the local atomic structure by means of X-ray photoelectron diffraction*, Surface Science Reports **50**, 1 (2003).

[5] R. Gunnella, F. Solal, D. Sebilleau and C. Natoli, *MSPHD: A full multiple scattering code for low energy photoelectron diffraction*, Computer Physics Communications **132**, 251 (2000).

[6] D. P. Woodruff and A. M. Bradshaw, *Adsorbate structure determination on surfaces using photoelectron diffraction*, Reports on Progress in Physics **57**, 1029 (1994).

[7] P. D. Padova, C. Quaresima, P. Perfetti, B. Olivieri, C. Leandri, B. Aufray, S. Vizzini and G. L. Lay, *Growth of Straight, Atomically Perfect, Highly Metallic Silicon Nanowires with Chiral Asymmetry*, Nano Letters **8**, 271 (2008), PMID: 18092826.

Characterization of graphene on 6H-SiC(0001) by means of PEEM and XPS

R. Hönig[1*], P. Espeter[1,2], P. Roese[1,2], K. Shamout[1,2], H. Kromer[1], U. Berges[1,2], C. Westphal[1,2]

[1] Experimentelle Physik I - Technische Universität Dortmund, Otto-Hahn-Str. 4a, D-44221 Dortmund
[2] DELTA - Technische Universität Dortmund, Maria-Goeppert-Mayer-Str. 2, D-44221 Dortmund
[*] corresponding author: richard.hoenig@tu-dortmund.de

The main issue in graphene preparation on silicon carbide (SiC) is the size of the individual graphene flakes. This grain size is a critical parameter for the development of electronic devices due to frequent scattering at grain boundaries. Thus, the intrinsic carrier mobility decreases. Heating a SiC crystal to about 1200 °C in high vacuum leads to preferential silicon sublimation and the growth of several layers graphene with lateral dimensions of about 0.1 µm. To achieve a higher grain size the decomposition rate of the crystal has to be decreased. Here, two different approaches of limiting the sublimation rate of the silicon atoms are performed: the self-limiting by the silicon vapor in an enclosed volume under high vacuum conditions or the limitation of the decomposition rate by the vapor pressure of an additional inert gas [1].

In figure 1 (left) an image of a sample prepared in an enclosure under high vacuum conditions obtained by photoemission electron microscopy (PEEM) in threshold mode is shown. A stripe structure with widths up to 0.6 µm has grown along the substrate step edges. The apparent contrast is essentially caused by work function differences of the sample. This leads to the possibility to count the relative number of layers, because the work function of the sample increases with each additional graphene layer [2]. Hence, the dark regions in the image correspond to a higher coverage of graphene. The absolute number of layers cannot be determined by this method, but as will be shown later it can be elucidated by x-ray photoelectron spectroscopy (XPS). In figure 1 (right) a PEEM image of a sample prepared

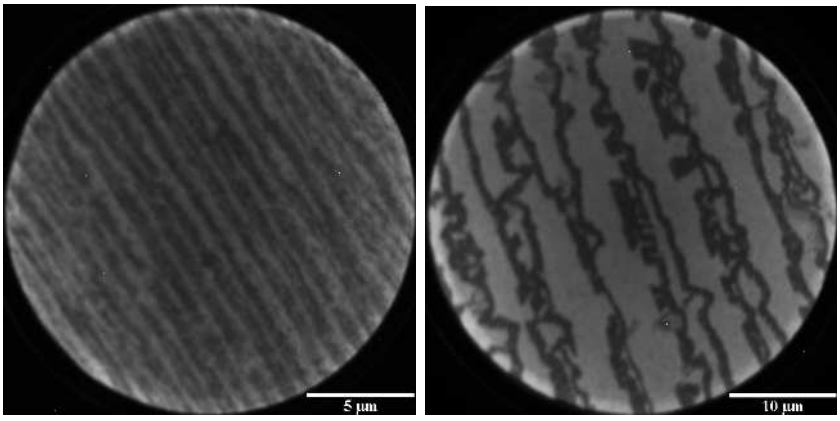

Figure 1: Left: PEEM image of a sample prepared in high vacuum, right: PEEM image of a sample prepared in Argon atmosphere.

in an Argon atmosphere is presented. A width of the graphene stripes of 4 µm in contrast to 0.6 µm shows that the Argon method is a great advantage compared to the high vacuum method.

As mentioned before, the absolute number of graphene layers is not known until know. To clearify this, high resolution XPS spectra of the C1s core level were recorded. In figure 2 (left) a spectrum of a sample prepared in a Xenon atmosphere is shown. Several components resulting from the different chemical environment of the C atoms can be distinguished [3]: the substrate (SiC), the C atoms of the buffer layer which are bonded to the substrate (S1), the C atoms with interlayer bonding (S2) and a oxide component (-C-O-) due the the *ex situ* preparation. The absence of the typical graphene component is an evidence for the solely growth of a buffer layer. The growth of additional graphene layers is inhibited due to the higher atomic mass of Xenon which suppresses the growth rate even more than Argon. This bare buffer layer is of particular interest for intercalation experiments [4, 5]. A spectrum of a

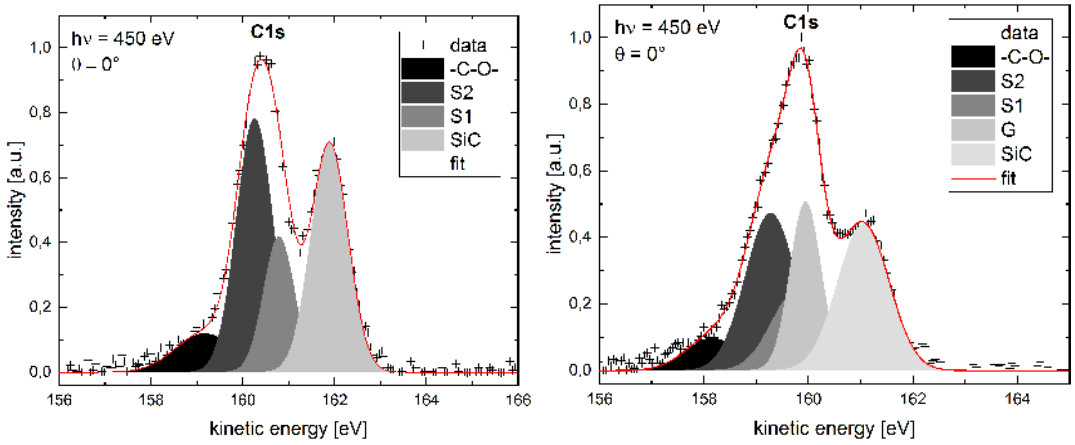

Figure 2: Left: C1s core level spectrum of a sample prepared in Xenon atmosphere, right: C1s core level spectrum of a sample prepared in high vacuum.

sample prepared in high vacuum with the same parameters as the sample presented in figure 1 (left) is shown in figure 2 (right). In this spectrum an additional peak at a kinetic energy of 160 eV arises which is the genuine graphene component. From the presence of the peaks S1, S2 and G and their relative signal strengths one concludes a mixing of areas with monolayer graphene and buffer layer.

In this work the grain size of graphene flakes was measured by means of PEEM, where large and homogenous graphene growth is observed depending on the preparation parameters. The number of graphene layers was identified by high resolution XPS spectra. Further PEEM studies will focus on the magnetic properties of intercalated graphene and XPS measurements will yield complementary information of the intercalation process.

Acknowledgement

We would like to thank the DELTA-staff for their support.

References

[1] W. A. de Heer, C. Berger, M. Ruan, M. Sprinkle, X. Li, Y. Hu, B. Zhang, J. Hankinson and E. Conrad, *PNAS* **108**, 16900 (2011).

[2] H. Hibino, H. Kageshima, M. Kotsugi, F. Maeda, F.-Z. Guo, and Y. Watanabe, *Phys. Rev. B* **79**, 125437 (2009).

[3] C. Riedl, C. Coletti and U. Starke, *J. Phys. D: Appl. Phys.* **43**, 374009 (2010).

[4] K. V. Emtsev, A. A. Zakharov, C. Coletti, S. Forti and U. Starke, *Phys. Rev. B* **84**, 125423 (2011).

[5] L. H. de Lima, D. Handschak, F. Schönbohm, R. Landers, C. Westphal and A. de Siervo, *Chem. Commun.* **50**, 13571 (2014).

Synchrotron radiation damage on Copper Naphthalocyanine layers

P. Roese[1,2,*], P. Espeter[1,2], K. Shamout[1,2], U. Berges[1,2], C. Westphal[1,2]

[1] Experimentelle Physik I - Technische Universität Dortmund, Otto-Hahn-Str. 4a, D-44221 Dortmund

[2] DELTA - Technische Universität Dortmund, Maria-Goeppert-Mayer-Str. 2, D-44221 Dortmund

[*] corresponding author: peter.roese@tu-dortmund.de

The organic semiconductor naphthalocyanine is a phthalocyanine derivate. These kind of molecules are conductive molecules with delocalized π-electronic structures. Extended delocalized π-electrons result in fascinating properties and make the molecules suitable for applications such as organic solar cells [1], organic LED's [2] and molecular switches [3]. Furthermore, the usage of naphthalocyanines as photosensibilisator in cancer treatment [4] utilize the strong absorption properties of functional molecules in the visible spectrum. By adding different substituents or metal atoms to the center of the molecule differing chemical, physical and electronic properties can be tuned. Because of these tunable characteristics, functional molecules are studied intensively in recent research.

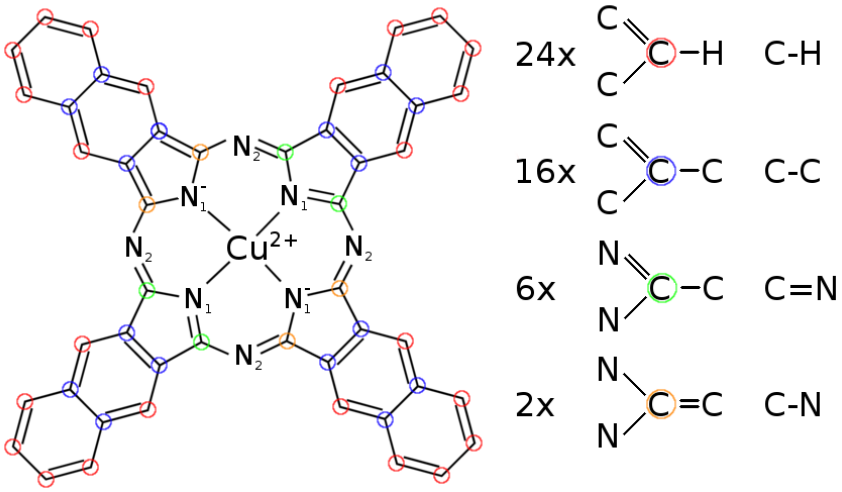

Figure 1: Structure of Copper-Naphthalocyanine (Cu-NPc). The different carbon bonding states are marked with colored circles, the total number of each bonding state is listed in the legend on the right. The two different nitrogen bonding states pyrrolic and aza-bridging are named N_1 and N_2, respectively.

The question how Cu-NPc adsorbs on and interacts with inert surfaces is of particular interest. An appropriate method to study the local near order of adsorbates and the interface between adsorbate and substrate is the x-ray photoelectron diffraction (XPD). Due to the long examination times of 24 h or longer, it is necessary to investigate the stability of naphthalocyanines under synchrotron radiation. In this work, synchrotron radiation based damage of Copper-Naphthalocyanine (Cu-NPc) deposited using molecular beam epitaxy at 550 °C onto an Ag(110) surface was studied using x-ray photoelectron spectroscopy (XPS). The experiments were performed at the U55 beamline 11 at DELTA. Figure 1 shows the

structure of the intact molecule, the different chemical bonds are marked with colored circles and the pyrrolic and aza-bridging nitrogens are labeled with N_1 and N_2, respectively.

An indicator for the radiation damage are the eight nitrogen atoms in the center of the molecule. Especially the pyrrolic nitrogen (N_1), which are binding to the copper atom in the center of the molecule, have been detected as major weakness in aromatic molecules [5].

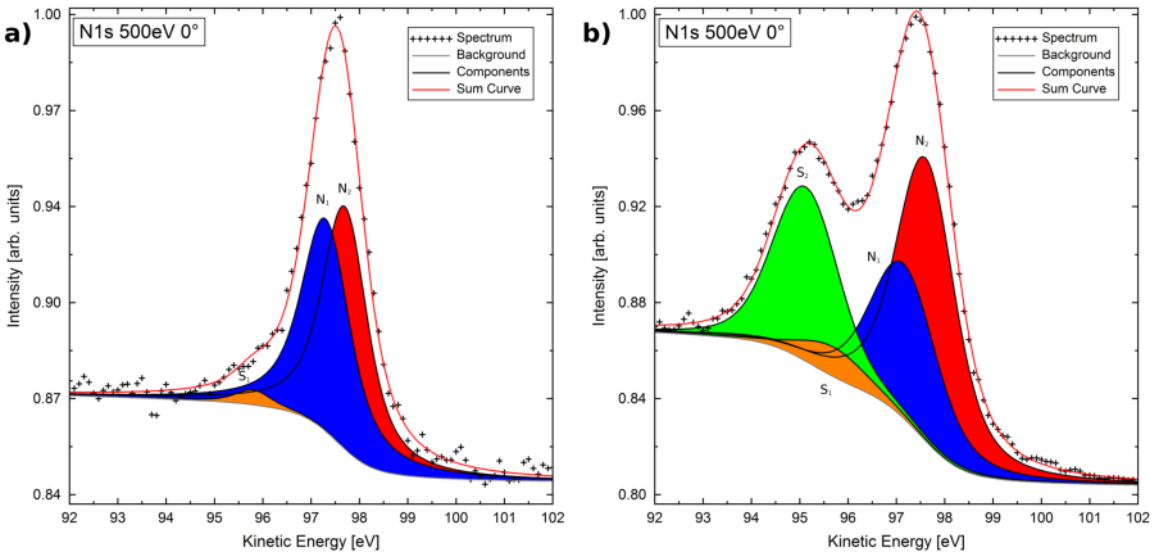

Figure 2: N 1s XPS spectra of Cu-NPc using a photon energy of hν = 500 eV and a polar angel of $\Theta = 0°$ directly after molecule deposition a) and after 17 h of irradiation with synchrotron radiation b). The components N_1 at $E_{kin} = 97.70$ eV and N_2 at $E_{kin} = 97.30$ eV correspond to the pyrrolic nitrogens bonded to the copper atom and the aza-bridging nitrogens (see figure 1), respectively. The S_1 component at $E_{kin} = 95.80$ eV can be identified as satellite structure resulting from the π electron system. After 17 h synchrotron radiation a new component S_2 rises at $E_{kin} = 95.12$ eV.

Figure 2 a) shows the high resolution XPS spectrum of N 1s of CuNPc on Ag(110) for a polar angle of $\Theta = 0°$ directly after molecule deposition. The spectrum can be fitted with three peaks referring to the pyrrolic nitrogen (N_1), the aza-bridging nitrogen (N_2) and a shake-up satellite peak at lower kinetic energy resulting from π-π^* transitions. These satellites are typical for aromatic molecules. The distance between the aza-bridging and pyrrolic peaks of about 0.4 eV as well as the peak area ratio of 0.94 : 1 is in excellent agreement with literature and theoretical values [6]. This spectrum demonstrates the non-destructive deposition of the molecules onto the surface. Figure 2 b) shows the high resolution XPS spectrum of N 1s of CuNPc on Ag(110) for a polar angle of $\Theta = 0°$ after 17 h of illumination with synchrotron light. A new peak (S_2) rises at lower kinetic Energies while the pyrrolic nitrogen (N_1) loses intensity. The aza-bridging nitrogen component (N_2) remains unchanged. This spectrum indicates the radiation induced damage of the molecules. The bonds of the nitrogen atoms to the copper atom in the center (N_1) seem to be broken while the outer aza-bridging nitrogens (N_2) are not affected. The results are in perfect agreement with previous studies [5].

A further evidence for the type of the radiation induced damage is the C 1s XPS spectrum. Figure 3 a) shows the high resolution XPS spectrum of C 1s of CuNPc on Ag(110) for a polar angle of $\Theta = 0°$ directly after molecule deposition and figure 3 b) shows the same spectrum after 17 h of irradiation with synchrotron light.

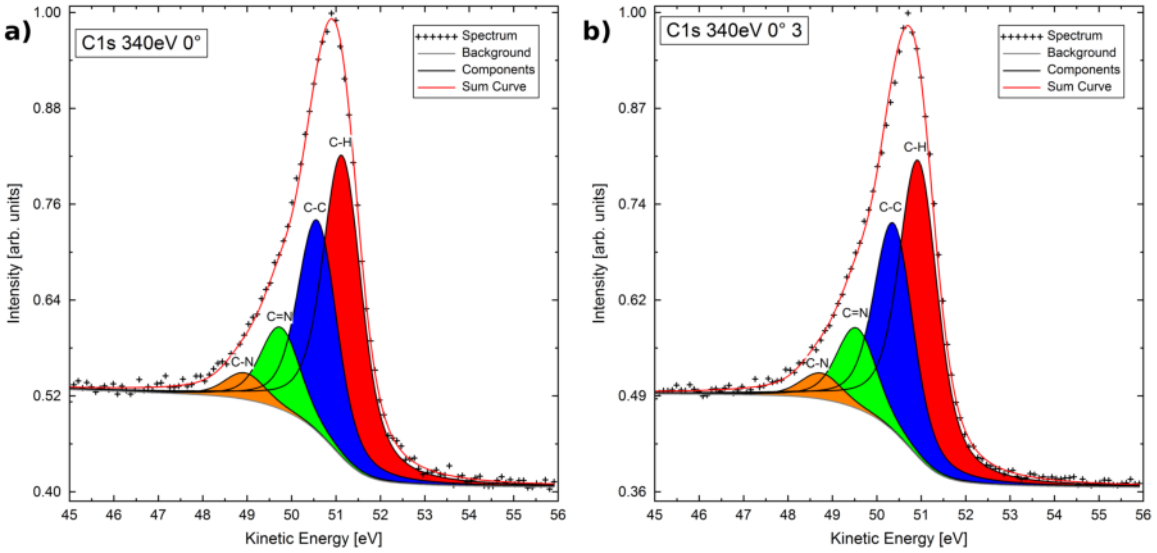

Figure 3: C 1s XPS spectra of Cu-NPc using a photon energy of hν = 340 eV and a polar angel of $\Theta = 0°$ directly after molecule deposition a) and after 17 h of synchrotron radiation b). The four components correspond to the four different chemical binding states of the carbon atoms in the molecule. The colors and labels are identical to the marked circles in figure 1.

The four components in each spectrum represent the four different carbon bonding states in the molecule, as shown with colored circles in figure 1. In the legend of figure 1, the total number of each different carbon bond in the molecule is listed. With these numbers a theoretical peak area ratio can be calculated as $0,50 : 0,33 : 0,125 : 0,04$. This ratio fits to the experimental data both directly after the deposition (figure 3 a)) and after 17 h of irradiation with synchrotron light (figure 3 b)). It can be summarized, that no changes in the C 1s signals are strong points for intact carbon bonds while the synchrotron radiation damages especially nitrogen bonds.

The main threshold for radiation damage is the photon flux of the beamline. A rough assessment for the photon flux for beamline 11 at DELTA is 10^{12} - 10^{13} $\frac{\text{photons}}{\text{s}\cdot 100\text{mA}}$ with a focus size of $70\,\mu$m (h) $\cdot$ $30\,\mu$m (v) [7].

Moving the experimental station out of the focus of the beamline reduces the photon flux. At the new position of about 0.4 m behind the beamline focus, the photon density is approximately 400 times smaller because of the increased size of the beam spot without losing intensity of the photoelectron signal. The XPS measurements for this system with the position modifications are scheduled for the upcoming beamtime. We're looking forward to perform photoelectron diffraction measurements of these molecules without synchrotron radiation damage in the future.

References

[1] R. Koeppe et al., *Applied Physics Letters* **87**, 244102 (2005).
[2] S. Wang et al., *Journal of Physical Chemistry B* **107**, 12639 (2003).
[3] E. Emberly et al., *Physical Review Letters* **91**, 188301 (2003).
[4] M. Shopova et al., *Journal of Biomedical Optics* **4**, 276 (1999).
[5] P. L. Cook et al., *The Journal of Chemical Physics* **131**, 214702 (2009).
[6] L. Ottaviano et al., *Journal of Electron Spectroscopy and Related Phenomena* **105**, 145 (1999).
[7] C. Westphal et al., *Journal of Electron Spectroscopy and Related Phenomena* **144**, 1117 (2005).

XPD experiments and simulation of GaAs(001)-c(8×2)

K. Shamout[1,2,*], P. Espeter[1,2], P. Roese[1,2], U. Berges[1,2], C. Westphal[1,2]

[1] Experimentelle Physik I - Technische Universität Dortmund, Otto-Hahn-Str. 4a, D-44221 Dortmund
[2] DELTA - Technische Universität Dortmund, Maria-Goeppert-Mayer-Str. 2, D-44221 Dortmund
[*] corresponding author: karim.shamout@tu-dortmund.de

The III-V compound semiconductor gallium arsenide is an applicable substrate for spintronic multilayer systems due to its electronical und magnetic properties [1, 2]. The structure of GaAs(001)-(4×2) in the MgO/Fe/GaAs(001) system as already been studied in different previous works [3, 4]. GaAs(001) performs different reconstructions since the Ga-As ratio can determine the possible top layer arrangement. In this work, we take the analysis of the GaAs surface reconstructions a step further by analysing the GaAs(001)-c(8×2) structure where huge uncertainties arise. Since STM scans only the top layer photoelectron diffraction (XPD) provides detailed information of the surface and interface of the sample. Thereby Ga or As dimers 5 Å beneath the surface can be resolved.
In 2008 Ohtake et al. have shown 8 different possible structures of the GaAs-c(8×2) surface [5]. These structures differ by the number of Ga dimers at the surface, the sub-dimers or the arrangement of circular formed Ga-As rings. Until now no progress in the determination has been achieved. In this work we present a structural model that fits best to the experimental data.

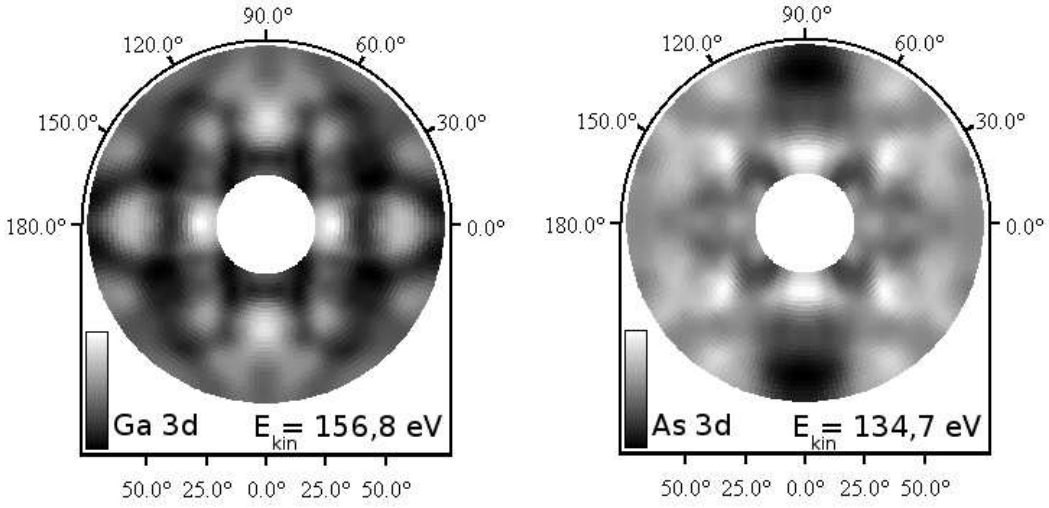

Figure 1: Measured XPD pattern of Ga 3d (left) and As 3d (right) at $E_{h\nu} = 180\,\mathrm{eV}$ from $\theta = 22° - 72°$.

The sample is illuminated with monochromatic X-ray provided by the U55 PGM Beamline 11 at DELTA, Dortmund. XPS spectra of Ga 3d and As 3d are recorded for each polar and azimuth angle in the hemisphere. Their anisotropic intensity modulation are shown in figure 1.

In the next step different atomic clusters were build and a XPD pattern was simulated by the MSPHD program. This algorithm provides XPD pattern for kinetic energies at $E_{kin} \leq 200\,\text{eV}$. Afterwards the resulting pattern is compared with the measured pattern and is quantified with the well-known R-factor ($R \in [0\ ,\ 2]$). Hereby, a factor of $R \leq 0.1$ indicates a structural accordance.
The structure suggested by Kumpf et al. roughly fits the best [6]. Moreover, we could correct the exact positioning of the subdimers. The resulting XPD pattern and the corresponding structure are displayed in fig. 2.

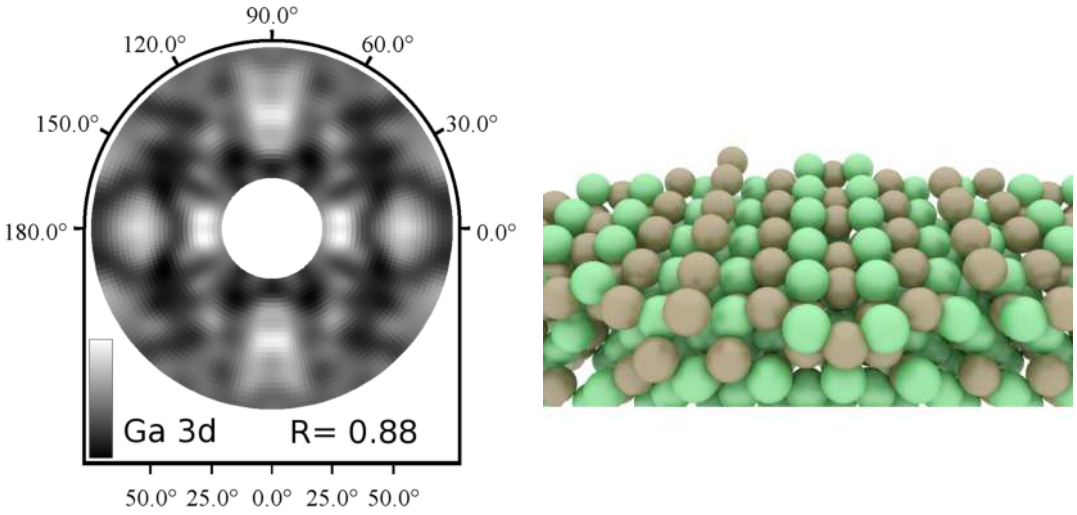

Figure 2: Simulated Ga 3d XPD pattern with R = 0.082 (left) and the resulting surface structure (right).

Although a R-factor of $R_{Ga\,3d} = 0.082$ as been achieved the higher polar angles $\theta \geq 62°$ that provide high statistic errors in the experiment need to be investigated again in order to get and an even better $R - factor$.

References

[1] S.-H. Yang et al. *Phys. Rev. B*, **84**:184410, 2011.

[2] B. Kardasz et al., *Journal of Applied Physics*, **109** (07D337):3, 2011.

[3] D. Handschak et al., *Phys. Rev. B* X, **88**:045313, 2013

[4] K. Shamout, *Untersuchung von Fe/GaAs(001) mittels Photoelektronenspektroskopie*, master thesis, TU Dortmund, 2016

[5] A. Ohtake et al., *Surface Science Reports*, Volume 63, Issue 7, 2008

[6] C. Kumpf et al., *Physical Review Letters*, Volume 86, No. 16

X-ray Scattering

X-ray diffraction from the side planes of core-shell nanowires

Ali Al Hassan, R.B. Lewis, H. Küpers, A. Davtyan, L.Geelhaar and U. Pietsch

Paul Drude- Institute Berlin, Solid state physics, University of Siegen.

Semiconductor core-shell Nanowires are promising candidates for future optoelectronic devices. One of these structures is a GaAs/$In_xGa_{1-x}As$/GaAs double heterostructure grown by MBE onto (111) silicon substrate. For optical performance one need to probe the lattice mismatch along the normal to nanowire side planes. The XRD measurements of samples with x=0.15 but different shell thickness have been performed on NW ensembles at beamlines BL9 at DELTA with photon energy of 13keV. Considering the hexagonal shape of the NWs, the interfacial strain field is expected to be different along the direction normal to the {1-10} side planes and along the [2-1-1] edges of NWs grown along the [111] direction. We recorded 2D reciprocal space maps (RSM) in vicinity of the (111) Bragg reflection along the growth direction and along a direction perpendicular, i.e. parallel to the scattering vector of the (2-20) side plane, named Q_z. A RSM taken at the [1-10] Bragg reflection of one of the samples is displayed in figure 1, plotting the intensity distribution as function of reciprocal space vectors, Qx and Qz. For quantitative analysis, line profiles were created by projecting the intensity distribution onto the Qz axis, and compared with other investigated samples. The peak with the highest intensity is attributed to the GaAs core. Peak A originates from the partially compressed (2-20) GaAs outer shell planes. Peaks C and B are associated with the relaxed InGaAs planes along the scanned direction and the two other pairs of facet planes oriented with $\pm$ 60^0 with respect to C, respectively.

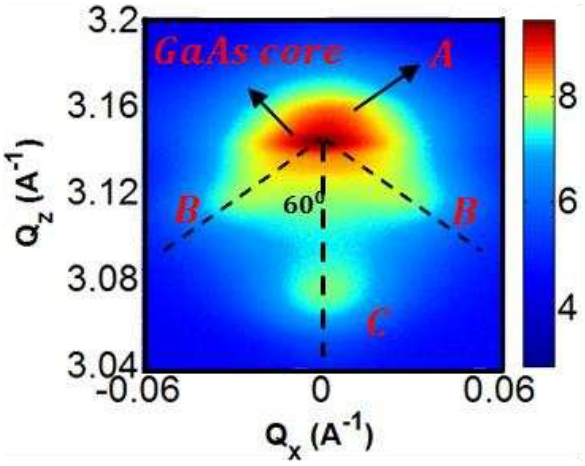

Figure 1: 2D RSM of the [1-10] reflection for 140/40/30nm GaAs/$In_{0.15}Ga_{0.85}As$/GaAs NWs.

DELTA user report 2016
Proposer: Prof. Dr. A. Ludwig
Co-Proposers: A. Furlan, S. Salomon, D. Grochla, L. Banko

Investigation of texture in Al-Cr-O-N films using synchrotron grazing incidence XRD

L. Banko

Werkstoffe der Mikrotechnik, Institut für Werkstoffe, Fakultät Maschinenbau

Ruhr-Universität Bochum, D-44801 Bochum

Al-Cr-O-N thin films, deposited by High Power Impulse Magnetron Sputtering (HiPIMS) technique, were investigated at BL 9 using mar345-detector with an energy of 15 keV. In total 9 samples, synthesized in three different processes with three different Al/Cr-ratios each were characterized regarding their crystal structure and texture. The samples showed no indication of oxide-phases in XRD experiments with Bragg-Brentano geometry performed in our lab, despite an oxygen content of up to 40 at.%. The purpose of this investigation was to identify oxide phases that could not be identified in these measurements due to texture effects or low diffraction intensities. However, no oxide phases were found in the grazing incidence XRD patterns acquired at BL 9, indicating that an oxygen content of at least 40 at.% can be solved in the fcc-Cr-N lattice either due to substitution of N or due to interstitial incorporation of O.

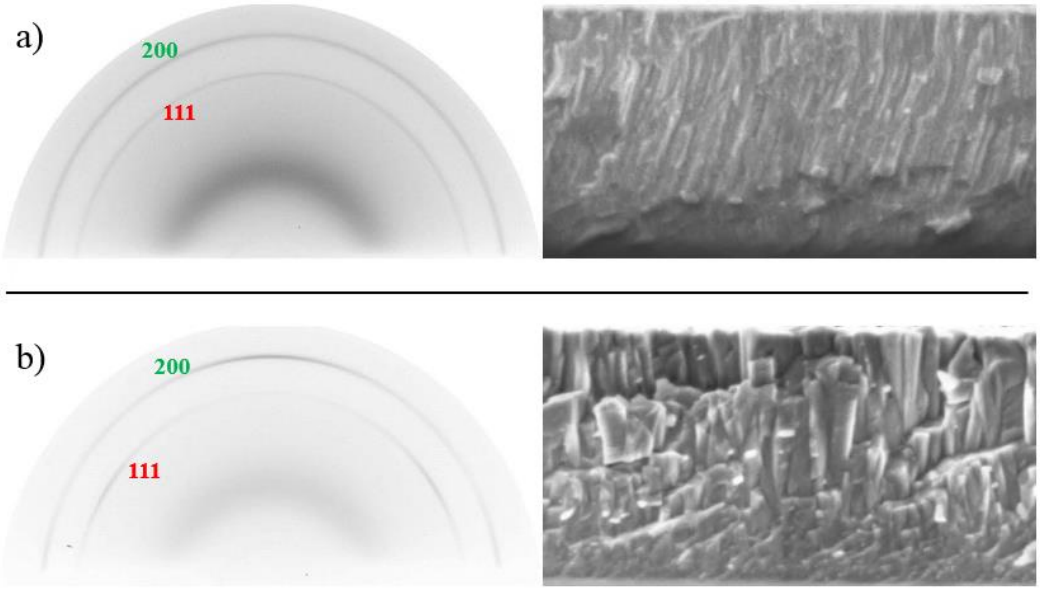

Figure 1: Diffraction patterns and SEM images of a) Al-rich Al-Cr-O-N and b) Cr-rich Al-Cr-O-N films.

Comparing the diffraction patterns of Al-rich and Cr-rich samples, the thin films exhibit significant differences in texture (see figure 1). Cr-rich films with dense columnar morphology exhibit a texture in the (200)-orientation with (111)-facets, whereas Al-rich samples show random orientation. This correlates perfectly with SEM cross-sectional images that show a fine grained morphology for Al-rich samples

Another set of Al-Cr-N thin films were synthesized using the same deposition parameters as for the Al-Cr-O-N films. The samples were characterized by means of GI-XRD at BL 9 using mar345-detector with an energy of 20 keV in October 2016. Cr-rich samples exhibit comparable texture to Cr-rich Al-Cr-O-N films with a more pronounced texture and a underdense morphology (see figure 2). Cr-rich films show a texture in the (200)-orientation, again with facets in the (111)-direction. The more pronounced texture mirrors the tilting angle of the opposing Cr- and Al-cathodes during film growth. The main difference in comparison of Al-Cr-O-N and Al-Cr-N can be found on Al-rich samples. The films exhibit a pronounced texture while Al-rich Al-Cr-O-N films show random crystal orientation. However, compared with Cr-rich films, the contribution of (111)-orientation is stronger. Again correlating the morphology by means of SEM cross-sectional images, films are more columnar and exhibit an open morphology with bigger grains. The results of these investigations clearly show, that an oxygen content in the range of 10 – 40 at.% results in a denser and finer grained morphology with random crystal orientation for Al-rich samples. The incorporation of O in Cr-rich samples results in a prefered (111)-orientation. Both increasing Al- and O-contents results in a finer morphology and shift from (200)- to (111)- to random-orientation. The results of these experiments show that GI-XRD at BL 9 provides high resolution texture information necessary for in-depth understanding of thin film micro-structures.

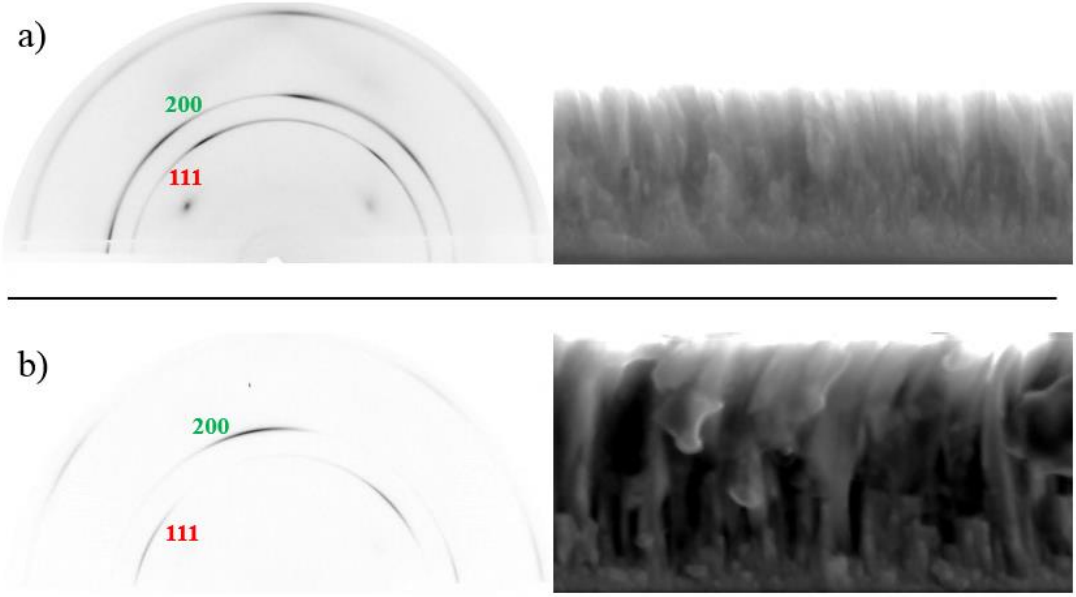

Figure 2:Diffraction patterns and SEM images of a) Al-rich Al-Cr-N and b) Cr-rich Al-Cr-N films.

DELTA user report 2016
Proposer: Prof. Dr. A. Ludwig
Co-Proposers: A. Furlan, S. Salomon, D. Grochla, L. Banko

High-throughput GI-XRD experiments on a $CoMnGe_{(1-x)}Si_x$ thin film materials library for phase analysis and correlation with phase transition properties

S. Salomon, F. Wöhrle

Werkstoffe der Mikrotechnik, Institut für Werkstoffe, Fakultät Maschinenbau

Ruhr-Universität Bochum, D-44801 Bochum

For the combinatorial investigation of the influence of Si substitution on the phase transition and the magnetic properties of the CoMnGe phase, which is known to exhibit interesting magnetocaloric properties [1,2], a $CoMnGe_{(1-x)}Si_x$ thin film composition gradient with up to 4 at.% Si was deposited by magnetronsputtering on a c-plane sapphire substrate. Preliminary XRD experiments performed in Bragg-Brentano geometry with a X'Pert Pro diffraction system by PANalytical and Cu-K_α radiation indicated that both the CoMnGe high-temperature (HT) phase and the Co_2MnGe phase are present in the thin film. However, due to an overlap of the only identifiable diffraction peaks, the (110) peak of the CoMnGe HT phase and the (220) peak of the Co_2MnGe phase, the influence of an increasing Si content on the crystal structure could not be determined. XRD(T) measurements furthermore showed that an increase of Si content has a significant influence on the phase transition properties of the thin film. For a thorough understanding of the influence of added Si on these properties, grazing incidence XRD experiments were performed at BL 9 with a beam energy of 15 keV, $\Theta = 3°$ and using a mar345 image plate detector.

***Figure 1**: 2D diffraction pattern of the thin film measurement region with ~ 2at.% Si. The two most prominent diffraction signals are correlated to the CoMnGe HT phase.*

The texture of the thin film did not change significantly with an increasing Si content. Figure 1 shows the 2D diffraction pattern of the measurement region with 2 at.% Si as an example. All diffraction signals show variations along φ, which indicates textured growth of all present phases. It can be clearly distinguished that the (102) diffraction signal of the CoMnGe HT phase shows strong intensity variations along φ. This explains the absence of this high intensity diffraction signal from the Bragg-Brentano XRD experiments. The (110) signal of CoMnGe HT phase appears to be more uniform while still showing slight intensity variations along φ. However, broadening occurs for the (110) signal where the intensity of the (102) signal

is at a minimum. This implies that the Co_2MnGe (220) signal is strongest in this orientation. The textured growth of these thin films and the resulting diffraction patterns highlight the importance of GI-XRD experiments for a thorough phase analysis.

Figure 2 shows the φ–integrated diffraction patterns for an increasing Si content with the intensity plotted over 2Θ (Cu-K_α). Because of the high beam intensity as well as the use of the image plate detector, with which the diffraction patterns of textured materials can be investigated, the measurements performed at BL 9 yield significantly more information regarding the present phases and their crystal structures than the preliminary measurements. The diffraction patterns show that not only are the CoMnGe HT phase and the Co_2MnGe phase present, but also the CoMnGe low-temperature (LT) phase and the Mn_5Ge_3 phase. With increasing Si content the (002) peak of the Mn_5Ge_3 phase decreases in intensity and cannot be identified anymore for contents of 1.7 at.% Si and above. The presence of this phase can also explain the irregular intensity changes near 39° for low Si contents. Furthermore, the intensity of the (211) peak of the CoMnGe LT phase decreases with an increasing Si content. The other diffraction peaks related to this phase show no significant variations in the composition range that was investigated. Specifically the findings related to the HT and LT phases of CoMnGe will help to explain the influences of increasing Si contents on the transition properties.

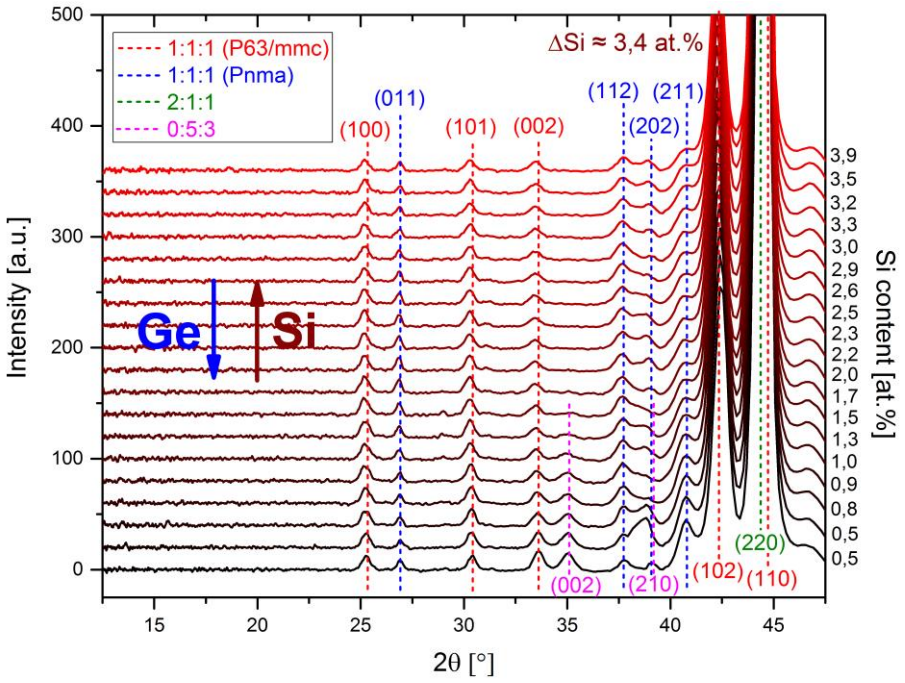

***Figure 2**: φ-integrated diffraction patterns (2Θ for Cu-K_α) of the $CoMnGe_{(1-x)}Si_x$ thin film composition gradient. The diffraction peaks are indexed according to the stoichiometry of the respective phases of (Co-)Mn-Ge (see legend).*

References

[1] J. Liu, K. Skokov, O. Gutfleisch, „Magnetostructural transition and adiabatic temperature change in MnCoGe magnetic refrigerants“, Scripta Materialia, 66, 642-645, 2012

[2] J. W. Lai, Z. G. Zheng, R. Montemayor, X. C. Zhong, Z. W. Liu, D. C. Zeng, „Magnetic phase transitions and magnetocaloric effect of MnCoGe1-xSix“, Journal of Magnetism and Magnetic Materials, 372, 86-90, 2014

DELTA user report 2016
Proposer: Prof. Dr. A. Ludwig
Co-Proposers: A. Furlan, S. Salomon, P. Decker

Structural analysis of a partial ternary Ni-Co-Al materials library to reveal the existence of martensitic phases

P. Decker

Werkstoffe der Mikrotechnik, Institut für Werkstoffe, Fakultät Maschinenbau

Ruhr-Universität Bochum, 44801 Bochum

Ferromagnetic shape memory alloys based on the materials system Ni-Co-Al are of interest as future materials in actuator devices. The bcc (Ni,Co)Al phase was found to show a martensitic transformation around the nominal composition of $Ni_{33}Co_{38}Al_{29}$ from a Pm-3m (austenite β) to P4/mm (martensite β') space group structure [1, 2]. Using combinatorial materials science methods the region of existence of the martensitic transformation shall be understood first. Furthermore, the influence of the composition on the transformation temperature needs to be clarified.

Grazing-incidence diffractometry was performed at BL 9 on a Ni-Co-Al materials library covering a partial ternary composition spread around $Ni_{33}Co_{38}Al_{29}$. 174 diffraction patterns were acquired and then integrated into two dimensional data sets (Intensity over 2θ, Cu-K_α) for an easier structural analysis. Figure 1 shows the result of a phase analysis based on this diffraction data. The β' phase is verified in a wide composition spread around the composition mentioned above. The β phase and the Cu_3Au structure type phase $(Ni,Co)_3Al$ were also found.

Figure 2 shows a two dimensional diffraction pattern of a measurement area containing the martensite phase with a composition of $Ni_{32}Co_{42}Al_{26}$. The (100), (200) β phase and the (110) β' phase rings show a locally increased intensity revealing a texture for both phases. Most of the rings however are closed and the structure is assumed to be polycrystalline. The texture information is useful to understand if texture affects the formation of phases or the martensitic transformation.

Literature

[1] P. J. Brown, K. Ishida, R. Kainuma, T. Kanomata, K.-U. Neumann, K. Oikawa, B. Ouladdiaf und K. R. A. Ziebeck, „Crystal structures and phase transitions in ferromagnetic shape memory alloys based on Co-Ni-Al and Co-Ni-Ga," *Journal of Physics: Condensed Matter,* Nr. 17, pp. 1301-1310, 2005.

[2] K. Oikawa, T. Ota, F. Gejima, T. Ohmori, R. Kainuma und K. Ishida, „Phase Equilibira and Phase Transformations in New B2-type Ferromagnetic Shape Memory Alloys of Co-Ni-Ga and Co-Ni-Al Systems," *Materials Transactions,* Bd. 42, Nr. 11, pp. 2472-2475, 2001.

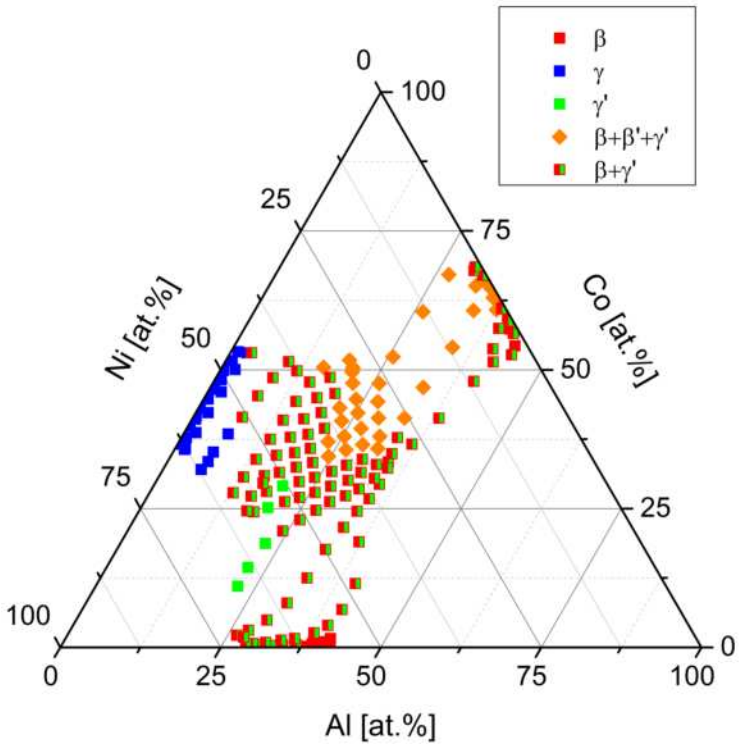

Figure 1: Results of the phase analysis on the partial ternary Ni-Co-Al materials library. The region of existence of the martensite phase β' is shown in orange.

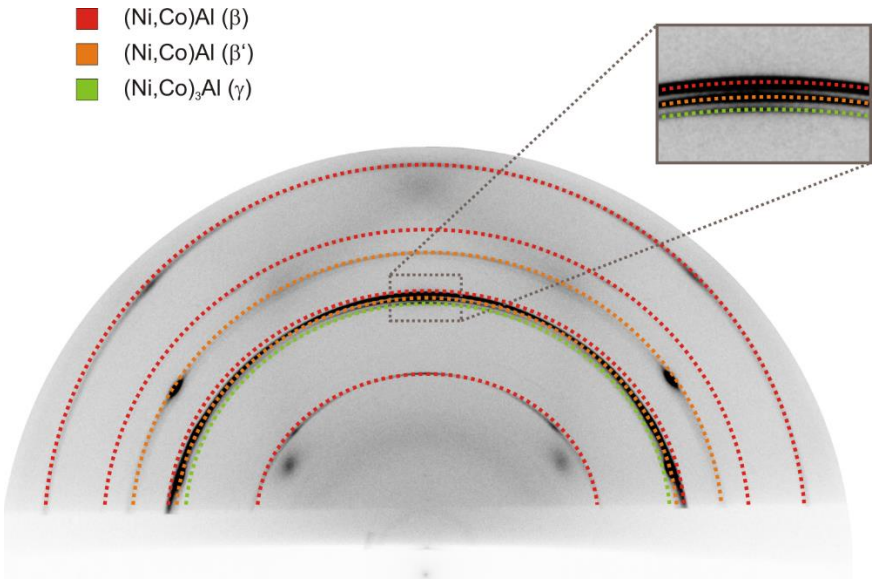

Figure 2: Two dimensional diffraction pattern of the phase region including the martensite phase with a composition of $Ni_{32}Co_{42}Al_{26}$.

DELTA user report 2016
Proposer: Prof. Dr. A. Ludwig
Co-Proposers: A. Furlan, S. Salomon, D. Grochla, L. Banko, P. Decker

High-throughput synchrotron grazing incidence XRD phase detection in Fe-Si-Ge and pure Ge thin films

A. Furlan

Werkstoffe der Mikrotechnik, Institut für Werkstoffe, Fakultät Maschinenbau

Ruhr-Universität Bochum, D-44801 Bochum

Starting in late 2015 and extending into the second half of 2016 Fe-Si-Ge thin film materials libraries and pure Ge thin films were investigated with XRD using grazing incidence geometry at BL9. We did those measurements in order to obtain the essential data about the structure and phase distribution of these thin film libraries. The Bragg-Brentano geometry of our in-house diffractometer proved inadequate for this purpose due to the fine-grained structure of films, resulting in low intensity peaks to be lost in the noise. The measurements were performed with a beam energy of 15 keV using the mar345 area detector. Fe-Si-Ge is specifically of interest for thermoelectric applications. For this project, a precise information about the phase distribution was essential. Correlating the film structure with the transport properties enables the fine-tuning of the materials properties for specific practical requirements.

For the phase analysis, peak indexing was first performed on the binary regions of the Fe-Si-Ge thin film libraries, Figure 1. The identified binary phase diffraction peaks were then compared to the peaks from diffractograms of the ternary film compositions. In this way shifts of the peaks for binary phases, due to the incorporated crystalline lattice defects, could be identified. The eventual presence of the unknown ternary Fe-Si-Ge phases was also examined.

For the film compositions containing amounts of Ge lower than ~40 at.% only binary Fe-Si phases could be detected. For such cases, diffractograms display similar patterns by means of detected peaks for wide range of compositions. The absence of diffraction peaks for Ge containing phases can have two explanations. One is that Ge, and the surplus of the other two elements, is incorporated as defects in the crystalline lattice of Fe-Si phases. The other is that Ge remained in the amorphous form. The first possibility is supported by the fact that diffraction peak shifts are observed for different film compositions, indicating different lattice parameters for different compositions. On the other hand, due to the inconclusive results from our in-house diffractometer the presence of the amorphous phase cannot be excluded. This will be verified subsequently by TEM.

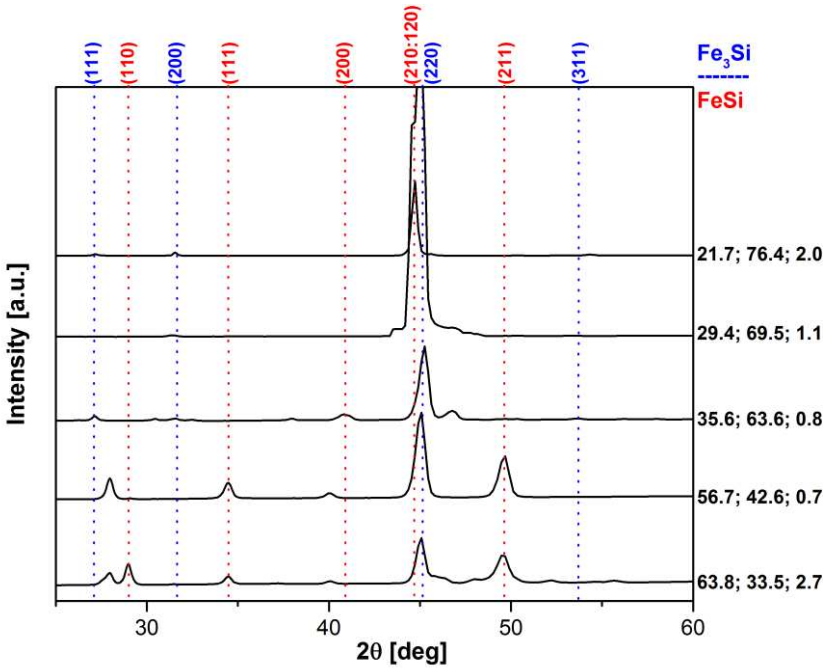

Figure 2: Synchrotron X-ray diffractograms of Fe-Si-Ge libraries for different, predominantly binary Fe-Si, film compositions. Single element contents are given in at.% for Si, Fe, and Ge respectively.

Particularly interesting was the detection of the low intensity peaks for ternary compositions containing high amounts of Ge. For such compositions, the diffractograms show densely packed peaks that were not possible to detect by our in-house diffractometer (Bragg-Brentano), Figure 1, Figure 3. Such peak distribution is characteristic for FeGe, $Fe_{6.5}Ge_4$, and Fe_6Ge_4 phases. Synchrotron XRD mapping was

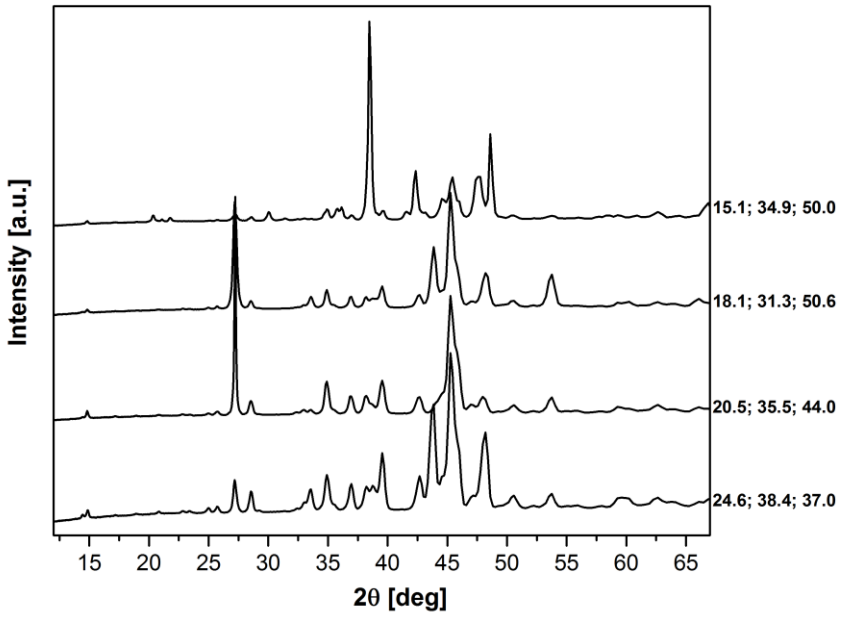

Figure 1: Synchrotron X-ray diffractograms of Fe-Si-Ge libraries for different film compositions with high contents of Ge. Multitude of peaks indicates possible presence of FeGe, $Fe_{6.4}Ge_4$, and Fe_6Ge_5 phases. Single element contents are given in at.% for Si, Fe, and Ge respectively.

performed for up to 91 measurement areas with film compositions for different Fe-Si-Ge thin film libraries. The diffractograms were subsequently grouped according to their type, which gave the indication of phase formation in dependence of film composition. Moreover, the grazing incidence geometry of the synchrotron diffractometer eliminated the peaks characteristic for the sapphire substrate.

The obtained results indicate that the investigated ternary films do not crystallize well. A highly textured structure is formed only for a very narrow range of compositions. The data obtained by the synchrotron

Figure 3: 2D synchrotron GI-XRD pattern for Fe-Si-Ge ternary with high proportion of Ge.

diffraction were essential for this project, since the use of conventional XRD measurements (Bragg-Brentano) proved to be inadequate. In Bragg-Brentano geometry, only the strongest diffraction peaks of the Fe-Si phases and Ge-Si solid solutions could be identified, while no information about Fe-Ge structures was obtained.

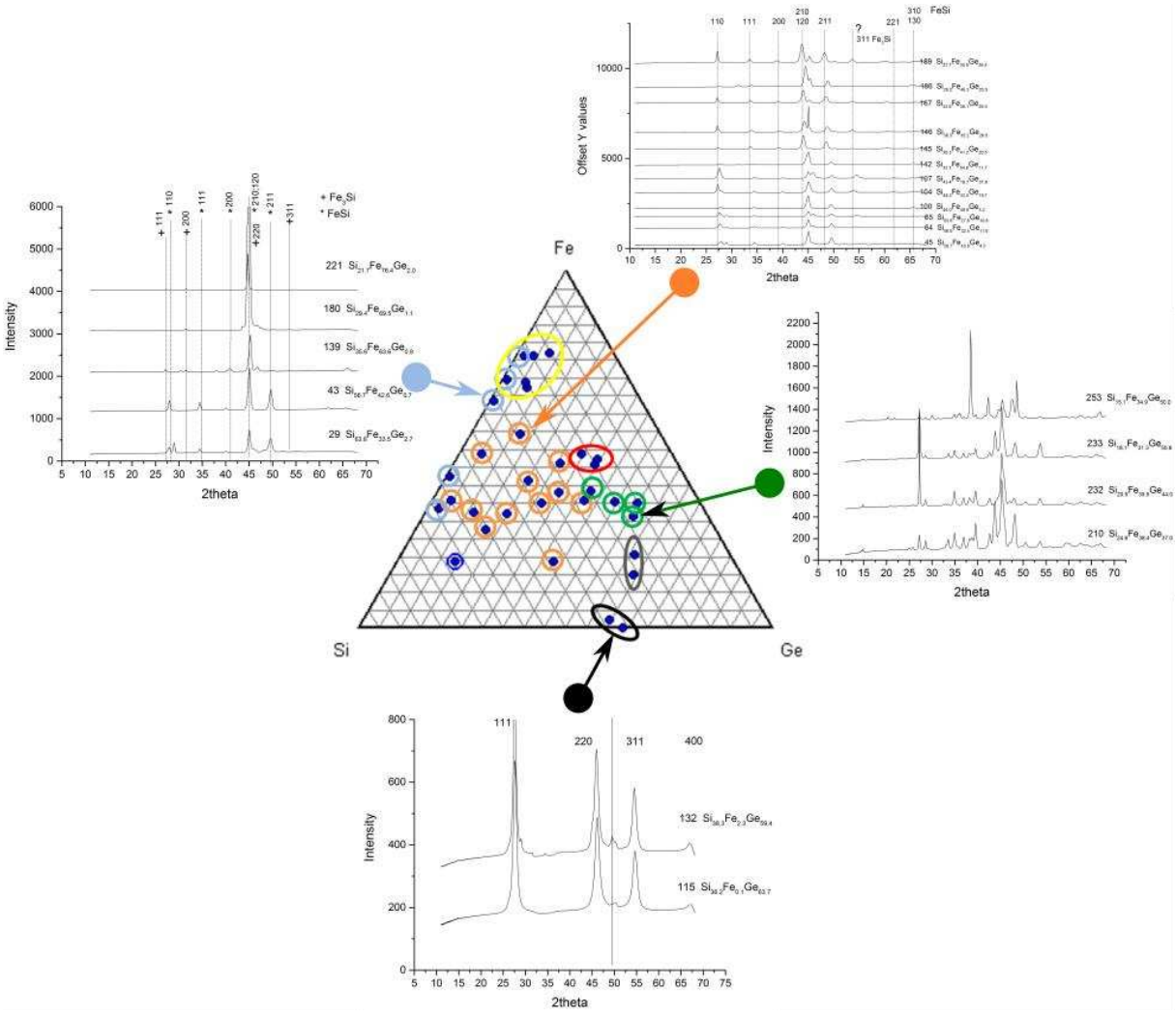

Figure 4: Synchrotron X-ray diffractograms grouped according to type for different ranges of Fe-Si-Ge film library compositions.

Thermal induced lattice distortion of diluted magnetic semiconductors

H. Göhring, M. Paulus, T. Büning, C. Sternemann, S. Bieder, M. Bayer, M. Tolan

Fakultät Physik/DELTA, Technische Universität Dortmund, 44221, Germany

Diluted magnetic semiconductors which combine the properties of semiconductors and ferromagnets have been an important subject in materials science. Semiconductors with Curie temperatures above room temperature could revolutionize the field of spintronics by allowing control of the magnetization via application of voltage as observed e.g. for the ferromagnetic material galfenol [1]. Magnetic semiconductors, which are currently under investigation, still show a rather low Curie temperature making them inapplicable for technical use. However, GaMnAs seems to be a promising candidate for high Curie temperature material. GaMnAs is typically grown epitaxially on GaAs substrates with a limited manganese content of a few percent, as higher Mn contents cause the formation of Mn nanocrystals. This system was studied intensively in the past years. Starting at Curie temperatures of around 60 K, special hybrid systems containing GaMnAs show ferromagnetic behaviour up to temperatures of 200 K [2]. A detailed knowledge about the interrelation between structural properties and magnetism is still not existing for these systems.

To overcome this lack of knowledge high resolution x-ray diffraction experiments were performed at beamline BL9 of DELTA using a photon energy of 13 keV and a flow cryostat setup operated with liquid nitrogen. In order to minimize vibrations due to the nitrogen transfer tube the cryostat is connected to the diffractometer using ball bearings which ensure

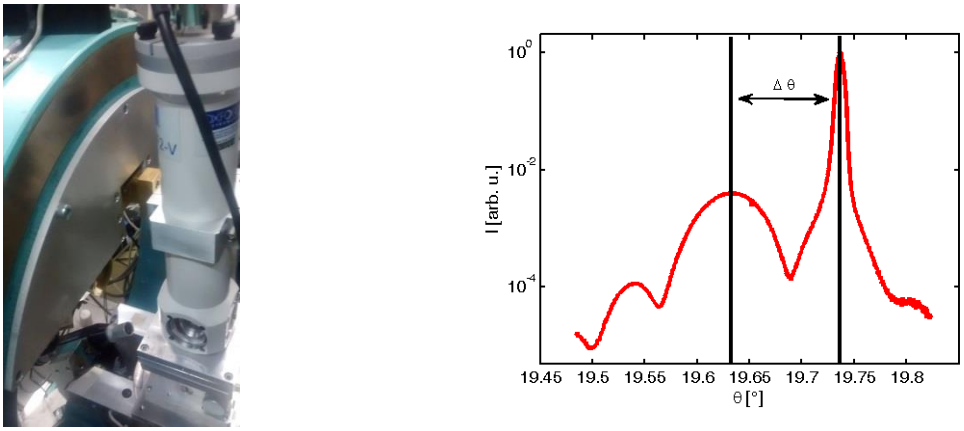

Figure 1: Left: The cryostat is mounted on a Huber Z-stage and connected to the diffractometer via ball bearings to minimize vibrations to the system. Right: Measured (004) Bragg rod of the 120 K sample. The relative changes between the Bragg peak position of the GaAs substrate and GaMnAs layer Δθ are investigated.

an excellent steadiness on the one hand and still allow sample movement along the z-axis on the other. The left side of figure 1 shows a photo taken of the experimental setup. A PILATUS 100K detector was used for data acquisition. Two samples with Curie temperatures of 60 K and 120 K were investigated. The goal of our experiment was to detect structural changes due to magnetostriction passing the Curie temperature. The small changes in the GaMnAs lattice were determined by measuring both, the GaAsMn (004) and the GaAs (004) reflection of the substrate which serves as an internal reference. Because of the liquid nitrogen measurements were carried out over a limited temperature range of 80 K to 160 K not reaching the Curie temperature of the 60 K sample. In order to observe the phase transition of the 60 K wafer

complementing experiments were carried out at beamline BM28 of the ESRF, utilizing liquid helium as a cooling agent.

A Bragg rod measured with the 120 K sample is displayed on the right side of figure 1. To investigate the structural changes due to magnetostriction, the thermal effect on the lattice has to be separated. The separation can be achieved in a first step of the data analysis by determining the relative changes Δθ between the GaAs and GaMnAs (004) Bragg peak

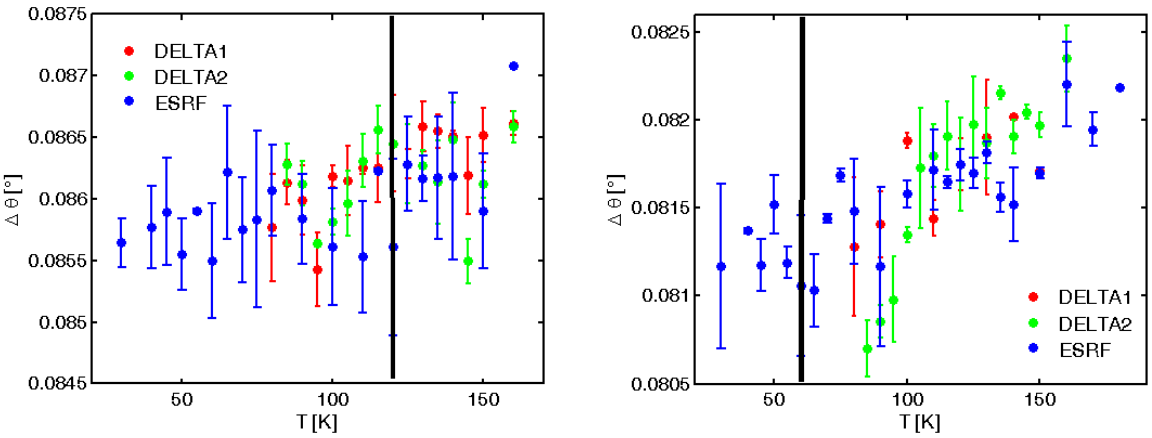

Figure 3: The angular separation Δθ between the GaAs and the GaMnAs (004) Bragg reflection. Red, green and blue points represent the experimental data taken at DELTA and ESRF, respectively. The black lines mark the Curie temperatures. All data sets are normalized at 125 K.

positions. For this purpose the (004) GaAs peaks were shifted to the same value for every scan. In a second step the position of the (004) GaMnAs Bragg peak was determined by fitting a Gaussian curve to the data. The results presented in figure 3 shows the averaged angular separation Δθ for the wafer with a Curie temperature of 120 K and 60 K on the left on the right, respectively. Both samples show linear behavior of the angular separation on the temperature within the accuracy of the experiment. There are no indications of structural changes exceeding the Curie temperature, which leads to the conclusion that the GaMnAs layer is strongly pinned to the substrate and therefore hindering the magnetostriction effect on the lattice distortion within the experiments' resolution of $2 \cdot 10^{-3}$Å.

Reference:

[1] D. E. Parkes, S. A. Cavill, A. T. Hindmarch, P. Wadley, F. McGee, C. R. Staddon, K. W. Edmonds, R. P. Campion, B. L. Gallagher and A. W. Rushforth, *Non-volatile voltage control of magnetization and magnetic domain walls in magnetostrictive epitaxial thin films*, Appl. Phys. Lett. **101**, 072402 (2012).

[2] A. M. Nazmul, T. Amemiya, Y. Shuto, S. Sugahara and M. Tanaka, *High temperature ferromagnetism in GaAs-based heterostructures with Mn delta doping*, Phys. Rev. Lett. **95**, 017201 (2005).

Acknowledgement:

We would like to thank the machine groups of DELTA and ESRF for providing synchrotron radiation and technical support. We thank Xinyu Liu for preparing and providing the samples at University of Notre Dame, Indiana and Didier Wermeille for the support at BM28. Holger Göhring acknowledges the support by BMBF through grant no. 05K12PE1 and the DFG through TRR160. Thomas Büning is funded by the BMBF within the FSP-302 with grant no. 05K13PE2 and Mercur AN-2014-0036.

X-ray diffraction analysis of $MAPbBr_3$ layers grown onto $MAPbCl_3$ substrates

Neda Pourdavoud[a], Thomas Riedl[a], Behnam Khanbabaee[b] and Ullrich Pietsch[b]

[a]Lehrstuhl für Elektronische Bauelemente, Bergische Universitaet Wuppertal, [b]Festkörperphysik, Universität Siegen.

Organo-metal halide perovskites have revolutionized thin-film photovoltaics as efficiencies were skyrocketing to levels >20%. With optoelectronic properties almost at par with the most successful inorganic semiconductors such as GaAs, organo-metal halide perovskites also state an intriguing platform for light emitting diodes (LEDs) and lasers. Strikingly, single crystals of these materials can be grown at relatively low temperatures from a precursor solution with outstanding material quality. This seeds the prospect to grow heterostructures of perovskites with a different bandgap on top of each other by low-temperature solution epitaxy, e.g. $MAPbBr_3$ (E_g = 2.3 eV) onto $MAPbCl_3$ (E_g = 3.1 eV). Thereby, device structures for LEDs and lasers based on these materials are envisaged.

The diffraction experiments have been performed at BL10 of DELTA using x-ray of 13keV and a Pilatus detector. Samples 5, 100 and 200µm thickness of $MAPbBr_3$ grown onto $MAPbCl_3$ substrate were probed under fixed angle of incidence and the diffraction pattern was probed at different exit angles of the Pilatus detector, and subsequently composed to a common diffraction diagram. Both materials crystallize in a cubic structure but show a lattice mismatch of about 4 percent. It was found that independent from the layer thickness both materials display their own diffraction pattern, i.e. no epitaxial condition could be observed. However, possible epitaxy close to the layer to substrate interface can be probed by using incidence angles close to the critical angle of total external reflection which become accessible measuring sample with layer thickness below one micron.

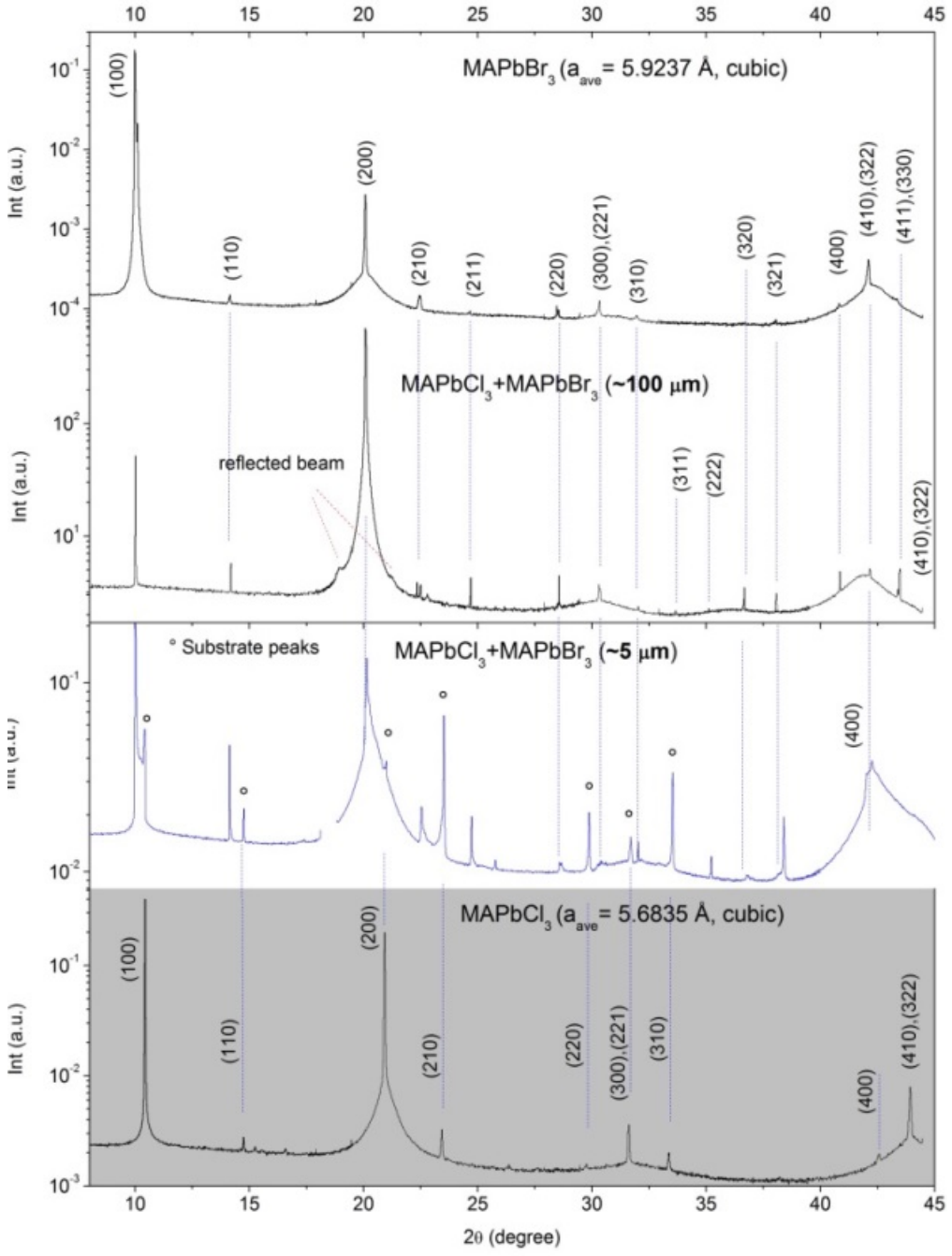

Fig. 1: Diffraction pattern of pure $MAPbBr_3$(top) and $MAPbCl_3$ (bottom) and samples with 100µm and 5 µm layer thickness

Comparison of thermal induced lattice expansion of GaAs and (In,Ga)As/GaAs quantum dots

H. Göhring, M. Paulus, C. Sternemann, T. Büning, M. Bayer, M. Tolan

Fakultät Physik/DELTA, Technische Universität Dortmund, 44221, Germany

Self-assembled (In,Ga)As quantum dots (QDs) are crystalline inclusions on the scale of ten nanometers that are embedded in a GaAs matrix. Like atoms, carriers residing in QDs have discrete energy levels due to their three-dimensional confinement. The excellent optical quality of such systems has allowed studies on fundamental problems of light-matter-interaction and has paved also the way of QDs into applications as light emitters, ranging from single photon sources to high-power laser diodes [1, 2].
Tiemeyer et al. investigated the lattice distortion of (In,Ga)As/GaAs quantum dots induced by polarons of excited carriers for the first time utilizing high resolution x-ray diffraction [3]. They found a tetragonal distortion of the GaAs crystal lattice if QDs are present and attribute this anisotropic distortion to polaronic effects initiated by the optically excited QDs. However, the possibility remained that the observed distortion can be assigned to a pure thermal effect.

To rule out the pure thermal effect as an explanation high resolution x-ray diffraction experiments were performed on two samples with a photon energy of 15 keV at beamline BL9 at DELTA and a helium flow cryostat setup run on liquid nitrogen. The cryostat was connected to the diffractometer using ball bearings which ensure an excellent steadiness on the one hand and still allow sample movement along the z-axis on the other. A PILATUS 100K detector was used for data acquisition. The investigated samples were the same ones used in the work by

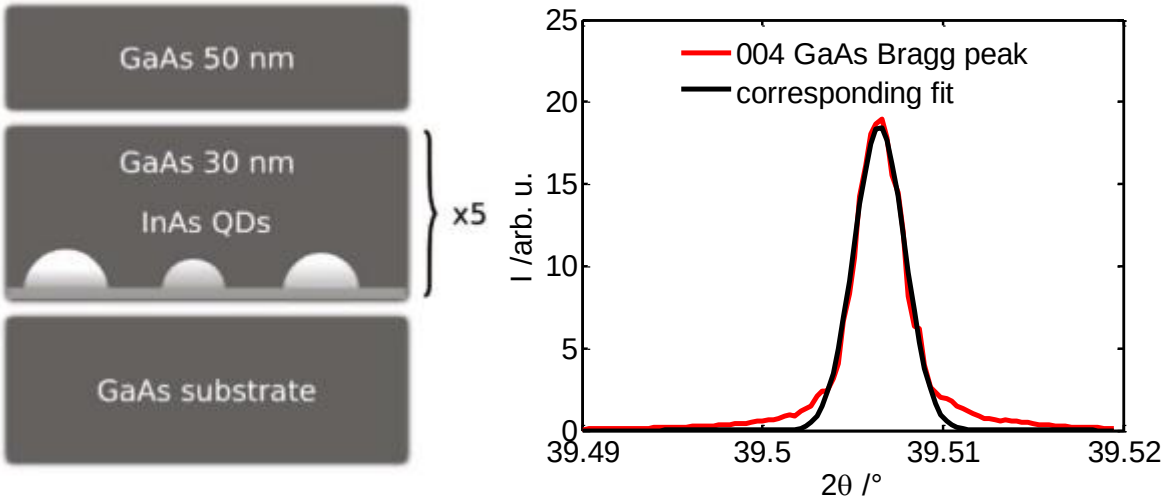

Figure 1: Left: Sketch of the QD sample consisting of a GaAs substrate, a (In,Ga)As multilayer structure and a capping layer [3]. Right: Measured GaAs (004) Bragg peak at a temperature of 100 K in red and a corresponding gaussian fit.

Tiemeyer et al; one GaAs wafer and an (In,Ga)As/GaAs QD multilayer structure grown on a (001) oriented 500 nm thick GaAs substrate. The multilayer counts 5 layers each consisting of a 1.9 monolayer thick InAs layer capped with 30 nm of GaAs, which is sketched on the left side of figure 1.
In order to determine the thermal Impact on the crystals' lattice distortion the (002) and (004) Bragg peaks of both samples was detected in a temperature range between 100 K and 125 K. This range was chosen, because the samples were also investigated at 100 K under optical

excitation. A typical scan is depicted in figure 1 on the right side. The change in lattice constant is obtained by investigating the differences $\Delta\theta$ between the (002) and (004) Bragg reflections. The measured change of the perpendicular lattice constant $\Delta a/a_S$ normalized by the measured 100 K lattice constant is shown in figure 2 (see also [3]). To ensure sufficient statistics we measured each data point four times consecutively. The linear regression to the data reveals slopes of $1.26 \pm 1.4 \times 10^{-5}\, K^{-1}$ and $1.13 \pm 1.4 \times 10^{-5}\, K^{-1}$ for the QDs and GaAs, respectively. Therefore, we conclude that the thermal lattice expansion is hardly modified by the included QDs within the experimental resolution. The change in slope yields a lattice constant difference between the QD and GaAs sample in the order of 1×10^{-5} for $\Delta T = 10$ K. The thermal expansion of the lattice constant however, is found to be in the order of 1×10^{-4} for the same temperature range. Comparing these findings to the elongation observed under optical excitation with P ($\Delta a/as \sim 0.5 \times 10^{-5}$) we estimate the laser induced lattice heating to be about 1 K. It is therefore, highly unlikely to assign the tetragonal distortion to a pure thermal effect.

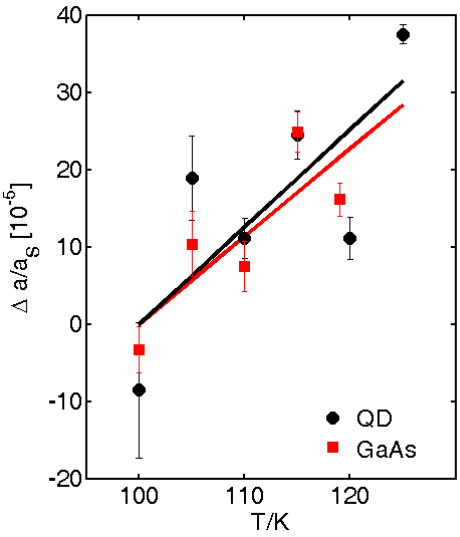

Figure 2: Thermal expansion of GaAs and the QD sample in (001) direction. The temperature was varied between 100 K and 125 K in the vicinity of the samples' temperature investigated in [3].

The findings of this beamtime were used to clarify and support the outcomes of Tiemeyer et al. and resulted in a publication in Nanotechnology [3].

Reference:

[1] D. Bimberg, M. Grundmann, and N. N. Ledentsov, *Quantum dot heterostructures*, (John Wiley & Sons, Ltd., New York, USA, 1998).

[2] *Single Quantum Dots: Fundamentals, Applications and New Concepts*, ed. by P. Michler, *Topics in Applied Physics*, (Springer, Heidelberg, Germany, 2004). *Single Semiconductor Quantum Dots* (NanoScience and Technology), ed. by P. Michler, *NanoScience and Technology*, (Springer, Heidelberg, Germany, 2009).

[3] S. Tiemeyer, M. Bombeck, H. Göhring, M. Paulus, C. Sternemann, J. Nase, F. J. Wirkert, J. Möller, T. Büning, O. H. Seeck, D. Reuter, A. D. Wieck, M. Bayer and M. Tolan, *Polaron-induced lattice distortion of (In,Ga)As/GaAs quantum dots by optically excited carriers,* Nanotechnology, **27**, 425702(2016).

Acknowledgement:

We would like to thank the machine groups of DELTA and ESRF for providing synchrotron radiation and technical support. Holger Göhring acknowledges the support by BMBF through grant no. 05K12PE1 and the DFG through TRR160. Thomas Büning is funded by the BMBF within the FSP-302 with grant no. 05K13PE2 and Mercur AN-2014-0036.

Structural and Spectroscopic Analysis of Lanthanide doped Nanoparticles

Mahmoud Al Humadi [a], Julie Gai [b], Claudia Wickleder [b], Ullrich Pietsch [a]

[a]Solid State Physics, University of Siegen, [b]Inorganic Chemistry, University of Siegen

The inorganic chemistry group of Siegen university synthesizes crystalline materials doped with Lanthanide ions as luminescent material. Although one can expect that the formed crystal field around the dopant changes the luminescence energy this effect was never experimentally confirmed. The samples used for this propose was Sc_2O_3 doped by (1.3.5.7.9 and 15) % Eu^{3+}. The structure investigations have been performed by X-ray powder diffraction analysis performed at BL P10 at DELTA synchrotron in Dortmund using photon energy of 12 KeV and a Pilatus 2D detector. The beam size was 4.0 * 0.5 mm^2 (horizontal * vertical). The sample to detector distance was 412 mm.

Detailed investigation of diffraction patterns revealed retention of the Sc_2O_3 lattice but the appearance of new Bragg peaks shifting linear with doping concentration (Fig. 1). From the same samples we measured the Eu^{3+} PL energy where selected transition displayed a PL-shift as function of dopant concentration as well. By combining XRD and PL data we could associate the measured PL shifts by the local strain field around the Lanthanide ions for the first time.

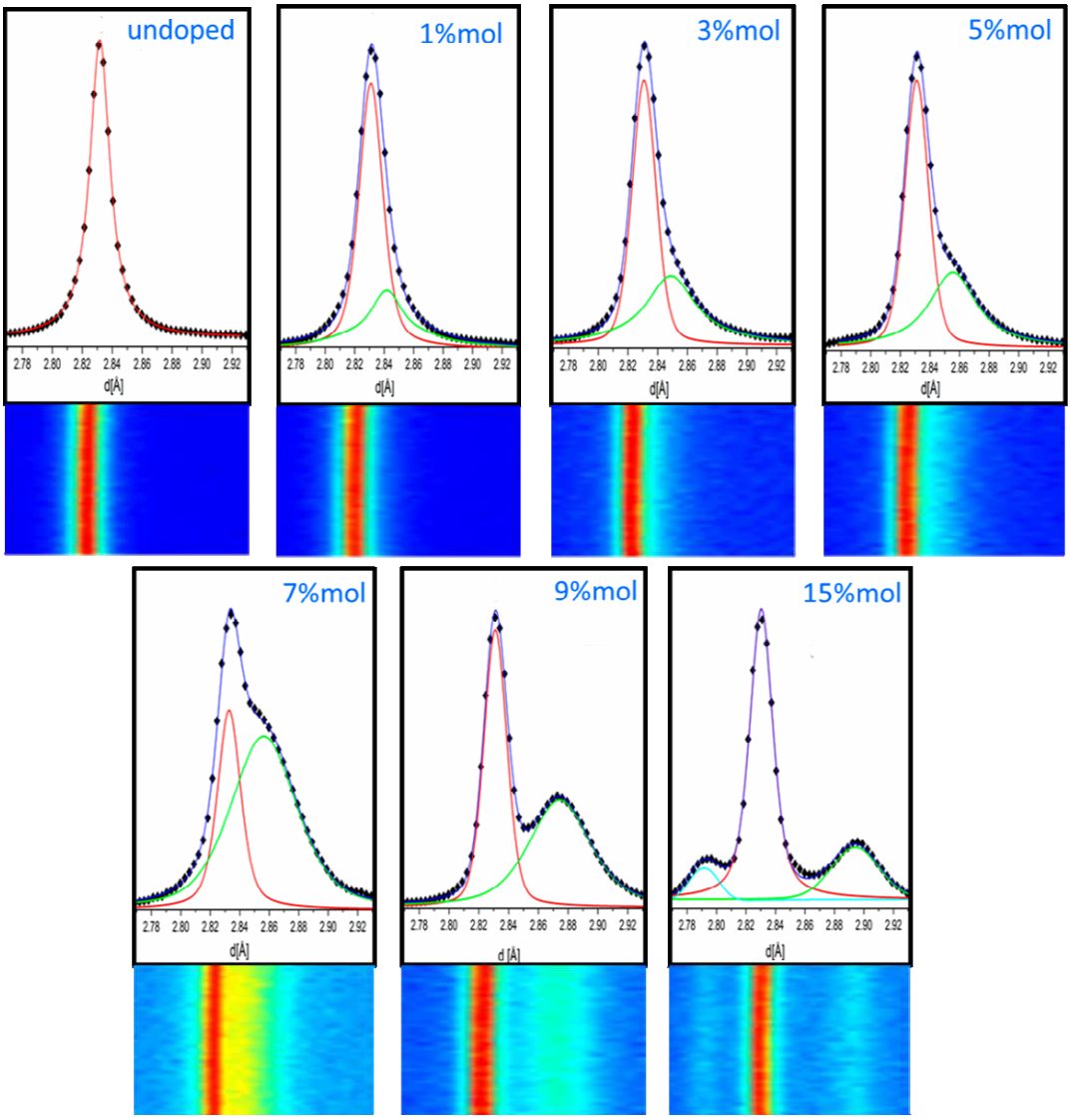

Figure 1: Shifting of (222) XRD peak with increase Eu^{3+} concentration.

Short-time nitridation of electroplated chromium coatings in SiH_4-doped N_2-atmosphere analysed by GIXRD

D. Wulff[a], U. Holländer[a], D. Lützenkirchen-Hecht[b], A. Langohr[a], K. Möhwald[a], H.J. Maier[a]

a) Institut für Werkstoffkunde, Leibniz Universität Hannover, An der Universität 2, 30823 Garbsen
b) Fakultät 4 - Physik, Bergische Universität Wuppertal, Gaußstr. 20, 42097 Wuppertal

Introduction

Within the scope of a funded project concerning the development a combined brazing-nitriding process for the production of water-cooled, bipolar plates for PEM fuel cells, nitriding processes of chromium coated metal sheets during a furnace brazing process at different temperatures were investigated. Here we employed GIXRD in order to study short-time nitriding of electroplated chromium coatings on copper. The samples were heat treated in a conveyor belt furnace in monosilane (SiH_4)-doped N_2 atmosphere at 900 °C, 950 °C and 1000 °C and a dwell time of 15 min, Figure 1. For the GIXRD measurements a PILATUS 100K was used. The measurements have been performed at DELTA BL 10 [1] using an energy of 10 keV and a detector threshold of 8.5 keV to eliminate the contributions of fluorescence radiation from the samples to the recorded diffraction patterns. The incidence angle have been varied between 1° and 8°, while the PILATUS detector has been fixed at diffraction angles of 28° or 43°, respectively.

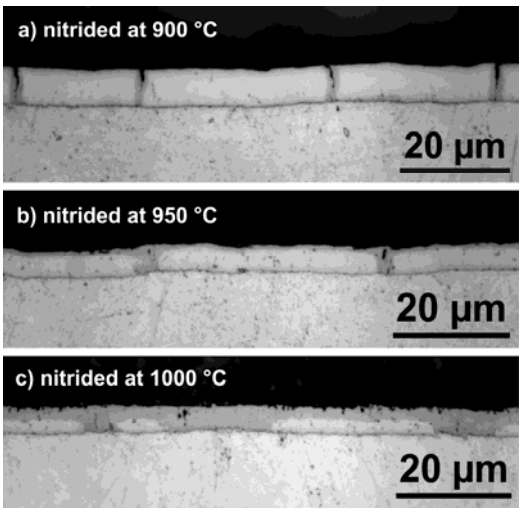

Figure 1: Light microscopic images of cross sections from samples heat treated at different temperatures in a conveyor belt furnace using SiH_4-doped N_2.

Results

In Fig. 2, GIXRD patterns of the samples collected at an incident angle $\Theta = 2°$ are presented. The penetration depth at this angle is of about 700 nm. The patterns of the native untreated sample only show a Cr-bcc reflex (♥) at 35.1°. The peak intensity is relatively small and the full width at half-maximum is rather large. Furthermore, the intensities of the reflexes do not increase with higher incident angles. Therefore it can be concluded that the native chromium layer (as electroplated) mainly consists of crystalline metallic Cr. Every pattern of the three heat treated samples show a peak quintet at 44.7° (112), 34.2° (111), 32.4° (002), 30.0° (110) and 23.6° (101), which can be clearly assigned to Cr_2N (♦). In the case of the sample heat treated at 1000°C and 950°C, the Cr_2N (♦) peak at 34.2° is the major reflex. At higher incident angles, the reflex at 44.7° (112) becomes the most intensive Cr_2N reflex. So it can be assumed that the preferred crystallographic orientation of Cr_2N changes within the surface layer of these samples. In the patterns of the sample heat treated at 950°C, the Cr reflex is also visible at each incident angle down to 1°. Either a very thin Cr_2N layer is located on top of the chromium, because the penetration depth at 1° is noticeably larger than the thickness of the Cr_2N layer, or significant amounts of metallic chromium are not transformed and still existing in the top layer, such that a mixture of Cr_2N and Cr is present at the surface. In contrast, all patterns of the sample heat treated at 1000°C do not show any Cr metal reflexes for incident angles below 3.5° with an X-ray penetration depth of about 1.3 µm. Assuming that the total

signal measured with the detector originated from a depth of three times the penetration depth, the thickness of the formed surface layers can be estimated to be about 3 * 1.3 µm = 4 µm.

Furthermore it can be assumed that at 950 °C and temperatures above, a recrystallization of the Cr took place. The presumption is supported by the fact that the integral intensity of the Cr reflex in patterns of the sample treated at 950°C is obviously higher than that of the native sample, although a significant amount of Cr_2N has formed on this sample and the primary x-ray intensity was almost identical.

On sample 1 (900 °C) no change in the preferred crystallographic orientation of Cr_2N can be detected. The reflex at 44.7° (112) is still dominant at 8°. A Cr reflex is detectable for every incident angle and its intensity increases with higher incident angles. From the data it can be concluded that 900 °C are not sufficient to prepare a dense layer of Cr_2N on the surface. Three very weak peaks at 26.9°, 29.0° and 43.5° can be seen at all the patterns of the heat treated samples especially for small incident angles. These can be assigned to Cr_2O_3 (♣), from which traces seem to be present on or near the surface. Such a formation of Cr_2O_3 had been detected previously when heat treating stainless steel under similar process conditions [2]. It is quite unclear at what instant of time (heating, cooling, during first contact with air upon leaving the furnace) the formation of Cr_2O_3 happened. In this context it is important to emphasize that obviously no equiatomic CrN had been formed within the temperature range investigated, although this reaction product would be thermodynamically preferred rather than Cr_2N [3]. Due to the short process time, thermodynamic equilibrium conditions are possibly not attained, and the formation of CrN is in addition less favored by kinetics. With a view on possible applications, this is a promising result, since Cr_2N provides a good corrosion protection and an electric contact to the substrate, which are both essential features for bipolar plates.

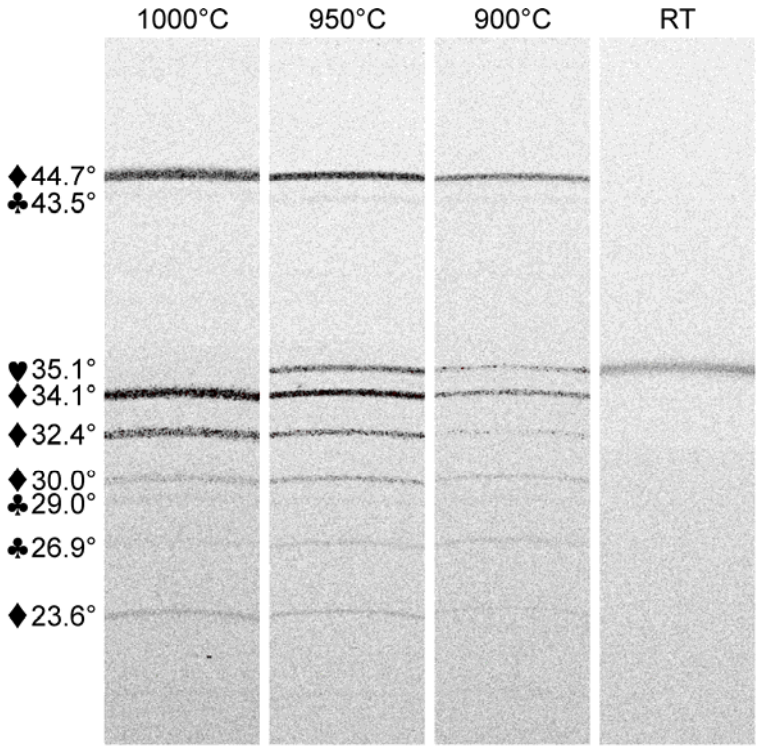

Figure 2: GIXRD patterns of samples heat treated at 1000 °C, 950 °C and 900 °C and an untreated Cr-coated reference sample (RT) collected at an incident angle of Θ = 2°. The peaks have been assigned as follows: Cr (♥), Cr_2N (♦) and Cr_2O_3 (♣).

Acknowledgements

The research is funded by German Federation of Industrial Research Associations (AIF, grant number 18.422B). The authors gratefully acknowledge the DELTA machine group for providing reliably synchrotron radiation. Special thanks go to R. Wagner for his help with the measurements at the beamline.

References

[1] D. Lützenkirchen-Hecht, R. Wagner, S. Szillat, A. K. Hüsecken, K. Istomin, U. Pietsch, R. Frahm, J. Synchrotron Rad. 21 (2014) 819-826.

[2] D. Lützenkirchen-Hecht , D. Wulff , R. Wagner, R. Frahm, U. Holländer, H. J. Maier, J. Mater. Sci. 49 (2014) 5454-5461.

[3] J.G. Buijnsters, P. Shankar, J. Sietsma, J.J. ter Meulen, Mater. Sci. Eng., A 341 (2003) 289-295.

Temperature-induced Formation of Lubricous Oxides

in Vanadium-doped Arc Sprayed Coatings

Wolfgang Tillmann[a], Leif Hagen[a], David Kokalj[a], Dominic Stangier[a], Michael Paulus[b], Metin Tolan[b]

[a]Institute of Materials Engineering, TU Dortmund University, Germany

[b]Fakultät Physik / DELTA, TU Dortmund University, Germany

Introduction

Transition metals (W, Mo, Ti and V) form structures of the Me_nO_{2n-1}-, Me_nO_{3n-1}- or Me_nO_{3n-2}-type with recurring vacancies under thermal load and oxidizing environment [1]. The formation of those reactive films in sliding contacts under elevated temperature provides enhanced tribological properties such as decreased frictional forces. In terms of coating technologies, Bobzin et al. [1] emphasize the relevance of vanadium for lubrication. Regarding vanadium oxides, vanadium pentoxide (V_2O_5) shows the lowest melting temperature (melting point: 678°C [2]; 670°C [3]) of the vanadium oxides and can consequently act above the melting point as solid lubricant with a certain liquid amount [4]. It is also a promising candidate for friction reduction at operating temperatures below the melting temperature, due to its low decohesion energies G [1].

In terms of thin film technologies, vanadium-doped PVD coatings have already been studied by numerous authors with respect to their tribological behavior. In contrast, the triblogical behavior or rather the coating characteristics of vanadium-doped arc sprayed coatings have not been examined yet. The aim of this study was to characterize iron-vanadium coatings deposited by the Twin Wire Arc Spraying (TWAS) process with respect to their oxidation behavior at elevated temperatures and to correlate the formation of oxides to the tribological properties observed in dry sliding experiments.

Experimental

As substrate material round C45 steel specimens with a diameter of 40 mm and thickness of 6 mm were employed. Before spraying, the surfaces of the samples were sand blasted with corundum and afterwards cleaned in an ultrasonic bath filled with ethanol. As feedstock material two different cored wires (Fa. Durum Verschleissschutz, Germany) with a diameter of 1.6 mm were used. The vanadium doped cored wire (referred to as “Fe-V”) consists of approximately 29.9 wt.% of V (in wt.%: 0.07 C, 0.25 Mn, 0.33 Si, 0.38 Al, 29.91 V, Bal. Fe). As opposed to that, a low carbon steel wire delivered as cored wire (in wt.%: 0.07 C, 0.11 Si, 0.25 Mn, Bal. Fe) serves as a reference (referred to as “Fe-Fe”). In order to deposit the coatings, the Smart Arc 350 PPG spraying system (Fa. Oerlikon Metco, Switzerland) was utilized. **Table 1** summarizes all parameter settings which have been employed for deposition of both feedstock materials. The layers were produced by applying two overruns for each specimen.

Tab. 1: *Spray parameter settings*

Handling parameters		**Spray parameters**	
Spray angle [°]	90	Voltage [V]	28
Spray distance [mm]	95	Current [A]	180
Gun velocity [m/s]	200	Primary gas pressure [MPa]	0.6
Track pitch [mm]	5	(compressed air)	

To investigate the tribological behaviour of the coatings, high temperature ball-on-disk (BOD) tests at 25°C and from 350°C up to 750°C in 100°C steps were performed with the "HighTemperature Tribometer" (Fa. CSM, Switzerland). The surface of all samples was machined and polished. An alumina ball (2300 HV) with 6 mm diameter and a load of 5 N was used as a counterbody. A sliding distance of 200 m without lubricant was employed. The velocity was kept at 40 cm/s and the radius of the circular path was maintained constant at 10 mm. The phase composition of the coating was analyzed via x-ray diffraction at beamline BL9 of the synchrotron light source DELTA. The samples were annealed up to different temperatures (350°C, 450°C, 550°C, 650°C, 750°C) utilizing a heat plate with graphite dome, type DHS 1100 (Fa. Anton Paar, Austria). The photon energy was set to 27 keV (wavelength λ = 0.4592 Å) and a MAR345 image plate detector was used for the detection. The beam size was set to 0.1 x 1.0 mm^2 (v x h) and the angle of incidence was 5 degrees. The diffraction patterns were obtained from the MAR images using the FIT2D program package [5]. Afterwards the 2 Theta scale of the diffraction patterns was converted to a wavelength of λ = 1.5406 Å.

Results

In terms of dry sliding experiments, both coating systems show a different tribological behavior along the investigated temperature range. Within elevated temperature a decrease of the coefficient of friction (COF) of the Fe-V-coating is observed. In particular, above 550°C the COF diminishes significantly. In contrast, the COF of the Fe-Fe-coating remains constant over the whole temperature range. Up to 450°C the Fe-Fe coating showed a lower COF when compared to the Fe-V coating. Nevertheless, the Fe-V coating exhibits a friction reduction of 42% at 750°C in contrast to the Fe-Fe-coating.

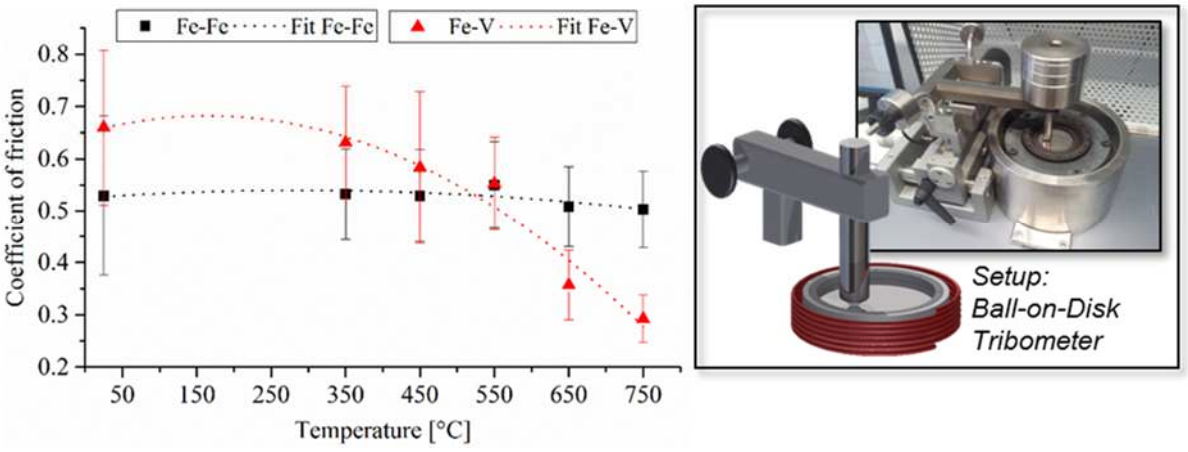

Fig. 1: *Coefficient of friction of different specimens for various temperatures taken in dry sliding experiments*

Figure 2 shows the diffraction patterns of the Fe-V-coating taken at different temperatures in the range of 25°C up to 750°C. After coating deposition V_2O_3, VO and Fe_3O_4 can be detected. Below 550°C no significant changes are observed during annealing with respect to the formation of oxide phases. Above 550°C the intensity of Fe_3O_4 (magnetite) decreases (30.1°, **Fig. 2a**), which means that the amount of Fe_3O_4 decreases in the coating. On the other hand, the strongest increase of the intensity of Fe_2O_3 (hematite) can be seen above 550°C (24.2°, **Fig. 2a**). Considering thermodynamic aspects, the occurrence of Fe_2O_3 due to annealing is more likely than Fe_3O_4 [6] and accordingly Fe_2O_3 is the thermodynamically more stable oxide in this temperature range. Vanadium oxides (V_2O_5, VO_2) and Fe-V-rich oxides ($Fe_{0.11}V_2O_{5.16}$, $Fe_{0.75}V_{0.75}O_{5.16}$, $FeVO_4$) are formed under thermal load and oxidizing environment as seen above 550°C. In the case of VO_2, the structure is not clearly identifiable. In **Fig. 2a** and **2b** the positions and relative intensities of the Bragg peaks of monoclinic (14), tetragonal (136) and orthorhombic (62) VO_2 are shown and match to the peaks of the coating. VO_2 features a metal-insulator transition at 68°C from tetragonal to monoclinic structure [7]. Since there is no difference between the plots at 25°C and 350°C, it can be assumed that only one

phase is present. The VO_2 peak of the coatings occurs only above 550°C and therefore it can be stated that the tetragonal phase is only included. But it is also reported, that the transition temperature can shift, if stresses are existing in the coatings [8]. The presence of the orthorhombic phase is unlikely because this phase arises only at pressures larger 13.7 GPa as reported by Bai et al. [9].

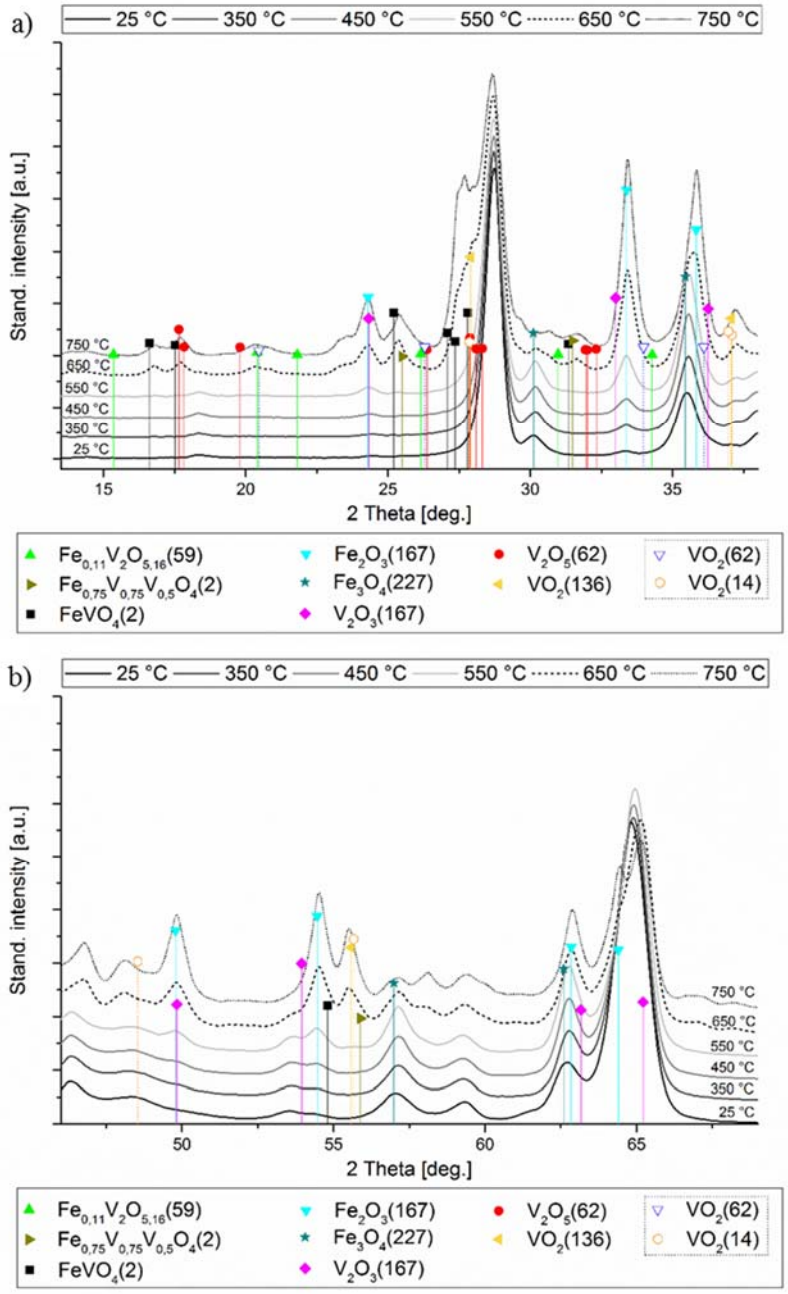

Fig. 2: *XRD pattern of the Fe-V coating obtained under different temperatures (25°C, 350°C, 450°C, 550°C, 650°C, and 750°C) in the 2 Theta range of a) 13.5°-38°, and b) 46°-69°. The 2 Theta axis is scaled to a photon energy of 8 keV. Space group numbers are indicated in parenthesis*

XRD-analyses show that the Fe-V-coating forms different vanadium oxides above 550°C, whereby the formation of VO and V_2O_5 mainly leads to enhanced friction behavior. However, it has not clarified which oxides allow the incipient friction drop of the Fe-V-coating at temperatures above 450°C. Nevertheless, the knowledge gained by these experiments is of great interest. In forthcoming studies, different contents of vanadium as well as different metallic matrices such as cobalt based alloys should be investigated. Moreover, the oxidation behavior of thin films containing vanadium in combination with wear resistant CrAlN coatings is also of great interest for future investigations.

Especially, the temperature-induced phase transformation in dependency of the vanadium content, and crystalline structure are of major interest.

Acknowledgement

The authors gratefully acknowledge the financial support of the DFG (German Research Foundation) within the Collaborative Research Centre SFB 708 subproject A1. The contributions of DURUM Verschleissschutz GmbH are gratefully acknowledged for their support in providing the vanadium-containing feedstock material. The authors would like to thank the DELTA machine group for providing synchrotron radiation.

References

1. K. Bobzin, N. Bagcivan, M. Ewering, DC-MSIP/HPPMS (Cr,Al,V)N and (Cr,Al,W)N thin films for high-temperature friction reduction, *Surf. Coat. Technol.*, 2011, **205**, p 2887-2892.
2. H. A. Wriedt, The O-V (Oxygen-Vanadium) System, *Bulletin of Alloy Phase Diagrams*, 1989, **10**(3), p 271-277.
3. D. R. Lide, *CRC handbook of chemistry and physics, A ready-reference book of chemical and physical data*, CRC Press, Boca Raton, 2004
4. R. Franz and C. Mitter, Vanadium containing self-adaptive low-friction hard coatings for high-temperature applications, A review, *Surf. Coat. Technol.*, 2013, **228**, p 1-13.
5. A. P. Hammersley, S. O. Svensson, A. Thompson, Calibration and correction of spatial distortions in 2D detector systems, *Nuclear Instruments and Methods in Physics A*,1994, **346**(1-2), p 312-321.
6. B. Sundman, An assessment of the Fe-O system, *JPE,* 1991*,* **12**(2), p 127–140.
7. C. Leroux, G. Nihoul, G. van Tendeloo, From VO2(B) to VO2(R). Theoretical structures of VO2 polymorphs and in situ electron microscop, *Phys. Rev. B*, 1998, **57**(9), p 5111–5121.
8. J. Cao, E. Ertekin, V. Srinivasan, W. Fan, S. Huang, H. Zheng, Strain engineering and one-dimensional organization of metal-insulator domains in single-crystal vanadium dioxide beams, *Nature nanotechnology*, 2009, **4**(11), p 732–737.
9. L. Bai, Q. Li, S. Corr, Y. Meng, C. Park, S. V. Sinogeikin, Pressure-induced phase transitions and metallization in VO2, *Phys. Rev. B*, 2015, **91**(10), p 1–7.

Investigation of structural flexibility in metal-organic framework thin films by in-situ grazing incidence X-ray diffraction

Suttipong Wannapaiboon,[1,2] Andreas Schneemann,[1] Inke Schwedler,[2] Min Tu,[2] Christian Sternemann,[3] Michael Paulus,[3] Gregor Kieslich,[1] Roland A. Fischer[1,*]

[1] *Chair of Inorganic and Metal-Organic Chemistry, Department of Chemistry, Technical University of Munich, D-85787 Garching, Germany*
[2] *Chair of Inorganic Chemistry II-Organometallics and Materials Chemistry, Faculty of Chemistry and Biochemistry, Ruhr-Universität Bochum, D-44780 Bochum, Germany*
[3] *Faculty of Physics / DELTA, Technical University of Dortmund, D-44221 Dortmund, Germany*

Metal-Organic Frameworks (MOFs), a new class of porous inorganic-organic hybrids, have been studied extensively in the past two decades due to their outstanding porosity, chemical modularity and structural diversity. MOFs are constructed by a building-block principle and the different components can be replaced or modified, thus allowing a high grade of tunability. This versatility makes MOFs promising materials for various applications such as gas separation and storage, and makes them superior over other common porous materials, such as silica or zeolites. A fascinating subclass of MOFs are soft porous crystals, [1] which possess an inherent structural flexibility and can undergo a single-crystal to single crystal transition when exposed to an external stimulus, such as gas adsorption/desorption, temperature or pressure. [2] An example for an interesting material that undergoes this transition is the pillared-layered material $[M_2(fu\text{-}bdc)_2(dabco)]_n$ (M = metal ions such as Zn^{2+}, Co^{2+}, Ni^{2+} and Cu^{2+}; fu-bdc = 2,5-(dialkoxy)benzene-1,4-dicarboxylate; dabco = 1,4-diazabicyclo[2.2.2.]octane). [3]

The integration of functionalized MOFs in micro systems and devices requires the deposition of MOF thin films on substrates. These composite materials offer high potential in assorted applications, such as chemical sensors, separation membranes and capillary columns for gas chromatography. [4] The stepwise liquid phase epitaxy method (LPE) is one of the potential methods to achieve MOF thin films of well-defined layer thickness or crystallite size with controlled crystallographic orientation leading to so-called surface-mounted metal-organic frameworks (SURMOFs). [5]

Herein, we fabricated the Cu-based pillared-layered SURMOFs, $[Cu_2(fu\text{-}bdc)_2(dabco)]_n$, by LPE process. The structural flexibility of the fabricated SURMOFs upon adsorption and desorption of methanol vapor was monitored by in-situ grazing incidence x-ray diffraction (GIXRD), collected at Beamline BL09 at DELTA Synchrotron, Germany (X-ray energy of 15 keV or wavelength 0.828 Å, refined sample-to-detector distance of 599 mm and the incidence angle of 0.6°). The activation of SURMOF by He purging partly changes the MOF structure from the large-pore phase to the narrow-pore phase (approximately 50%), Figure 1 (red curves). The loading of methanol for at least 20 % P/P_0 into the activated SURMOF is required in order to change the structure from the narrow-pore phase back to the large-pore phase, Figure 1 (orange curves). This structural flexibility is reversible upon adsorption and desorption of methanol vapor from the MOF pores as schematically illustrated in Figure 2. Further investigation is required to get insight into the structural-flexible phenomena of this MOF anchored to the substrate surface.

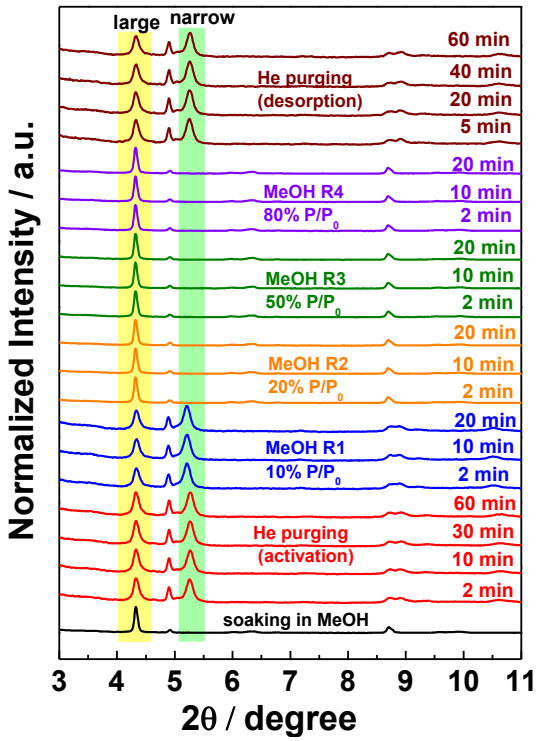

Figure 1 (a) In-situ monitoring of GIXRD (Out-of-plane cuts) of the $[Cu_2(fu\text{-}bdc)_2(dabco)]_n$ SURMOF upon adsorption and desorption of methanol vapor at 25 ℃

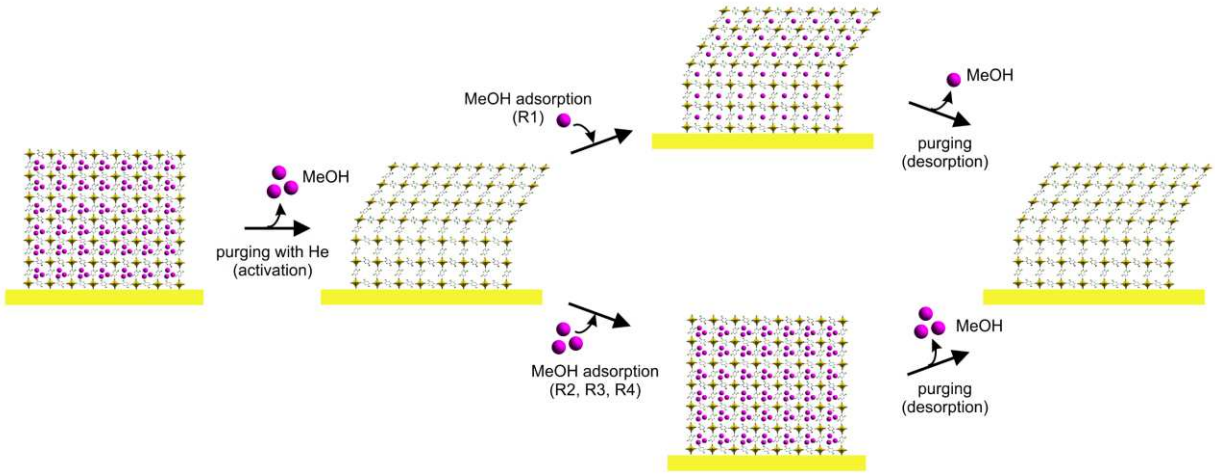

Figure 2 Schematic illustration of structural flexibility upon adsorption and desorption of methanol vapor into the SURMOFs

References

[1] S. Horike, S. Shimomura, S. Kitagawa, *Nat. Chem.* **2009**, *1*, 695.

[2] A. Schneemann, V. Bon, I. Schwedler, I. Senkovska, S. Kaskel, R. A. Fischer, *Chem. Soc. Rev.* **2014**, *43*, 6062.

[3] A. Schneemann, S. Henke, I. Schwedler, F. Wieland, C. Sternemann, M. Paulus, R. A. Fischer, *manuscript in preparation*

[4] O. Shekhah, J. Liu, R. A. Fischer, C. Woell, *Chem. Soc. Rev.* **2011**, *40*, 1081.

[5] L. Heinke, M. Tu, S. Wannapaiboon, R. A. Fischer, C. Woell, *Microporous and Mesoporous Mater.* **2015**, *216*, 200.

Supramolecular structure of monohydroxy alcohols at high pressure

Thomas Büning, Christian Sternemann, Catalin Gainaru, Michael Paulus, Holger Göhring, Susanne Dogan, Julian Schulze, Roland Böhmer and Metin Tolan

Fakultät Physik/DELTA, Technische Universität Dortmund, 44221 Dortmund, Germany

Hydrogen bonds are essential for the structure and dynamics of alcohols, aqueous solutions and water. Monohydroxy alcohols (MAs) have been studied as a model system for hydrogen bonded fluids in general for decades [1]. Due to the interplay of hydrogen bonding and steric hindrance, they are supposed to form supramolecular structures such as chains and rings in the liquid phase. These supramolecular clusters cause an absorption band in the mHz to GHz regime, referred to as Debye process, which distinguishes MAs and water from most other liquids. 2-ethyl-1-hexanol (2E1H) has been investigated intensively over a wide range of temperature and pressure. Especially, a nonlinear temperature evolution with a change of slope at 250 K of the strength of the Debye process has been a surprising result [2]. Moreover, an oppositional pressure dependence compared to the ring building MA 4-methyl-3-heptanol (4M3H) has been found [3]. The origin of these phenomena calls for an explanation on molecular level. X-ray diffraction (XRD) is a valuable tool to obtain information about typical length scales in liquids. XRD patterns of 2E1H and 4M3H were measured employing the setup for high pressure small- and wide-angle x-ray scattering at BL9 [4]. The measurements were performed at temperatures of 276 K, 300 K, and 343 K. The pressure was increased in steps of 500 bar until the maximum pressure of 4500 bar was reached. In some cases the Kapton window of the sample holder broke; those XRD patterns were not taken into account. The incident photon energy was 24 keV, which allowed the beam penetrate through the diamond windows of the high-pressure cell. Figure 1 shows the diffraction patterns of 4M3H and 2E1H at 276 K and 343 K. They consist of two peaks in the medium wave vector transfer (q) range, which is typical for an alcohol [5]. The main diffraction peak is mainly due to the carbon-carbon correlations in the liquid. It features a less intense prepeak at smaller q-values. This prepeak caused by supramolecular arrangements and its position displays a typical distance between the oxygen skeletons of the supramolecular clusters separated by the carbon chains of the molecules [5, 6]. As depicted from figure 1, both peaks shift to higher q-values at increasing pressure, which is due to the increased density (a detailed discussion of the peak parameters is presented in reference [7]). The combined shift of both peaks is in line with the compressibility for 2E1H [8]. Furthermore, the prepeak intensity decreases with increasing pressure in both alcohols at all temperatures. This might indicate a reduced number of supramolecular arrangements in the liquid [9]. Interestingly, the width of the prepeak σ_{pp} develops in oppositional directions in 2E1H and 4M3H at temperatures of 276 K and 300 K, as presented in figure

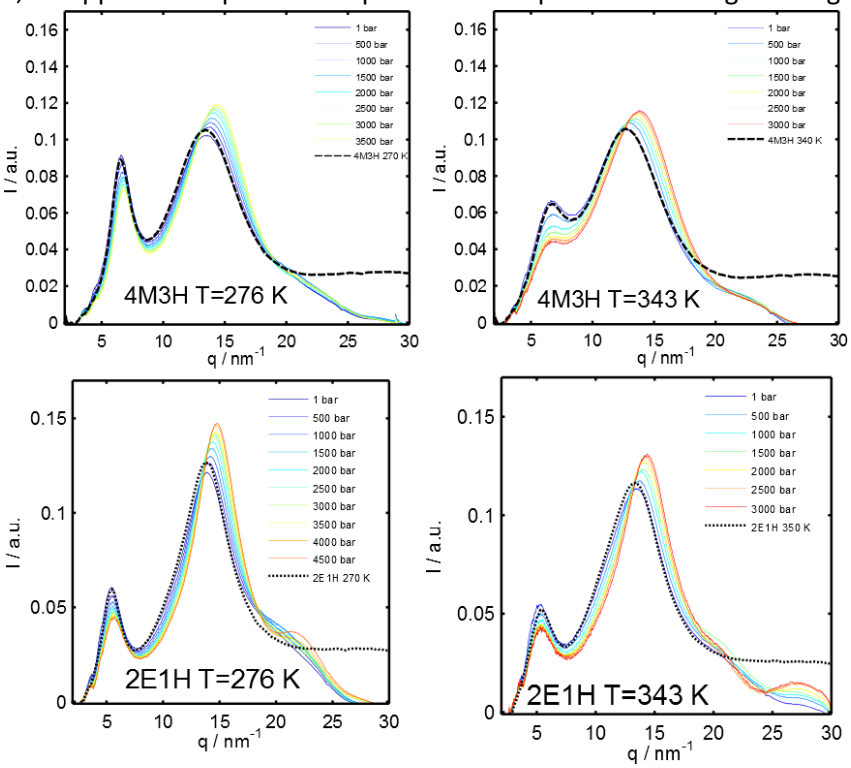

Figure 1: XRD patterns of 4M3H and 2E1H at temperatures of 276 K and 343 K over a wide range of pressure.

2. The values of σ_{pp} are approaching each other with increasing pressure. The prepeak width σ_{pp} correlates with the degree of local order in the molecule distribution [10]. It differs significantly at ambient conditions and is similar at high pressures. This suggests that the supramolecular structures are more alike at high pressures, which is in line with dynamic measurements that have suggested a disintegration of supramolecular arrangements [3]. In 2E1H a shortening of supramolecular chains and in 4M3H a transformation of ring like clusters into chainlike ring fragments has been proposed [3]. Such a transition is sketched in figure 2 b). It has to be mentioned that temperature has a major influence on the XRD patterns. Increasing the temperature leads to a decrease of the prepeak intensity. Therefore, it can be concluded that increasing the temperature leads to a disintegration of supramolecular structures and an increasing amount of monomers in the liquid. At the highest temperature of 343 K σ_{pp} differs significantly in 2E1H and 4M3H. In both liquids the prepeaks become wider with increasing pressures, which is due to the increasing number of monomers in both liquids.
The structures are strongly disturbed by temperature in 4M3H; probed via an increasing width and a decreasing intensity of the prepeak. At a temperature of 343 K the amount of supramolecular structure is strongly reduced and a further disturbance can be observed. The temperature dependence is less pronounced in 2E1H; the same temperature behavior was observed in 2E1H in previous measurements.
In a nutshell, the XRD patterns support the structure model that has been proposed on the basis of dielectric measurements. Further insights could be gained by comparing these data with results from molecular dynamic simulations. Additionally, investigations employing diamond anvil cells at BL9 will allow to access a wider range of pressure and temperature in the near future.

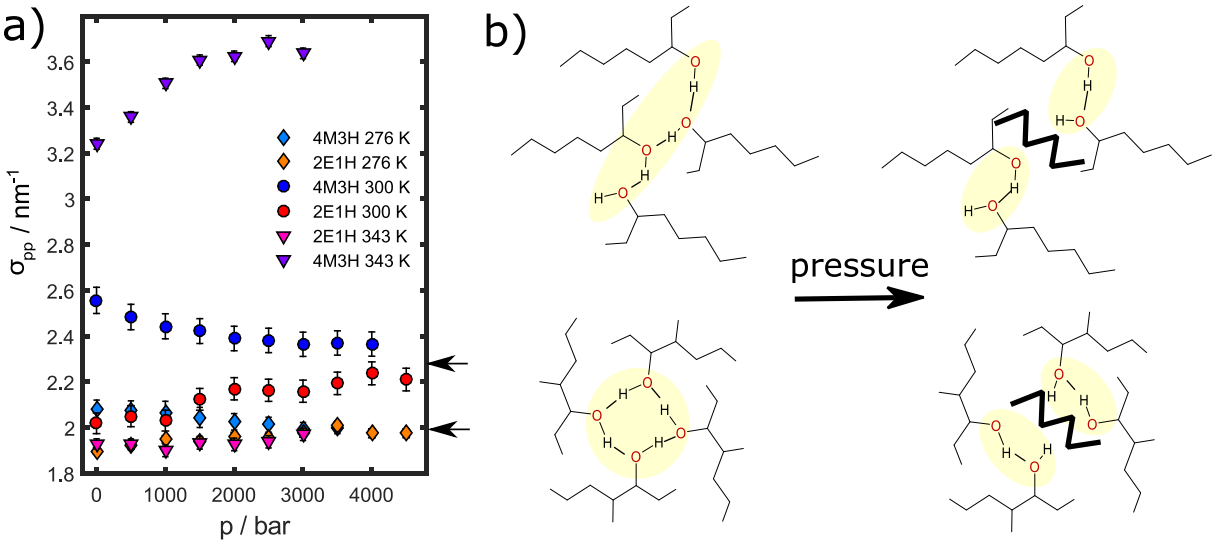

Figure 2: a) σ_{pp} of 2E1H and 4M3H at temperatures of 276 K, 300 K and 343 K at increasing pressures up to 4500 bar, b) sketch of the structural rearrangements at high pressure in 2E1H and 4M3H.

References: [1] R. Böhmer, C. Gainaru, and R. Richert, Phys. Reports **545**, 125-195 (2014) and references therein; [2] C. Gainaru, S. Kastner, F. Mayr, P. Lunkenheimer, S. Schildmann, H. J. Weber, R. Böhmer et al. Physical Review Letters, **107**, 118304 (2011); [3] S. Pawlus, M. Wikarek, C. Gainaru, M. Paluch, and R. Böhmer, The Journal of Chemical Physics **139**, 064501 (2013); [4] C. Krywka, C. Sternemann, M. Paulus, N Javid, R. Winter, A. Al-Sawalmih, S. Yi, D. Raabe, and M. Tolan, Journal of Synchrotron Radiation, **14,** 244251 (2007). [5] M. Tomšič, A. Jamnik, G. Fritz-Popovski, O. Glatter, and L. Vlček, The Journal of Physical Chemistry B **111** 1738-1751 (2007); [6] S. P. Bierwirth, T. Büning, C. Gainaru, C. Sternemann, M. Tolan, and R. Böhmer, Physical Review E **90**, 052807 (2014). [7] T. Büning, Dissertation, TU Dortmund (2016). [8] A. Reiser, G. Kasper, C. Gainaru, and R. Böhmer, The Journal of Chemical Physics **132**, 181101 (2010). [9] A. Hédoux, Y. Guinet, L. Paccou, P. Derollez, and F. Danède, The Journal of Chemical Physics **138**, 214506 (2013). [10] I. M. Shmyt'ko, R. J. Jiménez-Riobóo, M. Hassaine, and M. A. Ramos, Journal of Physics: Condensed Matter **22**, 195102 (2010).

Acknowledgement: We would like to thank the DELTA machine group for providing synchrotron radiation and technical support. Support of this project by the Deutsche Forschungsgemeinschaft (DFG) under Grant No. BO1301/8-2 is gratefully acknowledged. Thomas Büning thanks the BMBF (Project 05K13PE2 within FSP-302) and MERCUR (AN-2014-0036) for financial support, and we acknowledge the support by the cluster of excellence RESOLV funded by the DFG

Temperature dependent powder diffraction studies on coordination polymers with acetylenedicarboxylate as linker

V. K. Gramm, M. Werker and U. Ruschewitz*

Department für Chemie, Universität zu Köln, 50939 Köln, Germany

**email: uwe.ruschewitz@uni-koeln.de*

From high-resolution synchrotron powder diffraction data recorded at BL9 we were able to refine the crystal structures of the trivalent rare earth acetylenedicarboxylates $[RE_2(ADC)_3(H_2O)_6]\cdot 2H_2O$ with RE = Yttrium, Holmium, Erbium crystallizing in an already known structure type [1]. As these structures crystallize in the triclinic space group $P\bar{1}$, the diffraction patterns show a large number of reflections, as illustrated in figure 1 for $[Y_2(ADC)_3(H_2O)_6]\cdot 2H_2O$. For the *Rietveld* refinement of the data, the program GSAS [2] was used. Due to 18 crystallographically independent atoms in the unit cell, the number of refined parameters is quite large so that soft constraints/restraints had to be used for a stable refinement. Therefore a large number of reflections with well defined intensities are needed. The data recorded at BL9/DELTA meet these requirements. The samples were measured in capillaries, sealed in advance in our labs in Cologne. As expected for rare earth cations, the volume of the three refined compounds decreases with increasing atomic numbers and fits very well to the other unit cell volumes of the known compounds of this structure type.

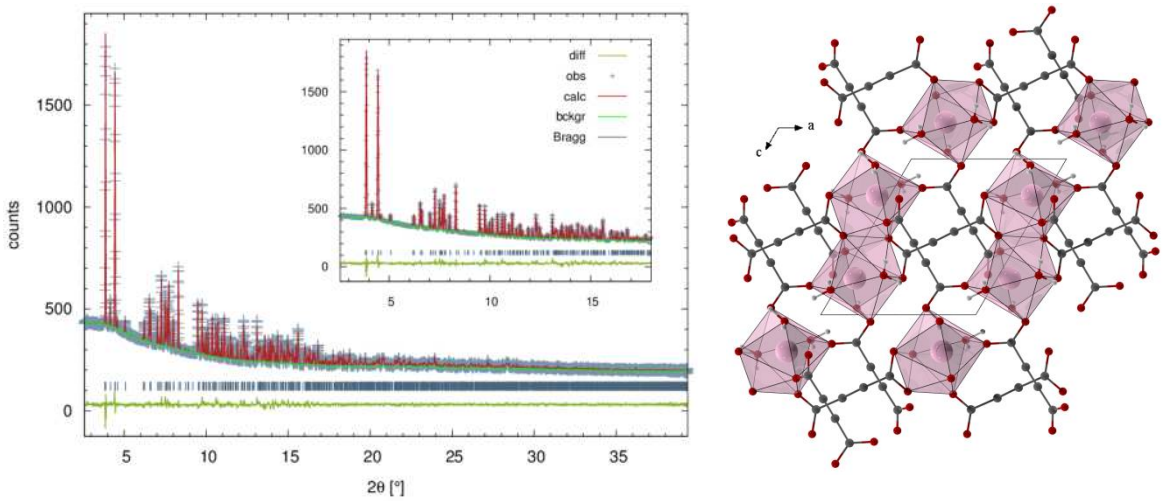

Figure 1: *Rietveld* plot, refined with GSAS [2] (left) and view of the crystal structure of $[Y_2(ADC)_3(H_2O)_6]\cdot 2H_2O$ along [010] (right).

The thermal expansion of the anhydrous acetylenedicarboxylates $Cs_2(ADC)$ and Eu(ADC) was investigated at BL9 by means of temperature-dependent powder diffraction below room temperature. Again, these samples were sealed in capillaries in advance in our labs in Cologne. Starting at room temperature, the samples were cooled down with a defined

temperature program using the Cryostreamer Cryojet-700-Compact (Oxford Cryosystems) provided by DELTA. At each defined temperature a powder pattern of the sample was recorded. The subsequent warming up to room temperature was also controlled with the cryostreamer.

The evaluation of the recorded data was performed with Jana2006 [3a] using *Le Bail* Fits [3b]. As expected due to our former investigations, Cs_2(ADC) shows a positive thermal expansion below room temperature (see figure 2, right). For Eu(ADC) we found a negative thermal expansion below room temperature, comparable to that reported for Sr(ADC) [4].

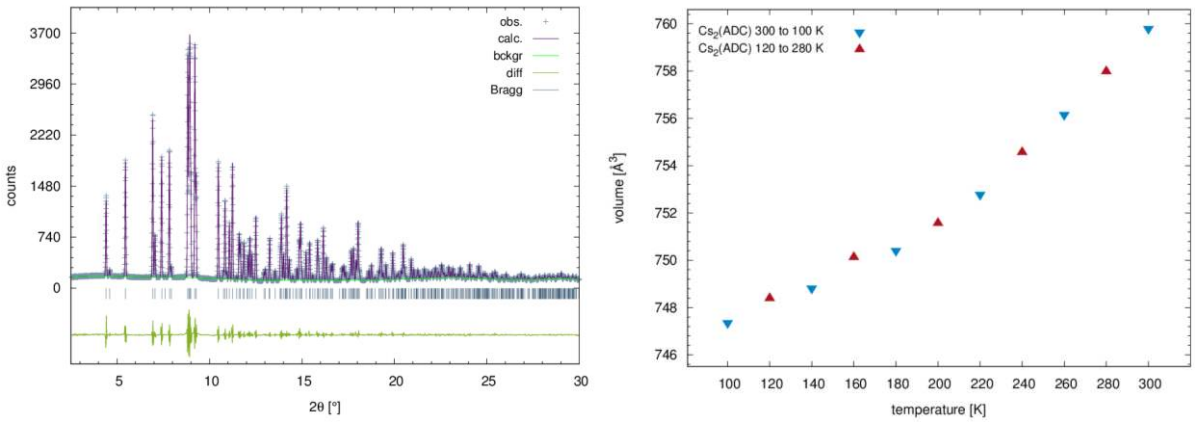

Figure 2: Exemplary *Le Bail* Fit of Cs_2(ADC), recorded at 250 K (left) and thermal expansion of Cs_2(ADC) between 100 and 300 K (right).

Furthermore the thermal behavior of the anhydrous acetylenedicarboxylate Pb(ADC) was investigated below room temperature. In line with our investigations by low temperature differential scanning calorimetry (LT-DSC) we expected a phase transition at about 250 K. But in the temperature-dependent powder diffraction patterns only a distinct broadening of the reflections and simultaneous amorphization was observed. All attempts to solve the crystal structure of this amorphous phase failed so far.

For all experiments described in the report the detector *Pilatus100K* was used.

References

[1] A. Michaelides, S. Skoulika, *Crys. Growth Des.* **2005**, *5*, 529.

[2] H. M. Rietveld, *Acta Crystallogr.* **1967**, *22*, 151; B. H. Toby, *J. Appl. Crystallogr.* **2001**, *34*, 210.

[3] a) V. Petricek, M. Dusek, L. Palatinus, *Z. Kristallogr.* **2014**, *229*, 345; b) A. LeBail, *Powder Diffraction* **2005**, *20*, 316.

[4] F. Hohn, I. Pantenburg, U. Ruschewitz, *Chem. Eur. J.* **2002**, *8*, 4536.

Direct monitoring of polymer recrystallization

L. Grodd[1], E. Mikayelyan[1], U. Pietsch[1], F. Spieckermann[2], H. Zhang[2], G. Reiter[2], S. Grigorian[1]

[1] Department of Physics, University of Siegen

[2] Physikalisches Institut, Albert-Ludwigs-Universität, Freiburg

Due to their electric properties, mechanical flexibility and easy solution based processibility there are various applications for conjugated polymers in organic electronics. The mobility of the charge carriers, which is a key parameter for the performance of electronic devices, is strongly influenced by the orientation of the crystals in the typically semicrystalline polymer films.

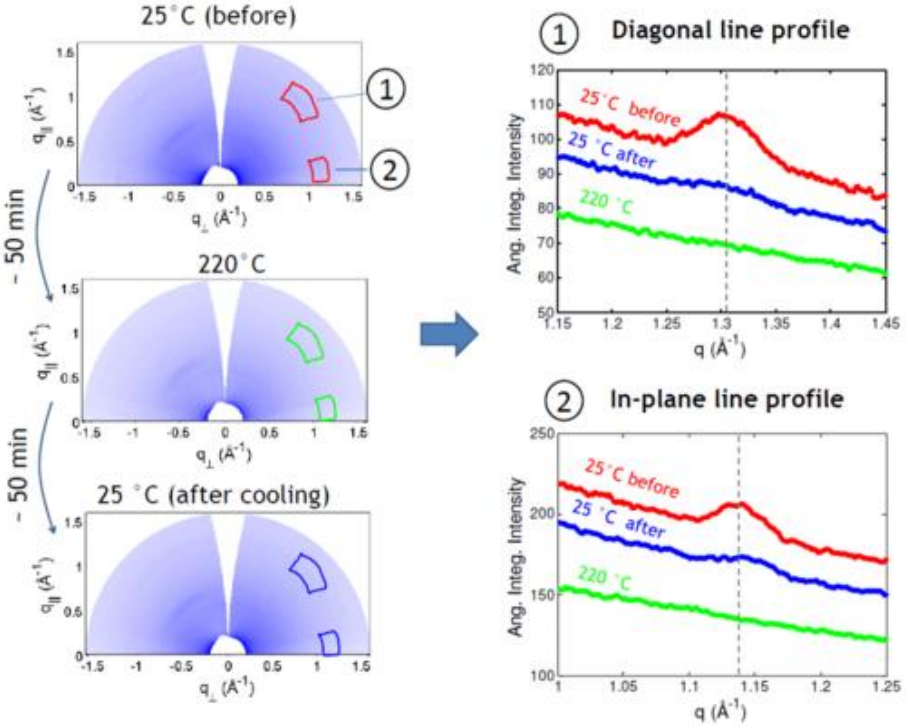

Figure 2: 2D diffraction patterns of iPS during the recrystallization experiment (left) and radial line profiles (right) of the highlighted areas at initial room temperature, at 220 °C and after cooling back to room temperature.

Therefore, gaining information about the mechanisms of the growth process will be valuable in order to control it. [1,2] Grazing incidence X-ray diffraction experiments during the crystal growth provides valuable information about a timescale and an evolution of the structural features.

The authors acknowledge the BMBF (project number: 05K13PS4) for the financial support.

References:

[1] Rahimi K., Botiz I., Stingelin N., Kayunkid N., Sommer M., Koch F.P., Nguyen H., Coulembier O., Dubois P., Brinkmann M., Reiter G., Angew. Chem. Int. Ed. Engl. 2012 ; 51(44), 11131-11135

[2] Xu J., Ma Y., Hu W., Rehahn M. and Reiter G., Nature Materials 2009, 8, 348-353

Role of alkyl chain substituent on self-assembly properties of donor-acceptor polymers.

Tomasz Marszalek,[1, 2] Wojciech Zajaczkowski,[2] Felix Hinkel,[1,2], Yu Yamashita,[3] H. Matsui,[3] J. Takeya,[3] Klaus Müllen,[2] Wojciech Pisula[2,4,*]

[1] Organisch-Chemisches, Inzstitut Ruprecht-Karls-Universitat Heidelberg, Im Neuenheimer Feld 270, 69120 Heidelberg (Germany)
[2] Max Planck Institute for Polymer Research, Ackermannweg 10, 55128 Mainz (Germany)
[3] Department of Advanced Materials Science, The University of Tokyo, 5-1-5 Kashiwanoha, Kashiwa 277-8561, Chiba (Japan)
[4] Department of Molecular Physics, Faculty of Chemistry Lodz University of Technology, Zeromskiego 116, 90-924 Lodz (Poland)
* Email: pisula@mpip-mainz.mpg.de

In contrast to our previous studies[1] where the influece of geometry and substitution position of alkyls side chains on self-assambly properities has been investigated, role of alkyl chain substituent length on self-assambly porperities of donor-acceptor CDT-BTZ polymers has been performed. For this purpose, two different substituents, hexadecyl (C16, P1) and eicosyl (C20, P2) in CDT-BTZ structure (Figure 1) have been synthesized and coorelation beetwen backbone alignment on molecular organization and its impact on charge transport characteristics in field-effect transistors has been discused. These results have been recently published in Chemistry of Materials.[2]

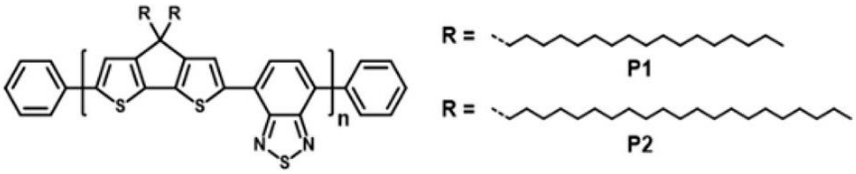

Figure 1. Chemical structure of CDT-BTZ polymers P1 and P2

To investigate the impact of the alkyl chain length on the molecular packing structure of CDT-BTZ thin films, GIWAXS measurements was performed. The improvement of ordering in thin films was confirmed by the increase in interlayer coherence length represented by the corresponding full width at halfmaximum (FWHM) parameters. To understand better the relation between alkyl substituents and supramolecular organization, two types of samples were prepared based on drop-casting and compression. First, the influence of the alkyl chains length (C16 or C20) in drop-cast films was investigated. GIWAXS patterns in Figure 2 a,b for drop-cast films indicate little difference in ordering between P1 and P2. Both polymers revealed an edge-on and face-on mixture in the surface arrangement. In the case of P2, the interlayer and π-stacking reflections were detected on the out-of-plane pattern and correspond to d-spacings of 2.82 and 0.35 nm. The same organization was found for P1 with interlayer and π-stacking spacings of 2.52 and 0.35 nm. The minor variation in the interlayer distance between P1 and P2 was related to the different side chain length. Therefore, it could be assumed that the alkane interdigitation is basically identical for both polymers not affecting the π-stacking. Moreover, the out-of-plane interlayer coherence length remained unchanged for both polymers. Coherence lengths of 13.6 nm for P1 and 17.0 nm for P2 were determined corresponding in each case to six layers. The same interlayer coherence length corresponding to 6 layers was found for the films obtained by compressing (Figure 2 c,d). On the basis of the described results, it could be

concluded that the interlayer and π-stacking distances and coherence lengths for both CDT-BTZ polymer derivatives were not dependent on the film deposition method.

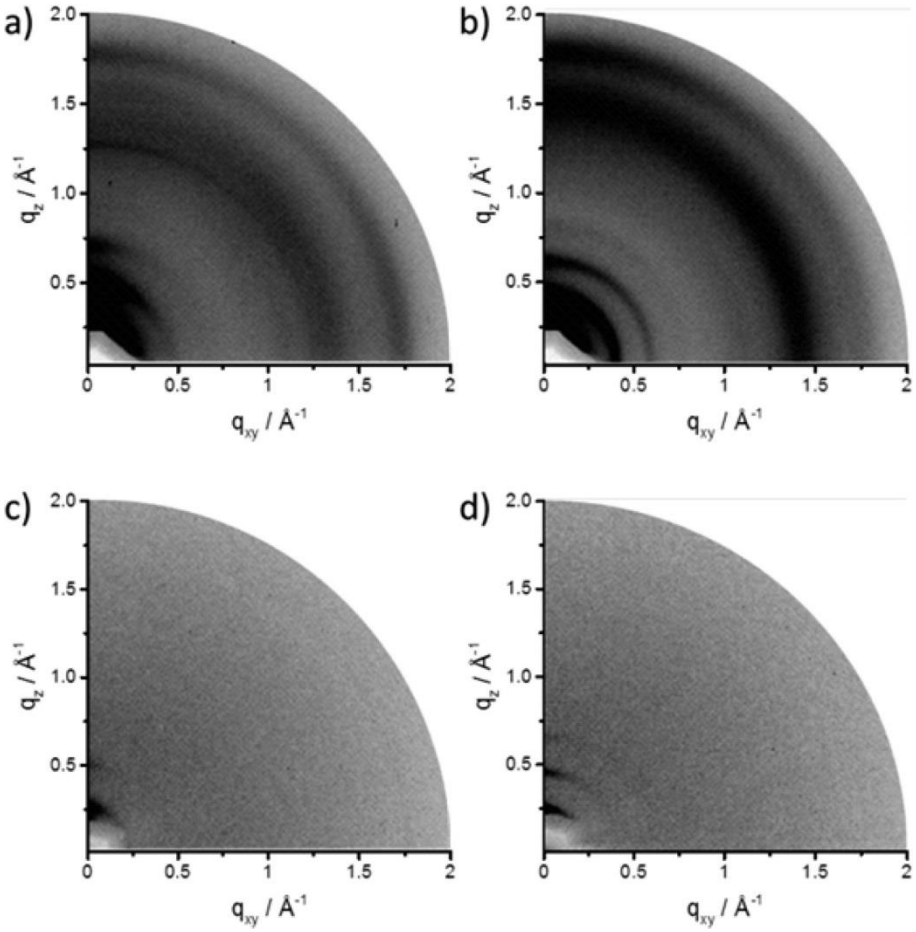

Figure 2. Grazing incidence wide-angle X-ray scattering (GIWAXS) patterns of (a) P1 and (b) P2 drop-cast films. GIWAXS patterns of (c) P1 and (d) P2 compressed films.

1. F. Hinkel, T. Marszalek, W. Zajaczkowski, S. R. Puniredd, M. Baumgarten, W. Pisula and K. Müllen, *Chemistry of Materials*, 2014, **26**, 4844-4848.
2. Y. Yamashita, F. Hinkel, T. Marszalek, W. Zajaczkowski, W. Pisula, M. Baumgarten, H. Matsui, K. Müllen and J. Takeya, *Chemistry of Materials*, 2016, **28**, 420-424.

"Polymer films morphology on the different flexible substrates"

Kateryna Shchyrba[1], Ullrich Pietsch[1], Souren Grigorian[1]

[1] Department of Physics, Faculty of Science and Technology, University of Siegen, Germany

One of the important research directions in Organic Electronics, called Stretchable/Flexible Electronics, has attracted a lot of attention: possibility to create cheaper, lighter, more mechanically stable, fully organic, chemically/ biologically compatible electronics shows huge potential along with numerous practical applications in different fields and daily life. As an active layer one can use various combinations of polymer compounds and one of such special class of solution-processible regioregular polythiophenes- P3HT provide nice film formed structure with self-organised microcrystalline domains, created by interchain stacking of 2D sheet-like lamella, formed by assembly of polymer backbones and thiophene rings and particularly interesting for us , due to its semiconducting properties.[1] [2] [3] Another usage of chemical organic compounds can be found in solar cell technology: one of the example of polymer:fullurene solar cells- poly[4,8-bis[(2-ethylhexyl)oxy]benzo[1,2-:4,5-b′]-dithiophene-2,6-diyl][3-fluoro-2-[(2-ethylhexyl)carbonyl]-thieno[3,4-b]-thiophenediyl] (PTB7). This active novel donor material consists of bulk heterojunction films, created by conjugated polymers and fullerene derivatives and provide low bandgap light absorption, high power conversion efficiency (PCE), appropriate energy level positions and quite high carrier mobilities. [4] [5] [6] It was shown, that different types of material can be used as candidates for flexible substrates, such as: kapton, polyethylene, paper, polyimide, textiles, fibers, PDMS, Si-elastomers, etc. We have chosen in our research for flexible substrates textiles, PDMS and Si-elastomers, as for the conjugated polymers, we have used 2 main materials, used in Organic Electronics- P3HT (regioregular poly(3-hexylthiophen)) and PTB7. Naturally, in such comparably new field, there are a lot of unsolved problems and open questions, so in our discovery, we have decided to focus on behaviour of polymer film on top of the flexible substrate and mechanical stability of such objects, via applying external force. To provide stretching movement, we have created at the University of Siegen special motorized stage. Structural investigations we have conducted at BL9, DELTA, using the grazing incidence X-ray diffraction method (GIXD) for in-situ X-ray structural investigations of different stretchable substrates coated with polymer films. On the picture below we can see comparison of polymer P3HT peaks coated on several substrates:

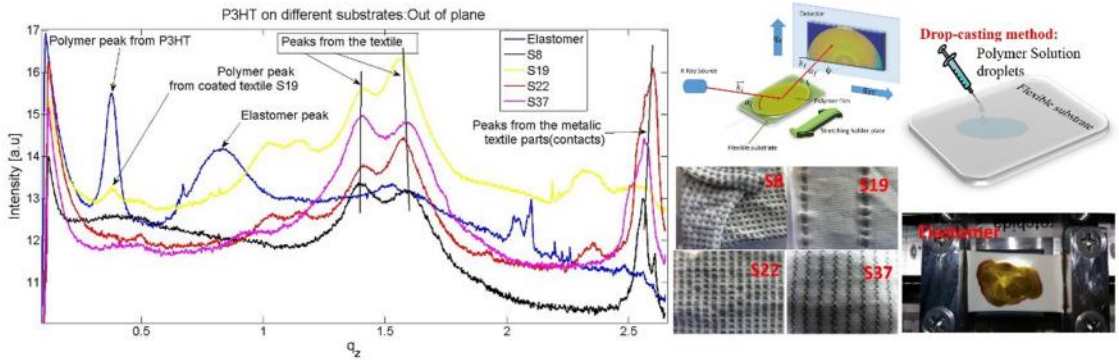

Fig.1. Out of plane profile for P3HT without alongation for 2 substrate materials: textiles with different waving structure and Elastomer. On the picture also presented picture of clean substares, schematic description of in-situ measurements during stretsching and coating method we used.

After several experimental trials with different substrates, we have stopped on PDMS with thickness 0.7-0.8mm. We present comparison of internal microcrystalline structure in our polymer film, formed by 2 main polymers on top of the same substrate type. On the picture below, one can see a notice in peaks shape for P3HT and PTB7 respectively depending on elongation level:

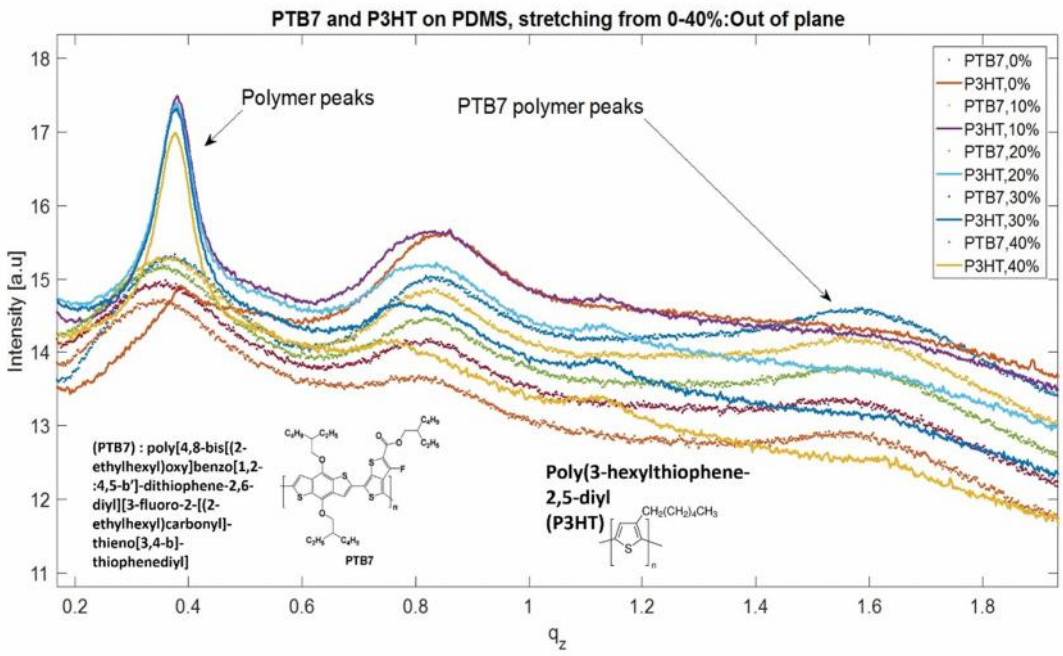

Fig.2. P3HT and PTB7 polymer films under external force applied: out of plane profiles during stretching, elongation in % from initial sample length.

The interplanar distances during a stretching process for both polymer types show distinctive modification in initial arrangement of microcrystalline domains. The substrate movement imply a strong effect on lamellar film structure followed by the additional surface effects and creating cracks for the higher strains.

The authors acknowledge the support of the DAAD through the PROCOPE program (project No 57211900) for the financial support.

References:

[1] H. Sirringhaus *et al.*, "Two-dimensional charge transport in self-organized, high-mobility conjugated polymers," *Nature*, vol. 401, no. 6754, pp. 685–688, Oct. 1999.

[2] I. McCulloch *et al.*, "Liquid-crystalline semiconducting polymers with high charge-carrier mobility," *Nat. Mater.*, vol. 5, no. 4, pp. 328–333, Apr. 2006.

[3] B. S. Ong, Y. Wu, P. Liu, and S. Gardner, "High-Performance Semiconducting Polythiophenes for Organic Thin-Film Transistors," *J. Am. Chem. Soc.*, vol. 126, no. 11, pp. 3378–3379, Mar. 2004.

[4] S. Nam *et al.*, "All-Polymer Solar Cells with Bulk Heterojunction Films Containing Electron-Accepting Triple Bond-Conjugated Perylene Diimide Polymer," *ACS Sustain. Chem. Eng.*, vol. 4, no. 3, pp. 767–774, Mar. 2016.

[5] Y. Liu *et al.*, "Aggregation and morphology control enables multiple cases of high-efficiency polymer solar cells," *Nat. Commun.*, vol. 5, p. 5293, Nov. 2014.

[6] I. Etxebarria, A. Guerrero, J. Albero, G. Garcia-Belmonte, E. Palomares, and R. Pacios, "Inverted vs standard PTB7:PC70BM organic photovoltaic devices. The benefit of highly selective and extracting contacts in device performance," *Org. Electron.*, vol. 15, no. 11, pp. 2756–2762, Nov. 2014.

Compressibilities of solid-supported DMPC membranes containing cholesterol at high hydrostatic pressure

Göran Surmeier, Michael Paulus, Christian Sternemann, Susanne Dogan, Lukas Tepper, Steffen Bieder, Julian Schulze, Julia Nase, and Metin Tolan

Fakultät Physik/DELTA, TU Dortmund, 44221 Dortmund, Germany

Email: goeran.surmeier@tu-dortmund.de

A lipid bilayer is the basic component of cell membranes, which separate the intracellular and extracellular region and regulates the mass transfer between both regions in all living organisms. We use solid-supported DMPC (1,2-dimyristoyl-*sn*-glycero-3-phosphocholine) bi- and multilayers with different concentrations of cholesterol as model membranes to examine the pressure-dependent behavior of those structures by x-ray reflectivity measurements.

In a former experiment we investigated the phase behavior of solid-supported multilayers of pure DMPC at high hydrostatic pressure using the same methods. We were able to determine phase boundaries between the liquid phase und different gel phases and, moreover, observed specific effects like a pressure-induced multilayer formation and a pressure-dependent filling of the water layers between the separate lipid bilayers in a multilayer system [1]. By adding cholesterol to the investigated lipid layers, we went one step forward to a more biologically relevant structure, as in nature, membranes are highly complex systems that are interstratified by cholesterol and proteins.

In order to obtain information about the vertical arrangement of solid-supported DMPC membranes with cholesterol, we conducted high energy x-ray reflectivity measurements at the solid-liquid interface between silicon and an aqueous buffer solution at beamline BL9 at DELTA. These measurements were performed in a custom-made high hydrostatic pressure cell [2] and at a photon energy of 27 keV. The beam size was 0.1 mm (vertical) × 1 mm (horizontal). Pressures up to 4 kbar and a temperature of 20 °C were applied. Our samples were prepared on silicon wafers by a spin coating process. For this purpose, 2 mg DMPC and different amounts of cholesterol up to 28 mol% were dissolved in 2 ml 2-propanol.

The measurements that were taken at DELTA are a completion of a data set that were obtained at ID31 at the ESRF (European Synchrotron Radiation Facility). On the basis of this data set, we observed that at 20 °C, the lipid layers are in a gel phase and show an approximately linear change of their thickness with increasing pressure, so that it is possible to describe their behavior by a linear compressibility. Moreover, we found a fundamental difference between the compressibilities of bi- and multilayers. The compressibility monotonically decreased with increasing amount of cholesterol undergoing a change of sign at about 25 mol% in the bilayer case, while it was non-monotonic and permanently negative in the multilayer case. At DELTA we successfully reproduced the corresponding measurements and were able to confirm the results, as is shown in figure 2.

Figure 1 shows some of the reflectivity curves. The data of a pure DMPC bilayer and a multilayer containing a high amount of cholesterol, each at 50 and 4000 bar, are depicted. As one can see, the oscillation period of the bilayer reflectivity increases with increasing pressure, meaning that the bilayer thickness decreases and the corresponding compressibility is positive. However, the position of the multilayer Bragg peaks shifts to smaller values as the pressure increases, meaning that the layer thickness increases and the compressibility is negative.

Acknowledgments: This work is supported by the Forschergruppe 1979 (**DFG-FOR1979**) and Cluster of Excellence RESOLV (**EXC 1069**) founded by the DFG.

References

[1] B. Nowak, M. Paulus, J. Nase, P. Salmen, P. Degen, F.J. Wirkert, V. Honkimaki, and M. Tolan, *Solid supported lipid multilayers under high hydrostatic pressure,* Langmuir 32, 11 (2016).

[2] F.J. Wirkert, M. Paulus, J. Nase, J. Möller, S. Kujawski, C. Sternemann, and M. Tolan, *X-ray reflectivity measurements of liquid/solid interfaces under high hydrostatic pressure,* Journal of Synchrotron Radiation 21, 76 (2014).

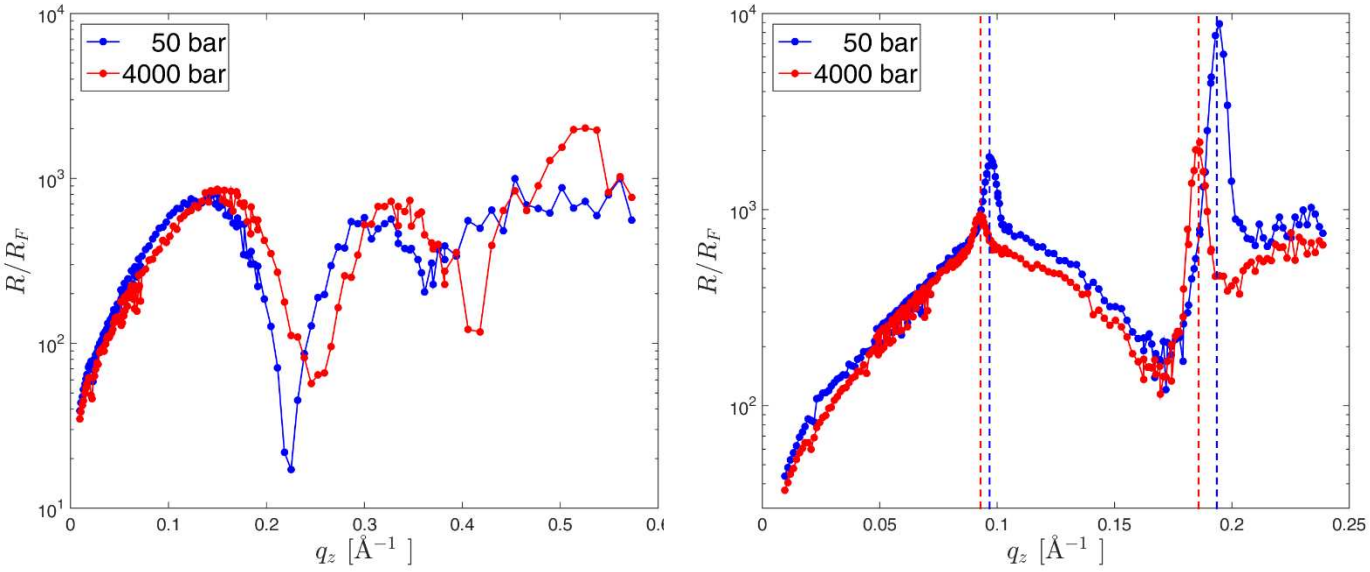

Fig. 1: *Left:* Bilayer reflectivity data of pure DMPC. *Right:* Reflectivity data of DMPC multilayers containing 28 mol% cholesterol.

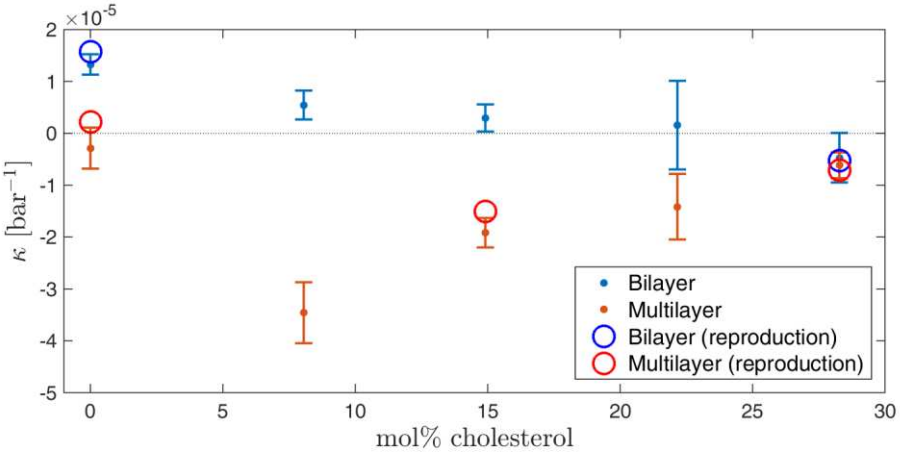

Fig. 2: Compressibilities of DMPC bi- and multilayers containing different concentrations of cholesterol. The results of a former experiment conducted at the ESRF in comparison with the values obtained at DELTA.

Supramolecular Assembly of π-Systems by Conjugation with Oligoproline

Wojciech Zajaczkowski,[1] Tomasz Marszalek,[1,4] Urszula Lewandowska,[2] Helma Wennemers,[2] Klaus Müllen,[1] Wojciech Pisula[1,3,*]

[1] Max Planck Institute for Polymer Research, Ackermannweg 10, 55128 Mainz, Germany
[2] Laboratory of Organic Chemistry, ETH Zurich, Vladimir-Prelog-Weg 3, 8093 Zurich (Switzerland)
[3] Department of Molecular Physics, Faculty of Chemistry Lodz University of Technology, Zeromskiego 116, 90-924 Lodz (Poland)
[4] Organisch-Chemisches, Institut Ruprecht-Karls-Universitat Heidelberg, Im Neuenheimer Feld 270, 69120 Heidelberg (Germany)
* Email: pisula@mpip-mainz.mpg.de

During our beamtime at the beamline 9 of the DELTA electron storage ring in Dortmund in December 2015 we continued our studies on the effect of structural modifications on the self-assembly of oligoprolines conjugated with sterically demanding chromophores (alkynylated perylene monoimides - PMI) (Figure 1). Our results demonstrated that the conjugates beetwen building blocks that do not tendency to self-assemble by their own but govern the spatial orientation between π-systems allows for direct control self-assembly properiteis. However small changes in the length of the peptide backbone have strong influence on the supramolecular assembly of oligoproline-PMI conjugates, forming self-assemblies from worm-like threads via fibrils to nanosheets structures. These results have been recently published in Angew Chem Int Edit[1] and Chemistry - A European Journal[2].

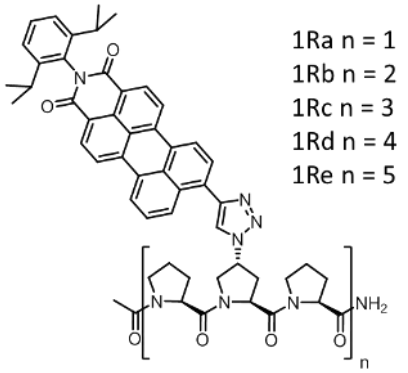

Figure 1. General structure of oligoproline-PMI conjugates.

To understand the relation between the oligoproline length and the supramolecular order grazing incidence wide-angle X-ray scattering (GIWAXS) was used for 1Ra–1Re deposited from mixtures of THF and H_2O (30:70) on Si/SiO_2 substrates. The GIWAXS patterns (Figure 2) indicate an similar supramolecular organization for the whole series, but significant differences in long-range ordering. As previously reported,[1] the π-stacking distance between intercalated PMI units is determined from wide-angle reflections, mostly located on equatorial plane of the pattern, and slightly varies between the oligoprolines. The distance is 3.70 Å for **1Ra** and **1Rd**, whereby the corresponding scattering peak is sharper, but rather isotropic for the first oligoproline (Figure 2). This is characteristic for a higher crystallinity between PMI units, but lack of orientational order of the crystallites towards the surface as in the case of 1Rd.

Interestingly, 1Rb and 1Rc reveal a tighter packing with values of 3.40 Å and 3.60 Å, respectively (Figure 2a-b). An additional equatorial wide-angle reflection for both derivatives suggest a tilting or shifting of the PMI units towards each other which is missing for 1Ra and 1Rd. In contrast, the longest oligoproline 1Re shows no π-stacking due to high disorder in the PMI packing. On the meridional plane of the GIWAXS pattern for all oligoprolines, 1Ra–1Re, one or more higher order reflections appear which are related to the intercalated double layer (Figure 2b). This assembly is based on a hydrophobic inner part consisting of the intercalated PMI units and outer hydrophilic oligoprolines. The d-spacing of the double layer is determined from the 1st order reflection and slightly changes between the differently long oligoprolines with 23.20 Å for 1Ra and 1Re, 25.00 Å for 1Rc and 1Rd, as well as 23.60 Å for 1Rb. More importantly, the number of higher reflections strongly differs between the compounds implying variations in long-range order of the assemblies. While the patterns display only the first order peak for 1Ra, 1Rb and 1Re, oligoprolines 1Rc and 1Rd give rise to reflections up to 4th order. From these results, it can be concluded that the oligoproline length of 1Rc and 1Rd seem to possess an optimum persistence length to yield higher order than in the case of 1Ra, 1Rb and 1Re. In the case of the longest oligoproline 1Re the oligoproline backbone is probably too flexible to allow even a packing of the PMI units within the double layer.

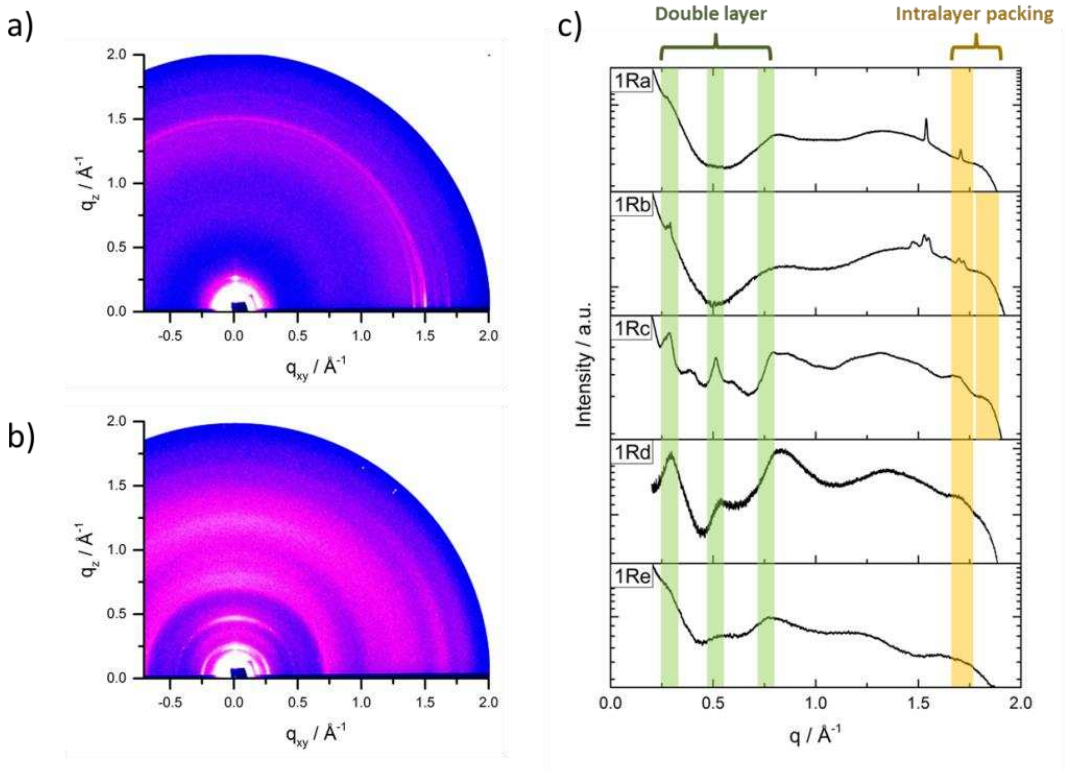

Figure 2. GIWAXS pattern of 1Rb a) and 1Rc b) after deposition from a solution in THF:H_2O (30:70); c) 1D GIWAXS profiles of 1Ra–1Re as a function of scattering vector q. The reflections for the double layer structure and the intralayer packing of the PMI units are indicated in the integrations.

1. U. Lewandowska, W. Zajaczkowski, L. Chen, F. Bouilliere, D. P. Wang, K. Koynov, W. Pisula, K. Müllen and H. Wennemers, *Angew Chem Int Edit*, 2014, **53**, 12537-12541.
2. U. Lewandowska, W. Zajaczkowski, W. Pisula, Y. Ma, C. Li, K. Müllen and H. Wennemers, *A European Journal*, 2016, **22**, 3804-3809.

Impact of osmotic stress and excluded volume on protein-protein interactions

Karin Julius[1], Michael Paulus[1], Jonathan Weine[1], Julian Schulze[1], Karin Esch[1], Metin Tolan[1], and Roland Winter[2]

[1] *Fakultät Physik / DELTA, Technische Universität Dortmund, 44227 Dortmund, Germany*

[2] *Fakultät für Chemie und Chemische Biologie, Technische Universität Dortmund, 44227 Dortmund Germany*

Inside cells, proteins are surrounded by different macromolecules, including proteins themselves, which cover approximately 30% of the available volume. It has been shown that the reduction of free space and the accompanied change of osmotic pressure has a significant impact on the conformational stability, dynamics and hence reactivity of proteins, which changes also their resistance to temperature or pressure-induced denaturation [1]. The aim of the experiment was the investigation of the impact of crowder molecules of various sizes and chemical properties on protein-protein interactions in highly concentrated aqueous lysozyme solutions, and how these interactions are modulated by changes in water structural properties, by osmotic pressure, and by the macro-/nanoconfinement theses crowders impose. As model crowding agents the inert, polar and hydrophilic polysaccharide Ficoll PM 70 and its subunit sucrose are chosen.

SAXS measurements were performed at DELTA, Dortmund, bl9 with a custom build high pressure cell [2] with removed diamond windows at ambient pressure at a sample temperature of 25 °C. An incident energy of 10 keV and a sample-to-detector distance of 1,1 m was used. To obtain the intermolecular interaction potential as a function of crowder concentration and crowder identity, SAXS curves of 15-20 (w/v) % aqueous lysozyme solutions in 25 mM BisTris buffer at pH 7 were recorded for Ficoll PM 70 and sucrose concentrations ranging from 5 to 25 (w/v)%.

Due to the marked increase of background scattering in case of the macromolecular crowding agent Ficoll, the correlation peak containing information on the intermolecular interaction between the protein molecules cannot be analyzed with sufficient accuracy beyond crowder concentrations of 10 wt.-% at lysozyme concentrations of 20 wt-% (FIG. 2.). Up to that crowder concentration, a marked shift of the correlation peak relative to the scenario in pure buffer solution is not observed, which can be explained by the strong repulsive protein-protein interactions of the highly positive charged lysozyme molecules (z=8 at pH 7) in this protein solution, which can still be described by a relative open network structure at this macromolecular crowder concentration. In sucrose solutions, the background remains essentially flat in the q-range of interest. For the nanomolecular crowder sucrose, the second virial coefficient and the strength of the attractive part, $J(c)$, of the intermolecular protein-protein interaction potential, $V(r)$, have been derived for dense lysozyme solutions from SAXS data as a function of crowder concentration, applying a liquid-state theoretical approach. We observe a linear decrease of attractivity of the interaction potential with increasing sucrose concentration at ambient pressure. Different from the scenario observed for the macromolecular crowder, this indicates that marked changes of osmotic pressure induced by the nanocrowder sucrose at high concentrations in concert with the reduction of space owing to the excluded

volume effect, affect the intermolecular forces significantly (FIG 1. a-c). The effect observed may be explained -at least in part- by the repulsive excluded volume effect induced by the presence of the strongly hydrophilic sucrose [3].

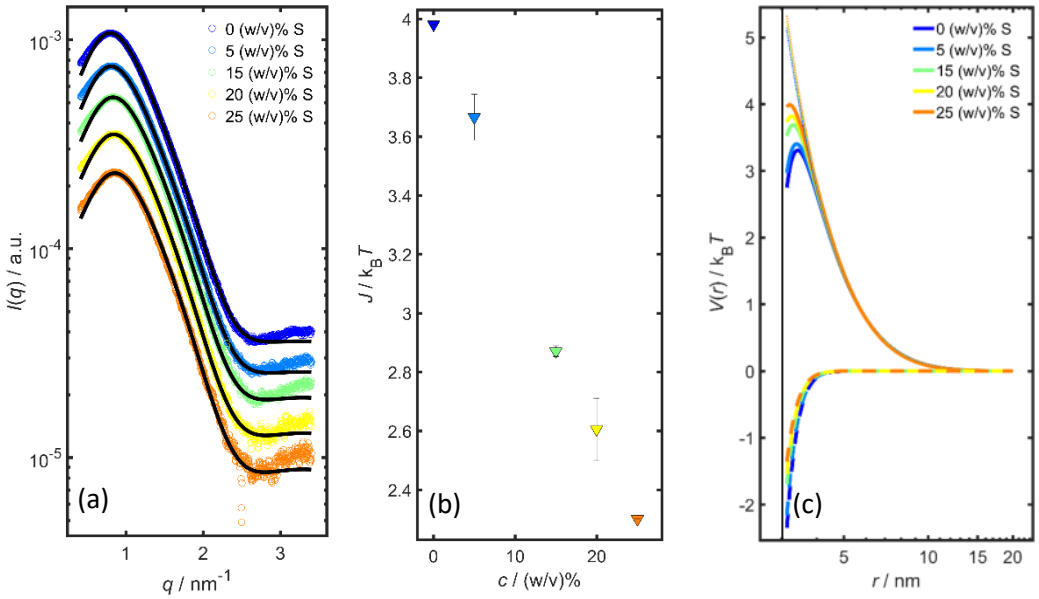

FIG. 1 (a) Experimental SAXS intensities of a 15 (w/v)% lysozyme solution at 25 °C, ambient pressure and pH 7 for sucrose concentrations of 0 to 25 (w/v)% and the refinement of the data. (b) The experimentally determined strength, $J(c)$, of the attractive part of the interaction potential for sucrose concentrations up to 25 (w/v)%. (c) Total protein-protein interaction potential, $V(r)$ (solid line), derived of the sum of a repulsive screened Coulomb potential (dotted line), a hard sphere potential (black solid line) and an attractive Yukawian type part (dashed line) as a function of crowder concentration.

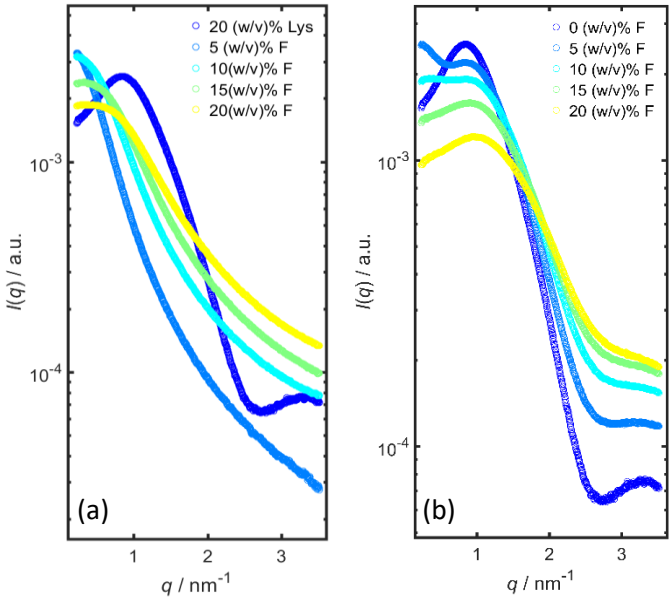

FIG. 2 (a) Experimental SAXS intensities of a 20 (w/v)% lysozyme solution and pure 5-20 (w/v)% Ficoll PM 70 solutions at 25 °C, ambient pressure and pH 7. (b) Data for the corresponding protein-crowder mixtures for 20 (w/v)% lysozyme

[1] Erlkamp, M., Grobelny, S., & Winter, R. (2014). Crowding effects on the temperature and pressure dependent structure, stability and folding kinetics of Staphylococcal Nuclease. *Physical Chemistry Chemical Physics : PCCP*, *16*(13), 5965–76.

[2] Krywka, C., Sternemann, C., Paulus, M., Tolan, M., Royer, C., & Winter, R. (2008). Effect of osmolytes on pressure-induced unfolding of proteins: A high-pressure SAXS study. *ChemPhysChem*, *9*(18), 2809–2815.

[3] Ravindra, R., & Winter, R. (2004). Pressure perturbation calorimetry: A new technique provides surprising results on the effects of co-solvents on protein solvation and unfolding behaviour. *ChemPhysChem*, *5*(4), 566–571.

The behavior of trypsin at the solid-liquid interface and under high hydrostatic pressure

Lukas Tepper, Michael Paulus, Susanne Dogan, Göran Surmeier, Julian Schulze and Metin Tolan

Fakultät Physik/DELTA, TU Dortmund, 44221 Dortmund, Germany

Trypsin is a well known protein in biological and chemical research and used for many applications in the industry. The understanding of the behavior of trypsin at different interfaces like biological membranes is important for different research areas.

In this project the interaction of trypsin with hydrophilic interfaces is analyzed. We studied the behavior of trypsin at the solid-liquid interface between a hydrophilic silicon wafer and aqueous protein-solution using x-ray reflectivity (XRR). The focus of the project was the behavior of trypsin under high hydrostatic pressure (HHP) up to 5 kbar.

This experiment was performed at beamline BL 9 using the 27 keV XRR setup. We used an incident x-ray energy of 27 keV to go through the buffer solution in the cell and to prevent radiation damage. Trypsin was solved in a BisTris buffer at pH 7.5 with 0.1 mg/ml. In this pH-range trypsin has its highest activity. All measurements were performed at room temperature. We used a high pressure cell described in [1]. The pressure was increased from 50 to 5000 bar.

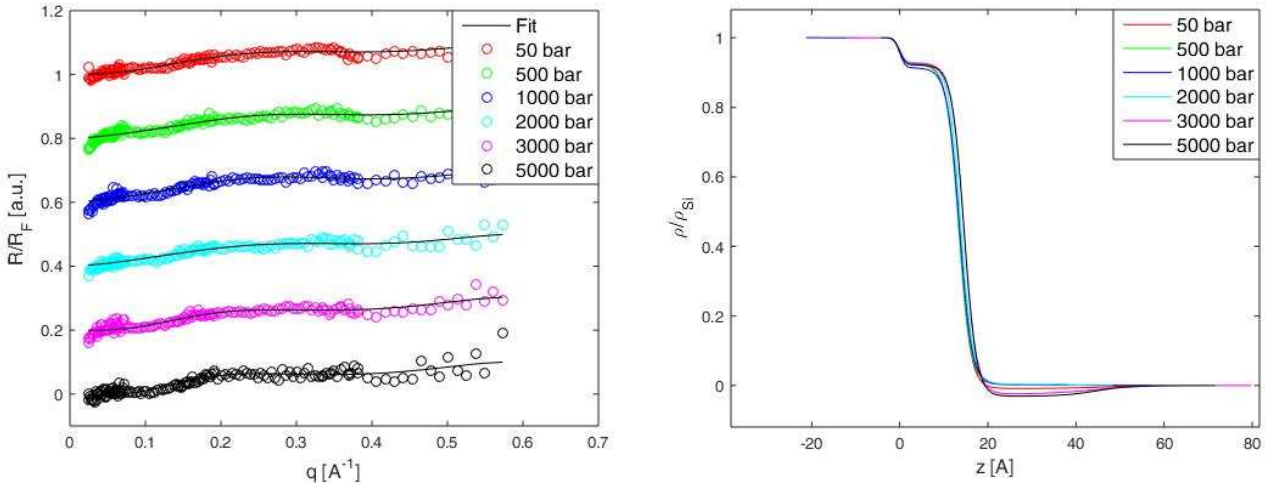

Figure 1: XRR data of trypsin under high hydrostatic pressure divided by the Fresnel reflectivity (left) and electron density profiles obtained by a fit of the XRR data minus the electron density of water (right).

Figure 1 shows the reflectivity curves and the electron density profiles obtained from a fit of the reflectivity data. The measurements show a pressure dependence. With rising pressure, a layer with approximately 20 Å thickness forms at the interface due to a pressure depended adsorption of tryspsin at the interface.

Acknowledgment:
The authors thank the DELTA machine group for providing synchrotron radiation. This work was supported by the Cluster of Excellence RESOLV funded by Deutsche Forschungsgemeinschaft.

References

[1] F. Wirkert, M. Paulus, J. Nase, J. Möller, S. Kujawski, C. Sternemann and M. Tolan, *X-ray reflectivity measurements of liquid/solid interfaces under high hydrostatic pressure*, Journal of Synchrotron Radiation **21**, 76 (2014)

Hard X-ray spectroscopy

Biotransformation evidence of copper nanoparticles in cowpea (Vigna unguiculata) by XANES

C.O. Ogunkunle[a,b], B. Bornmann[b], R. Wagner[b], P.O. Fatoba[a], R. Frahm[b], D. Lützenkirchen-Hecht[b]

[a] *Environmental Biology Unit, Department of Plant Biology, University of Ilorin, Ilorin, Nigeria*
[b] *Fakultät 4-Physik, Bergische Universität Wuppertal, Gaußstr. 20, 42097 Wuppertal, Germany*

The rapid advancement of nanotechnology has resulted in increased production and use of commercially engineered nanoparticles (NPs). Due to their small size of typically less than 100 nm, those NP materials are thought to have antimicrobial properties and a potential risk of a phyto-toxicity. Due the numerous uses of nanosized Cu and its oxides especially in the agricultural sector [1], there is high potential to gain the Cu NPs into the food chain, for example through contamination of food crops [2, 3]. Up to now it is not well understood if the toxicity potential of CuNPs and its oxides is as a result of chemical speciation/transformation in the plants or not, as only few studies have been carried out on the biotransformation and speciation of metal nanoparticles in plants, and there is a huge lack of information especially for CuNPs (e.g. [4-6]). Therefore, this study aims to investigate the uptake and translocation of CuNPs and the effects on some micro-nutrients in cowpea, and its transformation/speciation using the synchrotron X-ray absorption near-edge spectroscopy (XANES). For this purpose, test soil (pH=6.0) collected from the Botanical garden of the University of Ilorin, Nigeria, was air-dried and sieved (<2 mm). 2.5 kg of potted soil were loaded with an amount of 1000 mg of spherical CuNPs (Ionic Liquids GmbH, Germany) with an average particle size of 25 nm. This concentration appears to be a reasonable value in comparison to the maximum concentration of 1000 mg/kg as recommended for ecotoxicological tests of chemical substances according to the ISO guideline 11269-2 [7].

Seeds of cowpea (*Vigna unguiculata*) of accession no-A1 8462 were collected from the International Institute for Tropical Agriculture (IITA, Nigeria). The seeds were treated in 10% sodium hypochlorite solution for 10 minutes to ensure surface sterility [8], followed by two consecutive rinsing with deionized water (DW). Five seeds were planted in a pot and left to germinate. Irrigation was carried out every day with 100-150 ml DW throughout the period of the experiment, and the seeds were allowed to grow for the exposure period of 21 days. Subsequently, the plants were harvested, washed with DW to remove adhering soil material and freeze-dried for the synchrotron measurements at DELTA beamline 10. Cu speciation was done in the root, stem and leafs of the plants.
In Fig. 1, X-ray fluorescence spectra of different samples excited with a beam of 9100 eV photon energy are compared. As can be seen, the Cu contributions increase from the control sample (roots of plants grown in a soil with a Cu level <1mg/kg) with a value of about 6.7 mg/kg dried weight, to the leaves and the stem with about 25 mg/kg. The highest Cu content was measured for the roots with a concentration of about 164 mg/kg. Various other cations such as K, Ca, Ti, Mn and Fe are detectable at different levels. Changes in these may as well be attributed to the growth in the CuNP-loaded soil and will be subject of a forthcoming publication [9].

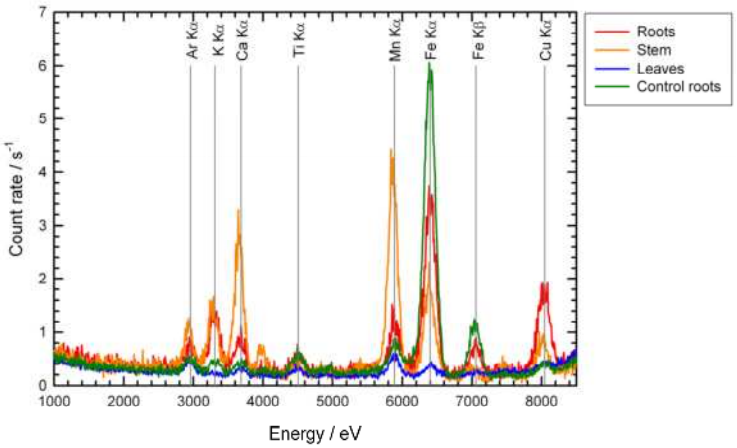

Fig. 1: X-ray fluorescence spectra of different parts of cowpea plants grown in soil loaded with CuNPs (1000 mg per 2.5 kg soil) excited with 9100 eV photons. Cu-contributions increase from the control roots (no extra Cu NPs added, Cu level below 1 mg/kg), to the leaves, the stem and the roots of the investigated cowpea plants. Various other cations (K, Ca, Ti, Mn, Fe) are also detectable.

Cu K-edge XANES data of the roots were measured in the fluorescence mode using an energy-dispersive silicon drift diode (SDD) with a multichannel analyzer (Amptek XR100 SDD) and a large-area PIPS-diode, respectively. Several scans from 8920 eV to 9130 eV photon energy with typically 250 data points each with 10-12 s integration time per data point were collected and averaged. Spectra related to samples from the roots, the stem and the leaves as well as several reference samples (Cu metal foil, CuNPs, Cu_2O, CuO, and Cu-histidine [9], Cu-nicotianamine [9], Cu-glutathione[9]) were measured and analyzed. In Fig. 2, XANES spectra at the Cu K-edge obtained from the roots are compared to those of selected Cu reference materials and the CuNPs. From the edge position, a Cu-valence close to +2 in the cowpea plant material can clearly be derived. Furthermore, the shape of the spectrum is very similar to that of the Cu^{2+} reference materials, especially to CuO and Cu-nicotianamine, suggesting that a copper uptake and biotransformation of the CuNPs has occurred. A more detailed evaluation and publication of the data is currently under way [10].

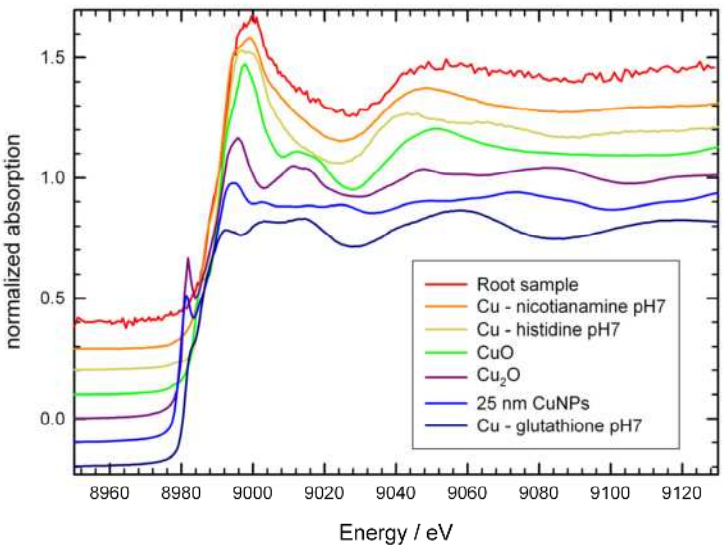

Fig. 2: Normalized Cu K-edge XANES spectra of the cowpea root sample in comparison to several Cu reference materials Cu-metal, CuNPs, Cu_2O, CuO, Cu-nicotianamine [9], Cu-histidine [9] and Cu-glutathione [9].

Acknowledgement

We gratefully acknowledge the DELTA machine group for providing synchrotron radiation reliably. C.O. Ogunkunle would like to thank the TWAS and DFG for the financial support of his visit in Wuppertal under contract no. LU 796/3-1. We also acknowledge the provision of Cu-nicotianamine, Cu-histidine and Cu-glutathione reference spectra from Ana Mijovilovich and Wolfram Meyer-Klaucke [9].

References

[1] J. Trujillo-Reyes, S. Majumdar, C.E. Botwz, J.R. Peralta-Videa, J.L. Gardea-Torresdey, J. Hazard. Mater. 267 (2014) 255.
[2] Y.-N. Chang, M. Zhang, L. Xia, J. Zhang, G. Xing, Materials 5 (2012) 2850.
[3] M.L.J. Xu, H. Iwai, Q. Mei, D. Fujita, H. Su, H. Chen, N. Hanagata, Sci. Rep. 2 (2012) 406.
[4] P. Zhang, Y. Ma, Z. Zhang, X. He, J. Zhang, Z. Guo, R. Tai, Y. Zhao, Z. Chai, ACS Nano 6 (2012) 9943.
[5] M.L. Lopez-Moreno, G. de la Rossa, J.A. Hernandez-Viezcas, H. Castillo-Michei, C.E. Botez, J.R. Peralta-Videa, J.L. Gardea-Torresdey, Environ. Sci. Technol. 44 (2010) 7315.
[6] Y. Ma, P. Zhang, Z. Zhang, X. He, J. Zhang, Y. Ding, J. Zhang, L. Zhang, Z. Guo, L. Zhang, Z. Chai, Y. Zhao, Environ. Sci. Technol. 49 (2015) 10668.
[7] ISO Guideline 11269-2: Soil Quality - Determination of the Effects of Pollutants on Soil Flora - Part 2: Effects of Contaminated Soil on the Emergence and Early Growth of Higher Plants. International Organization for Standardization, Geneve, Switzerland.
[8] Ecological Effects Test Guidelines (OPPTS 850.4200): Seed Germination/Root Elongation Toxicity Test. http://www.epa.gov/opptsfrs/publications/OPPTS_Harmonized/850_Ecological_Effects_Test_Guidelines/Drafts/850-4200.pdf
[9] A. Mijovilovich, B. Leitenmaier, W. Meyer-Klaucke, P.M.H. Kroneck, B. Götz, H. Küpper, Plant Physiology 151 (2009) 715.
[10] C.O. Ogunkunle, B. Bornmann, P.O. Fatoba, R. Wagner, D. Lützenkirchen-Hecht, Environ. Sci. Technol., in preparation.

The local structure of concentrated yttrium(III) chloride aqueous solutions under high hydrostatic pressure

Mirko Elbers[1], Christian Sternemann[1], Michael Paulus[1], Karin Julius[1], Nico König[1], Göran Surmeier[1], Karin Esch[1], Holger Göhring[1], Jennifer Bolle[1], Ralph Wagner[2] and Metin Tolan[1]

[1]Fakultät Physik/DELTA, TU Dortmund, 44221 Dortmund, Germany
[2]Bergische Universität Wuppertal, 42119 Wuppertal, Germany

The interaction between proteins strongly depends on the surrounding aqueous solution. Modifications in the surrounding water structure e.g. by the addition of ions or the application of pressure have a direct impact on the protein-protein interaction [1]. For instance, pressure dependent small angle x-ray scattering experiments have shown a minimum in the interaction strength at approximately 2 kbar [1]. This minimum was assigned to a collapse of the second hydration shell of water [2]. By adding kosmotropic salt ions to the aqueous solution, the minimum shifts to higher pressures due to the stabilization of the water structure [3]. The influence of the salt ions on the local water structure is therefore crucial for the understanding of the protein-protein interaction process. Thus, aqueous salt solutions with different concentrations under hydrostatic pressure were investigated by extended x-ray absorption fine structure (EXAFS) measurements, which provide an insight into the near environment of the yttrium ions.

We performed the EXAFS experiments at beamline BL 8 at DELTA in transmission geometry and with a high-pressure cell developed by C. Krywka [4]. To investigate the concentration dependence of the structural changes in the local environment of the yttrium ion, five different YCl_3 concentrations (0.1M, 1M, 2M, 2.5M, 3M) were used. For each concentration, EXAFS spectra were recorded as a function of pressure in the range from 50 bar to 5000 bar with a step size of 500 bar.

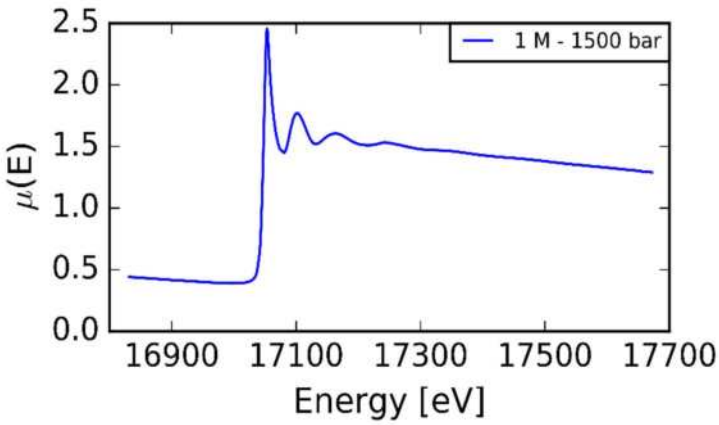

Figure 1: EXAFS spectrum for the 1M aqueous YCl_3 solution at 1500 bar

A raw spectrum for the 1M concentration at 1500 bar is shown in figure 1. Standard procedures were used for the background removal to extract the relevant EXAFS oscillation for further analysis [5]. The obtained spectra as example for the 2M solution are shown in the upper graph in figure 2 (a) at different pressure steps between 500 bar and 4500 bar. The spectra are plotted in the momentum space $k = \sqrt{\frac{2m_e}{\hbar^2}(E - E_0)}$, where E_0 is the inflection energy. To emphasize the oscillation in the relevant k-range, the spectra are weighted with a factor of k^2. In the lower graph, all concentrations at 2000 bar are plotted for a better comparison. The qualitative analysis of the spectra doesn't show a pressure or concentration dependent change in the atomic distances, which would result in a shift to higher or lower k-values, respectively. The Fourier transform (FT) of the EXAFS spectrum gives the pseudo-radial distribution function (RDF) of the yttrium ion, which is shifted to lower R-values due to the influence of the atomic potentials. Here, R describes the distance to the yttrium ion. The FT of the spectra are plotted in figure 2 (b). No obvious changes in the atomic distances as a function of pressure or concentration were found. The maximum at 1.82 Å corresponds to the distance of the first coordination shell at approximately 2.34 Å - 2.36 Å [6].

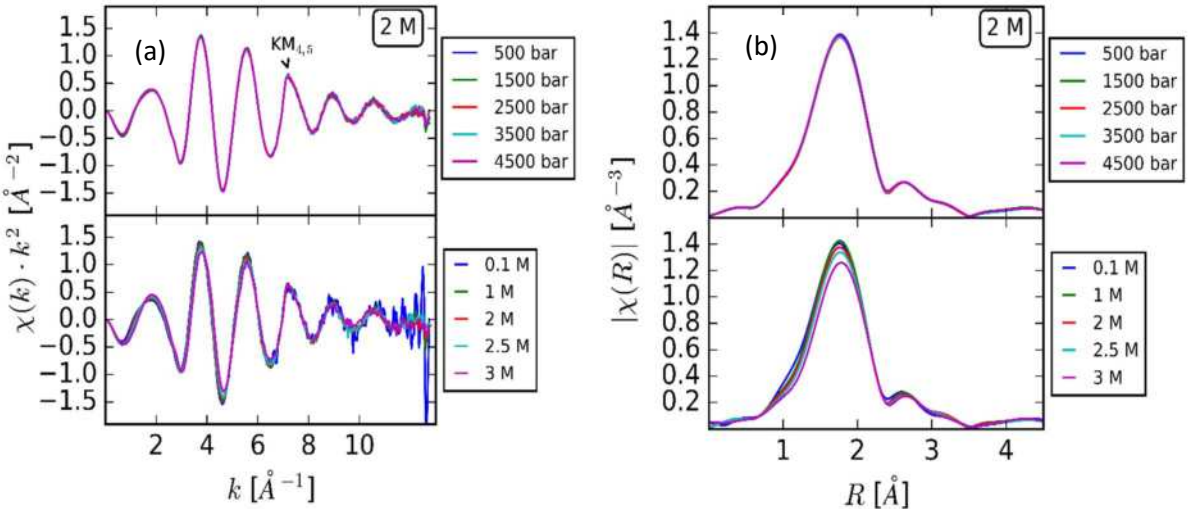

Figure 2: (a) TOP: EXAFS spectrum of the 2M solution at different pressure steps. The peak at $k = 7.2$ corresponds to a double electron excitation BOTTOM: spectrum of the different measured concentrations. (b) FT of the spectra in figure 2 a

For a quantitative and advanced analysis of the experimental data, molecular dynamic simulations for the different concentrations at ambient pressure were performed. The theoretical EXAFS spectra of the obtained structures were calculated with FEFF and fitted to the recorded spectra. By using the distance between the yttrium ion and the first coordination shell as a fit parameter, small radial changes could be examined. The chloride ions were neglected due to their low contribution to the theoretical EXAFS spectrum. The resulting radii of the first coordination shell at different pressure steps are shown in figure 3 (a) as an example for the 1M solution. The absolute error in the determination is given in the radius at 1 bar. Furthermore, to quantify the compression and to compare the different concentrations, linear regressions of the obtained data were performed for each concentration. The compression shows a concentration depended behavior as with increasing concentration the amount of the slope rises. However, the occurring effect is contrary to the macroscopic behavior of salt solutions, since it is known that a higher concentration leads to a weaker compressibility. For further explanation of the results additional measurements at higher pressures and more concentrations are necessary. Furthermore, additional measurements with better statistics would reduce the large absolute error in the determination of the shell radius.

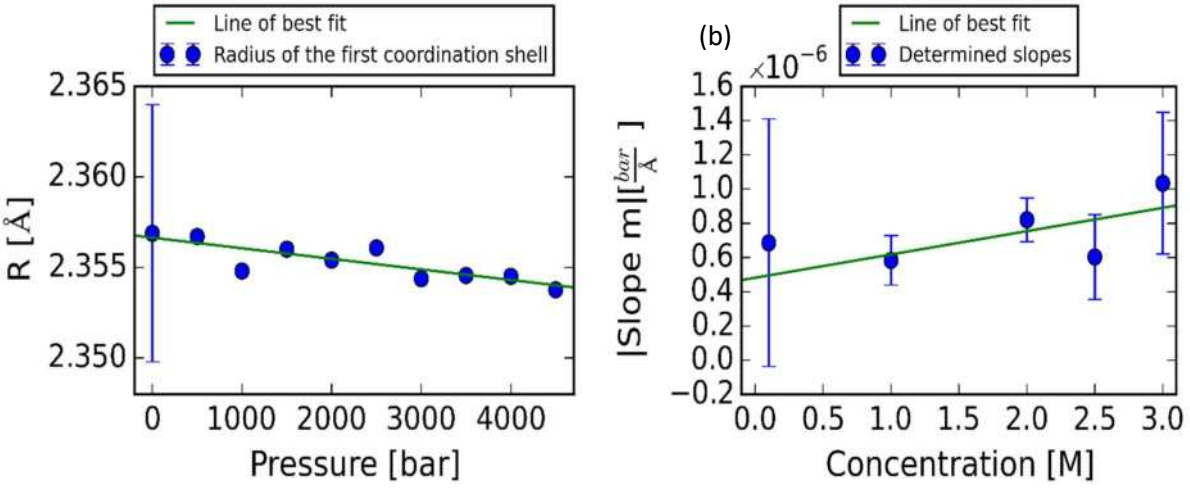

Figure 3: (a): The resulting radii of the first hydration shell for the 1M solution with the performed linear regression. The absolute error in the determination is shown in the radius at 1 bar (b) resulting slopes of the different concentrations obtained from linear regression

We acknowledge T. Irifune and the joint usage/research center for PRIUS at the GRC (Ehime University, Japan) for providing nano-polycrystalline diamond discs, DELTA for providing synchrotron radiation, the Cluster of Excellence RESOLV (EXC 1079), the DFG(FOR1979) and DFG through TRR160 for financial support.
References: [1] M.A. Schroer et al. (2011) [2] A.K. Soper et al. (2000) [3] J. Möller et al. (2014) [4] C. Krywka et al. (2008) [5] M. Newville et al. (1993) [6] S. Díaz-Moreno et al. (2000)

In-situ EXAFS experiments during Co-electrodeposition

Damir Hamulić[a,b], Dirk Lützenkirchen-Hecht[b]

[a]*Faculty of Chemistry and Chemical Technology, University of Ljubljana, Večna pot 113, 1000 Ljubljana, Slovenia*
[b]*Fakultät 4-Physik, Bergische Universität Wuppertal, Gaußstr. 20, 42097 Wuppertal, Germany*

Cobalt-based coatings have potential applications e.g. in energy storage systems [1] and solar energy conversion [2]. They are used in electrochromic [3] and magnetoresistive devices [4], and may possess catalytic activity [5]. In general, electrodeposition is a versatile technique for the preparation of metal and oxide coatings, and the facile variation of the deposition conditions such as the pH, temperature, the concentration of anions, cations and additives in the electrodeposition solution as well as the deposition potential may be used to prepare films with tailored properties. In addition to previous ex-situ experiments using a combination of electrochemistry, EXAFS and scanning electron microscopy to study the resulting film structure, thickness and morphology [6], we will consider the first in-situ EXAFS experiments performed during the electrodepostion of Co from 0.02 M $CoCl_2$-solutions in the present contribution.
All the EXAFS experiments have been performed at DELTA beamline 10 in the transmission mode using a channelcut Si(111) monochromator and gas-filled ionization chambers as detectors. Cobalt electrodeposition took place at room temperature in a customized three-electrode cell (see Fig. 1) with a PTFE body containing ca. 20 cm^3 of electrolyte and Kapton windows for the X-ray beam. A gold-coated Kapton foil served as working electrode, a platinum wire as counter electrode, and an Ag/AgCl reference electrode (E^0_h = 0.210 V) was employed, against which all potentials are reported. Each EXAFS scan from 7705 to 7775 eV (150 data points with 0.31 s each) took 60 s including backscan, and in total a deposition time of one hour was measured in-situ.

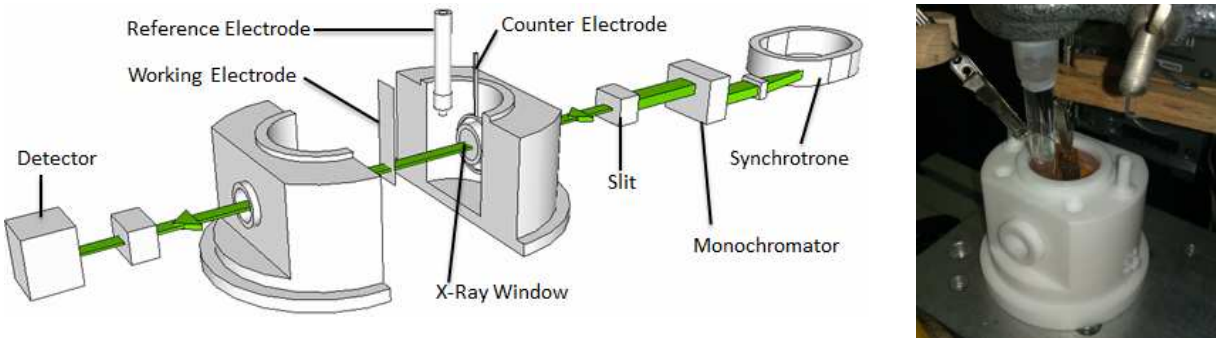

Fig. 1: (left) Schematic representation of the experimental setup at BL10. The intensity of the X-rays from the Si(111) monochromator was measured using an ionization chamber in front of the electrochemical cell with about 20 ml of electrolyte. The working electrode is a 120 μm Kapton foil coated with a sputter deposited Au-layer of ca. 200 nm thickness. Kapton entrance and exit windows of the electrochemical cell provide a liquid layer of variable thickness so that the contributions of the electrolyte to the measured EXAFS signal are not too large. The cell is equipped with an Ag/AgCl reference electrode and a Pt-wire as counter electrode. (right) Photo of the setup.

The course of the Co-deposition reaction can be followed in the XANES spectra shown in Fig. 2(a). For short deposition times, the spectra are governed by the 0.02M $CoCl_2$ electrolyte solution, while with increasing time, the Co-deposits contribute more and more to the measured spectra. From our previous experiments, we could conclude that Co-metal deposition occurs for the chosen electrochemical conditions [6]. Thus, we have modeled the measured data by a linear combination fits of the $CoCl_2$-solution and Co-metal reference spectra, and some representative results are presented in Fig. 2(b). The excellent agreement between the measured data and the fits with extremely small fit residuals is obvious, allowing to exclude any intermediate species besides the Co^{2+} in the solution and the Co-metal deposits.

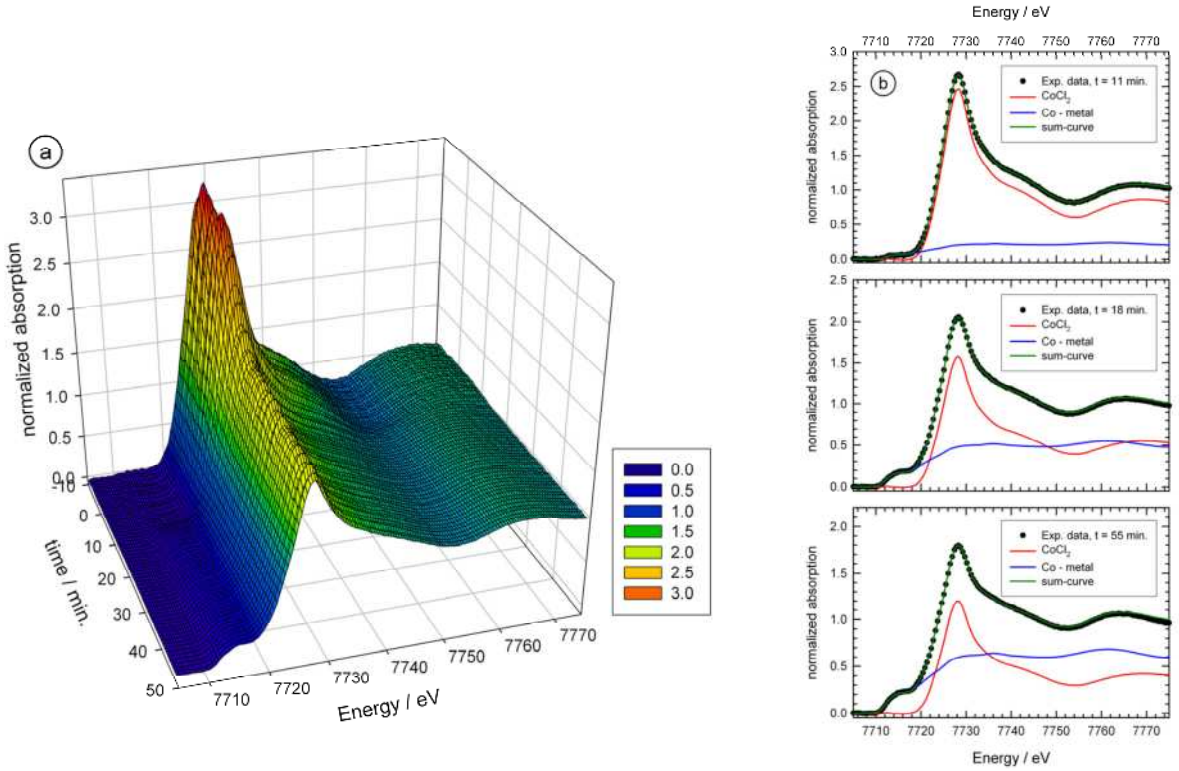

Fig. 2: (*a*) time-resolved in-situ XANES measurements during the electrodeposition of Co in 0.02M $CoCl_2$ for a potential of -1.11 V vs. Ag/AgCl at the Co K-edge. **(b)** Linear combination fits of some selected spectra using Co-metal and liquid $CoCl_2$ as references. The increase of the metal contributions with time is obvious.

In Fig. 3, the time evolution of the concentration of Co-metal and $CoCl_2$ according to the LC-fit analysis are depicted. As can be seen, there is a rapid increase of the metal after about 6 minutes of polarization, however the growth slows down after ca. 20 minutes, with a slower growth rate thereafter. This can be explained by a fast consumption of the Co^{2+} close to the working electrode for shorter deposition times and an accordingly fast growth. If the solution is depleted from Co^{2+}, the diffusive motion to the working electrode is slower, resulting in a decreased deposition rate of the Co-metal.

Future in-situ studies are planned to address the effect of the electrolyte on the details of the Co-deposit growth and morphologies, and the kinetics of the growth.

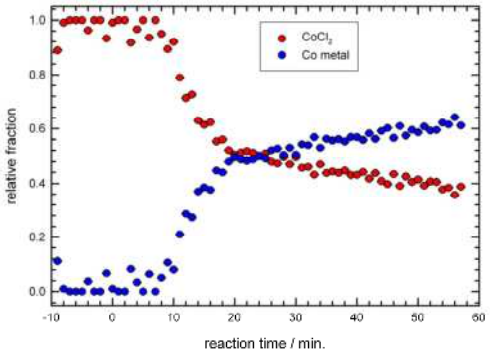

Fig. 3: Compilation of the LC-fit results obtained from the analysis of the time-resolved in-situ XANES measurements during the electrodeposition of Co in 0.02M $CoCl_2$ for a potential of -1.11 V vs. Ag/AgCl at the Co K-edge. The growth slows down for larger deposition times potentially due to the diffusive transport of Co^{2+} to the working electrode.

Acknowledgement

We gratefully acknowledge the DELTA machine group for providing synchrotron radiation reliably. D. Hamulić would like to thank the ERASMUS student exchange programme for the financial support of his visit in Wuppertal.

References

[1] J.J. Auborn, Y.L. Barberio, J. Electrochem. Soc. 134 (1987) 638.
[2] E. Barrera, I. Gonzales, T. Viveros, Solar Energy Mat. Solar Cells 51 (1998) 69.
[3] P.M.S. Monk, S. Ayub, Solid State Ionics 99 (1997) 115.
[4] Y. Ueda, N. Kikuchi, S. Ikeda, T. Houga, J. Magn. Mater. 198 (1999) 740.
[5] I.G. Casella, M.R. Guascito, Electrochim. Acta 45 (1999) 1113.
[6] D. Hamulić, D. Lützenkirchen-Hecht, DELTA annual report (2015) 83.

Analysis of temperature-induced formation of lubricous oxides in vanadium-doped iron based arc sprayed coatings

Wolfgang Tillmann[a], Leif Hagen[a], David Kokalj[a], Michael Paulus[b], Metin Tolan[b]

[a]Institute of Materials Engineering, TU Dortmund University, Germany

[b]Fakultät Physik / DELTA, TU Dortmund University, Germany

Introduction

For many technical applications the optimization of surfaces, e.g. of tools, is fundamentally [1]. Increasing demands, for example in dry machining, lead to increased friction forces and high temperatures [2], whereby a shortened life time occurs [3]. Accordingly, the focus is on coatings which adaptively form thin oxide reaction films at elevated temperatures [3]. For this purpose, particularly oxides of transition metals (Mo, Ti, V and W) are attractive because they form oxides of the Me_xO_{3x-1}, Me_xO_{2x-1} or Me_xO_{3x-2} type (Magnéli-phases) with a plurality of sliding planes to minimize friction forces [4]. In terms of coating technologies, Bobzin et al. [4] emphasize the relevance of vanadium for lubrication. According to this study, the formation of specific vanadium oxides under thermal load such as vanadium pentoxide (V_2O_5) possess an enhanced friction behavior due to its low decohesion energies G and consequently act as solid lubricant above the melting point of 678°C [5] respectively 670°C [6]. In terms of vanadium oxides, its oxidational state along the temperature range (between room temperature and 750°C) as well as the oxidizing environment play a significant role.

In the case of thin film technologies, vanadium-doped PVD coatings have already been studied by a number of authors with respect to their tribological behavior. Nevertheless, the triblogical behavior and the oxidation of vanadium-doped arc sprayed coatings have not been investigated yet. Therefore, iron-vanadium coatings have been deposited by the Twin Wire Arc Spraying (TWAS) process with regard to their oxidation behavior at elevated temperatures. The aim of this study was the identification of vanadium oxides and the correlation of the influence on the tribological properties observed in dry sliding experiments.

Experimental

As substrate material round C45 steel specimens with a diameter of 40 mm and thickness of 6 mm were used. Before spraying, the surfaces of the samples were sand blasted with corundum and afterwards cleaned in an ultrasonic bath filled with ethanol. As feedstock material two different cored wires (Fa. Durum Verschleissschutz, Germany) with a diameter of 1.6 mm were used. The vanadium doped cored wire (referred to as “Fe-V”) consists of approximately 29.9 wt.% of V (in wt.%: 0.07 C, 0.25 Mn, 0.33 Si, 0.38 Al, 29.91 V, Bal. Fe). As opposed to that, a low carbon steel wire delivered as cored wire (in wt.%: 0.07 C, 0.11 Si, 0.25 Mn, Bal. Fe) serves as a reference (referred to as “Fe-Fe”). In order to deposit the coatings, the Smart Arc 350 PPG spraying system (Fa. Oerlikon Metco, Switzerland) was utilized. **Table 1** summarizes all parameter settings which have been employed for deposition of both feedstock materials. The layers were produced by applying two overruns for each specimen.

Tab. 1: *Spray parameter settings*

Handling parameters		**Spray parameters**	
Spray angle [°]	90	Voltage [V]	28
Spray distance [mm]	95	Current [A]	180
Gun velocity [m/s]	200	Primary gas pressure [MPa]	0.6
Track pitch [mm]	5	(compressed air)	

To investigate the tribological behavior of the coatings, high temperature ball-on-disk (BOD) tests at 25°C and from 350°C up to 750°C in 100°C steps were performed with the “HighTemperature

Tribometer" (Fa. CSM, Switzerland). Before the BOD tests the surface of all samples was machined and polished. An alumina ball (2300 HV) with 6 mm diameter and a load of 5 N was used as counter body. A sliding distance of 200 m without lubricant was employed. The velocity was kept at 40 cm/s and the radius of the circular path was maintained constant at 10 mm.

The oxidation state of the Fe-V coating was analyzed via X-ray absorption near-edge structure spectroscopy (XANES) at beamline BL10 of the synchrotron light source DELTA. The samples were annealed up to different temperatures (350°C, 450°C, 550°C, 650°C, 750°C) utilizing a heat plate with graphite dome, type DHS 1100 (Fa. Anton Paar, Austria) and investigated in-situ. As well, the samples of the BOD tests have been characterized by ex-situ XANES. The measuring range was set to 60 eV before the vanadium K edge (5465 eV) up to to 100 eV after the edge. Before the edge the measuring was performed with 2 eV steps, in the region of the edge with 0.5 eV steps and after the edge with 1 eV steps and a time of 5 s per step. As monochromator, a silicon (111) crystal was used. The beam was set to a dimension of 1 mm height and 4 mm width. The detection of the absorption has been carried out by fluorescence.

Results

Within elevated temperature a decrease of the coefficient of friction (COF) of the Fe-V-coating can be observed (**Fig. 1**). In particular, above 550°C the COF drops significantly. Opposed to that, the COF of the Fe-Fe-coating remains constant over the whole temperature range. Up to 450°C the Fe-Fe coating shows a lower COF when compared to the Fe-V coating. Nevertheless, the Fe-V coating features a friction reduction of 42% at 750°C compared to the Fe-Fe-coating.

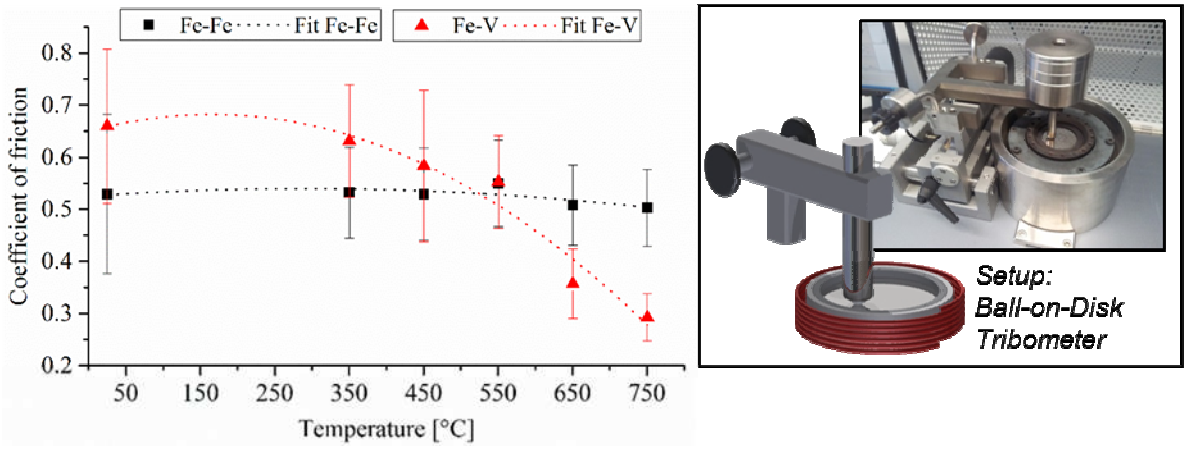

Fig. 1: *COF of different specimens for various temperatures taken in dry sliding experiments*

XRD-analyses in a previous study show that the Fe-V-coating forms low amounts of different vanadium oxides above 550°C. However, it has not clarified exactly which oxides allow the incipient friction drop of the Fe-V-coating at temperatures above 450°C. It has been shown that the formation of the vanadium oxides especially occurs in a thin oxide layer on the surface. The aim of XANES is to determine only the surface near oxides of the coatings.

The energy of the threshold is defined as the first peak in the derived absorption curve and describes the impermissible 1s→3d transition [8]. The second peak in the derived absorption curve describes the main edge [8]. In general, the intensity of the pre-edge can be used for analysis of symmetry properties [9]. In Contrast to e.g. chromium the intensity of the pre-edge peak of vanadium can rarely give alone accurate information about the state of oxidation, since vanadium shows for the same oxidation state different symmetries [9]. The absorption edge of the 1s→4p transition can be even more used to determine the oxidation state [9].

First of all, some vanadium reference oxides have been measured. The normalized results of the oxides (VO, V_2O_3, V_2O_4, V_2O_5, V_6O_{13}) and the vanadium foil are stacked plotted in **Fig. 2a**. It can be seen that the oxides show a striking pre-edge peak at 5.5 eV after the energy E_0 of the vanadium K-edge (5465 eV), the intensity increases with the oxidation number (**Tab. 2**). After the pre-edge peak for all measured references the absorption rises up to the point of the absorption edge and then oscillates. The examined references show a displacement of the transition from 19.5 eV for vanadium to 29.5 eV for V_2O_5. The energies of the main edges tend also to rise with the oxidation state from 8.8 eV to 14.4 eV.

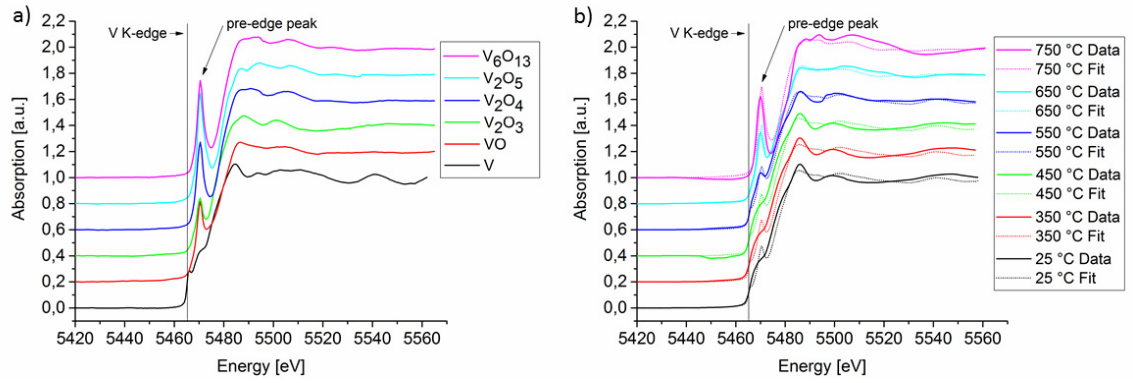

Fig. 2: *Ex-situ XANES at the V K-edge of the a) reference V-oxides and b) Fe-V coating obtained after different temperature treatments (25°C, 350°C, 450°C, 550°C, 650°C, and 750°C)*

Figure 2b shows normalized and stacked XANES diagrams of ex-situ measured Fe-V coatings depending on the temperature and also represents the appropriate linear combinations of the reference oxides. The Absorption at 25°C, 350°C and 450°C runs a similar course and shows no pronounced pre-edge peak (marked with * in Tab. 2). Starting from 550°C a pre-edge peak is formed which is more intense at 650°C and 750°C. All the fitted curves are consistent with the location of their pre-edge peaks and the 1s→4p transition of the measured coatings. Only the intensities the pre-edge peaks of the fitted curves up to 450°C are somewhat higher than in the measured curves. The higher intensities of pre-edge peaks from 550°C can be concluded that the coatings show a higher oxidation state than in the initial state. **Table 2** shows associated characteristic peak energies and intensities of the measured coatings.

Tab. 2: *Characteristic XANES values of the reference V-oxides and the Fe-V coating obtained after different temperature treatments (25°C, 350°C, 450°C, 550°C, 650°C, and 750°C)*

Phase	Oxidation-state	Threshold	Pre-Edge		Main-Edge	1s → 4p transition
		Position [eV]	Normalized intensity	Position [eV]	Position [eV]	Position [eV]
V	0	0	0,29	1	9,5	19,5
VO	2	3,9	0,62	5,5	8,7	21,5
V_2O_3	3	4	0,44	5,5	10,8	23
V_2O_4	4	3,9	0,67	5,5	13,2	26
V_6O_{13}	4,3	4,2	0,75	5,5	14,4	28,5
V_2O_5	5	4,2	0,85	5,5	13,8	29,5

Fe-V coating	Threshold	Pre-Edge		Main-Edge	1s → 4p transition
T [°C]	Position [eV]	Normalized intensity	Position [eV]	Position [eV]	Position [eV]
25	0,9	0,39*	5*	9,5	21
350	0,9	0,39*	5*	9,5	21
450	0,9	0,43*	5*	9,5	21
550	0,9	0,47	5	9,8	21
650	3,4	0,57	5	11,6	21
750	3,3	0,74	5	12,5	21

The following section is about the oxide composition of the measured coating surfaces. First, it is noted that the fitted compositions are not unique. There are also other compositions based on the available reference oxides possible, which also reflect the measurement curves well. Furthermore, it can be assumed that there are also other oxides than the investigated reference oxides on the surface. Moreover, it is noted that the selected oxides probably occur not only pure, but also in combination with iron. Up to 450°C the surface of the coating consists of about 41% V, 22% VO and 36% V_2O_3. At 550°C the initial formation of V_2O_5 with 0.3% part can be observed. At 650°C the content of V_2O_5 is already at 15%, while the proportion of vanadium goes back to 5% and the proportion of VO increases to 58%. Only at 750°C all selected reference oxides occur on the surface, however, pure vanadium is no longer available. The lowest part with 10% is shown by V_2O_3, while the proportion of VO is 13%, of V_2O_5 23%, of V_2O_4 24% and of V_6O_{13} 28%.

Summarizing, at low temperatures V, VO and V_2O_3 is shown on the surface and at elevated temperatures, a cover layer is formed, which consist additional of V_2O_4, V_2O_5 and V_6O_{13}. Concluding, this observed top layer is responsible for the friction decrease of the Fe-V-coating above 450°C.

Acknowledgement

The authors gratefully acknowledge the financial support of the DFG (German Research Foundation) within the Collaborative Research Centre SFB 708 subproject A1. The contributions of DURUM Verschleissschutz GmbH are gratefully acknowledged for their support in providing the vanadium-containing feedstock material. The authors would like to thank the DELTA machine group for providing synchrotron radiation.

References

1. Y.-S- Yang, T.-P. Cho, J.-H. Lin, Optimizing hydrophobic and wear-resistant properties of Cr–Al–N coatings, *The 6th International Conference on Technological Advances of Thin Films & Surface Coatings,* 2013*,* **544**, p 612–616.
2. R. Franz, J. Neidhardt, B. Sartory, B. R. Tessadri, C. Mitterer, Micro- and bonding structure of arc-evaporated AlCrVN hard coatings, *Thin Solid Films,* 2008*,* **516** (18), p. 6151–6157.
3. F. Fernandes, T. Polcar, A. Cavaleiro, Tribological properties of self-lubricating TiSiVN coatings at room temperature, *Selected Papers from The Society of Vacuum Coater's 57th Annual Technical Conference*, 2015, **267**, p. 8–14.
4. K. Bobzin, N. Bagcivan, M. Ewering, DC-MSIP/HPPMS (Cr,Al,V)N and (Cr,Al,W)N thin films for high-temperature friction reduction, *Surf. Coat. Technol.*, 2011, **205**, p 2887-2892.
5. H. A. Wriedt, The O-V (Oxygen-Vanadium) System, *Bulletin of Alloy Phase Diagrams*, 1989, **10**(3), p 271-277.
6. D. R. Lide, *CRC handbook of chemistry and physics, A ready-reference book of chemical and physical data*, CRC Press, Boca Raton, 2004
7. R. Franz and C. Mitter, Vanadium containing self-adaptive low-friction hard coatings for high-temperature applications, A review, *Surf. Coat. Technol.*, 2013, **228**, p 1-13.
8. J. Wong, F.W. Lytle, R.P. Messmer, K -edge absorption spectra of selected vanadium compounds, *Physical Review B.*, 1984, **10**, p. 5596–5610.
9. P. Chaurand, J. Rose, V. Briois, New methodological approach for the vanadium K-edge X-ray absorption near-edge structure interpretation: application to the speciation of vanadium in oxide phases from steel slag, *The journal of physical chemistry. B.,* 2007, **19**, p. 5101–5110.

XAS investigations of Eu-doped $BaAl_2O_4$. Part 1: XANES studies

D. Lützenkirchen-Hecht[a], B. Gržeta[b], M. Vrankić[b], S. Bosnar[c], A. Šarić[b], D. Petrov[d], R. Wagner [a]

[a]*Fk. 4-Physik, Bergische Universität Wuppertal, Gaußstr. 20, 42097 Wuppertal, Germany*
[b]*Division of Materials Physics, Ruđer Bošković Institute, Bijenička cesta 54, 10000 Zagreb, Croatia*
[c]*Division of Materials Chemistry, Ruđer Bošković Institute, Bijenička cesta 54, 10000 Zagreb, Croatia*
[d]*Department of Physical Chemistry, Plovdiv University, Tsar Asen Str. 24, 4000 Plovdiv, Bulgaria*

Alkaline earth aluminates such as $BaAl_2O_4$ are known as very suitable starting compounds for the preparation of fluorescent and phosphorescent doped materials. In particular, europium doped barium aluminate is a luminescent material with emission in the red spectral range when doped with trivalent Eu^{3+} ions, while doped with divalent Eu^{2+} ions it displays a broad blue-green emission band [1]. Despite the actual use of doped barium aluminate in optoelectronic devices, however, structural investigations remained rare up to now. Therefore we have conducted X-ray absorption measurements for Eu-doped $BaAl_2O_4$ at the L_3 absorption edge of the Eu dopant, as well as at the L_3 absorption edge of Ba for both pure and Eu-doped $BaAl_2O_4$, in order to determine the valence states of Eu and Ba in these cases, and to elucidate the structure of Eu-doped $BaAl_2O_4$ in addition to X-ray diffraction studies. It is expected that obtained results will help to understand the photoluminescence properties of Eu-doped barium aluminate.

Powder samples of pure $BaAl_2O_4$ and one doped with 4.9 at.% Eu in relation to barium were prepared by a hydrothermal method and subsequent annealing at 1100 °C for 4h [2]. The prepared Eu-doped sample exhibited red photoluminescence under excitation with laser light of 308 nm wavelength. The transmission mode Eu and Ba L_3-edge X-ray absorption experiments of the prepared samples were performed at DELTA beamline 10 [3], using ionization chambers for measuring the incident and transmitted intensities, and employing the Si(111) channel-cut monochromator.

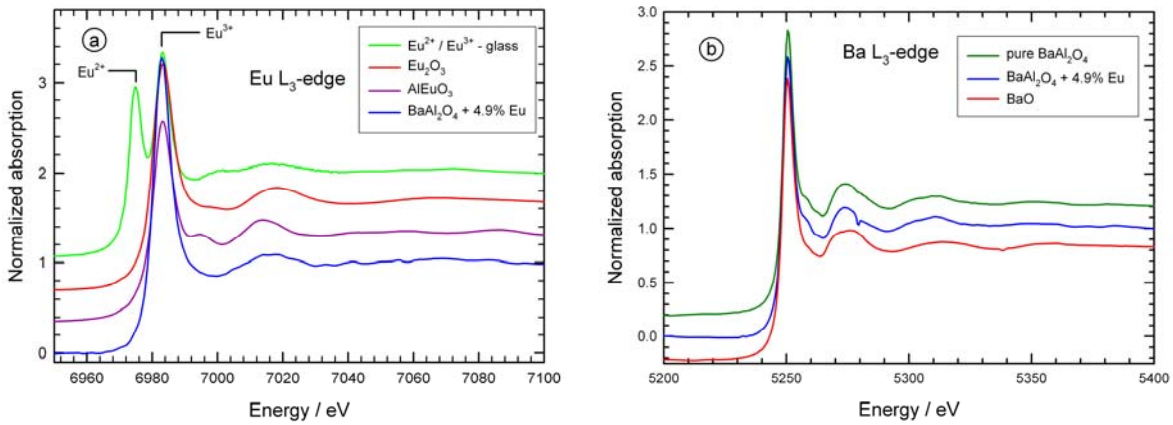

Fig. 1. (*a*) Comparison of the XANES spectra at the Eu L_3-edge of Eu-doped $BaAl_2O_4$ and the Eu-reference compounds Eu_2O_3, $AlEuO_3$ and an Eu^{2+}/Eu^{3+} containing glass sample. (*b*) Comparison of the XANES spectra at the Ba L_3-edge of pure $BaAl_2O_4$, Eu-doped $BaAl_2O_4$ and BaO.

In Fig. 1(a), the normalized Eu L_3-edge XANES spectrum of $BaAl_2O_4$ doped with 4.9 at.% Eu is compared to the spectra of Eu_2O_3 and $AlEuO_3$, used as references for Eu^{3+}, and to the one of a glass sample containing both Eu^{2+} and Eu^{3+} in approximately equal amounts [4]. As can be seen, Eu^{2+} leads to a strong white line feature at about 6975 eV, while Eu^{3+} reveals a white line at a substantially higher photon energy of 6983 eV [4], so that a discrimination of Eu^{2+} and Eu^{3+} appears to be straightforward. Accordingly, the Eu_2O_3 and $AlEuO_3$ references show a strong absorption maximum at about 6983.5 eV. The white line feature of the Eu-doped $BaAl_2O_4$ sample at 6983.4 eV thus clearly reveals the presence of trivalent europium in the doped sample, in contrast to the observations with strong indications for Eu^{2+} [1]. It is also noteworthy that the XANES features of Eu_2O_3, $AlEuO_3$ and of Eu-doped $BaAl_2O_4$ are substantially different in terms of their post-edge features. In particular, the XANES spectrum of Eu_2O_3 has a pronounced post-edge peak at 7020 eV. This peak is shifted to significantly smaller energies for Eu-doped $BaAl_2O_4$ (7016 eV) and $AlEuO_3$ (7012 eV). Eu_2O_3 and $AlEuO_3$ reveal the second absorption maximum in the high energy tail of the white line at about 6995-6998 eV, which however is absent in Eu-doped $BaAl_2O_4$. Finally, the white line intensity of Eu-doped $BaAl_2O_4$ is substantially larger than for the two reference samples, indicating different atomic environments around europium for the three considered samples. This is of a special interest, because the presence of $AlEuO_3$ cannot completely be excluded on the basis of X-ray diffraction measurements (not shown here).

The Ba L_3-edge measurements (Fig. 1(b)) also reveal that the host material remains in its original Ba^{2+}-state; the white line position and intensity is very similar to that of divalent Ba^{2+} in BaO. These data also prove that the structure of the host lattice is not substantially affected by the Eu-doping. Furthermore, the absorption spectrum of BaO reveals different absorption features, so that $BaAl_2O_4$ transformation to BaO accompanied by formation of Al_2O_3 can be excluded here.

In conclusion, the presented XANES spectra at the Eu L_3-edge clearly show that the photoluminescence of Eu-doped $BaAl_2O_4$ in the red spectral range is caused by the presence of Eu^{3+} ions in the host lattice, the retained structure of which is confirmed by Ba L_3-edge measurements. Furthermore, the presence of impurity phases in our Eu-doped sample such as Eu_2O_3, $AlEuO_3$ and BaO can be excluded. In order to elucidate the structure and the environment of the Eu^{3+}-dopant in more detail, the results of additional EXAFS experiments will be presented in a separate contribution.

Acknowledgements

We gratefully acknowledge the DELTA machine group for providing synchrotron radiation reliably.

References

[1] M. Peng, G. Hong. J. Luminescence 127 (2007) 735.
[2] M. Vrankić, PhD-thesis, University of Zagreb, Croatia (2014).
[3] D. Lützenkirchen-Hecht, R. Wagner, S. Szillat, A.K. Hüsecken, K. Istomin, U. Pietsch, R. Frahm. J. Synchrotron Rad. 21 (2014) 819.
[4] C. Paßlick, O. Müller, D. Lützenkirchen-Hecht, R. Frahm, J.A. Johnson, S. Schweizer. J. Appl. Phys. 110 (2011) 113527.

XAS investigations of Eu-doped $BaAl_2O_4$. Part 2: EXAFS experiments

D. Lützenkirchen-Hecht[a], B. Gržeta[b], M. Vrankić[b], S. Bosnar[c], A. Šarić[b], D. Petrov[d], R. Wagner [a]

[a]*Fk. 4-Physik, Bergische Universität Wuppertal, Gaußstr. 20, 42097 Wuppertal, Germany*
[b]*Division of Materials Physics, Ruđer Bošković Institute, Bijenička cesta 54, 10000 Zagreb, Croatia*
[c]*Division of Materials Chemistry, Ruđer Bošković Institute, Bijenička cesta 54, 10000 Zagreb, Croatia*
[d]*Department of Physical Chemistry, Plovdiv University, Tsar Asen Str. 24, 4000 Plovdiv, Bulgaria*

According to XANES experiments at the Eu L_3-edge, Eu-doping of barium aluminate $BaAl_2O_4$ resulted in the presence of Eu^{3+} ions in the host host lattice [1], giving rise to photoluminescence in the red spectral range [2] in contrast to the blue-green emission characteristic for Eu^{2+} ions [2]. The XANES experiments also indicated that the coordination of Eu in the Eu-doped $BaAl_2O_4$ is different from that in the Eu-containing reference compounds such as Eu_2O_3 and $AlEuO_3$, which suggested that the detailed structure needs to be investigated. Therefore we undertook EXAFS investigations in order to study the local environment of the Eu^{3+}-dopant in detail. For this purpose, EXAFS experiments at the Ba (5247 eV) and Eu (6977 eV) L_3-edges have been performed at DELTA beamline 10, making use of the Si(111) channel-cut monochromator and ionization chambers as detectors for the incident and transmitted X-rays [3]. The extraction of the EXAFS fine structure, $\chi(k)$, was done after intensity calibration and background subtraction, and the k^2- or k^3-weighted EXAFS data were fitted with suited model structures using phases and amplitude functions generated by FEFF [4] using the Athena/Artemis software package [5].

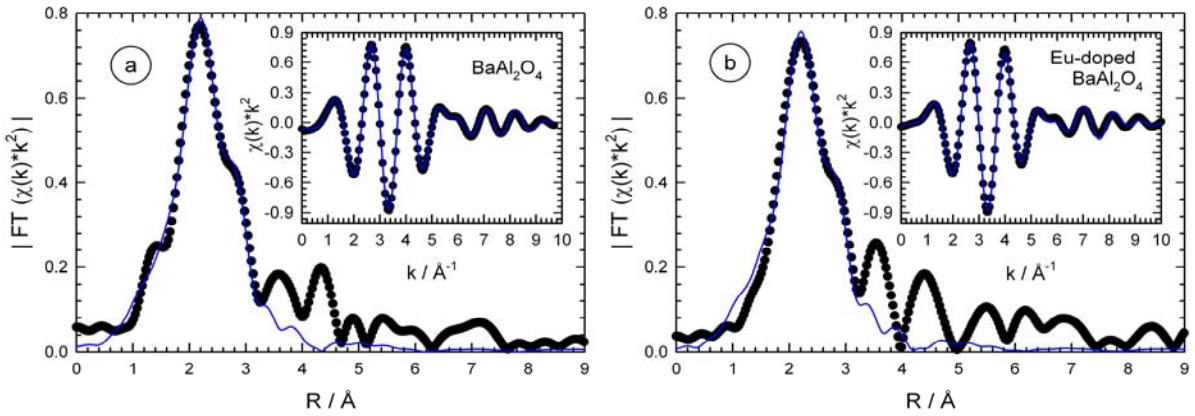

Fig. 1. Fitting result for EXAFS data at the Ba L_3-edge of (*a*) pure $BaAl_2O_4$ and (*b*) $BaAl_2O_4$ doped with 4.9% Eu. The k-range for the Fourier-transform and the fit were 1.28 $Å^{-1}$ < k < 8.78 $Å^{-1}$ and a radial distance 1.58 Å – 3.22 Å was used. Two oxygen and two aluminium shells were used to model the data.

In the fitting procedure of EXAFS data at the Ba L_3-edge, fits comprising two oxygen nearest neighbour shells with 6 oxygen atoms at about 2.7 Å and 3 oxygen atoms at about 2.95 Å, and 3 aluminium atoms at 3.4 Å and 3.5 Å fit the experimental data well for both the pure $BaAl_2O_4$ and $BaAl_2O_4$ doped with 4.9% Eu, as can be seen in Fig. 1. These results confirm that the local structure of the pristine $BaAl_2O_4$ with 9 oxygen atoms in the first coordination sphere is retained during Eu-doping. Furthermore, slightly increased bond lengths for the doped material agree qualitatively within the fit uncertainties with results of X-ray diffraction study for those two samples.

While the EXAFS measurements are relatively straightforward at the Ba L_3-edge of the host material, the investigations at the L_3-edge of the Eu-dopant are challenging because of the low Eu concentration. Therefore, several scans were measured and averaged in order to obtain a data quality that is sufficient for a quantitative data analysis and EXAFS fitting. In Fig. 2, the magnitude of the Fourier-transform of the k^3-weighted EXAFS fine structure, $|FT(\chi(k)*k^3)|$, measured at the Eu L_3-edge is compared to the fitted EXAFS data of Eu_2O_3 and $AlEuO_3$ references.

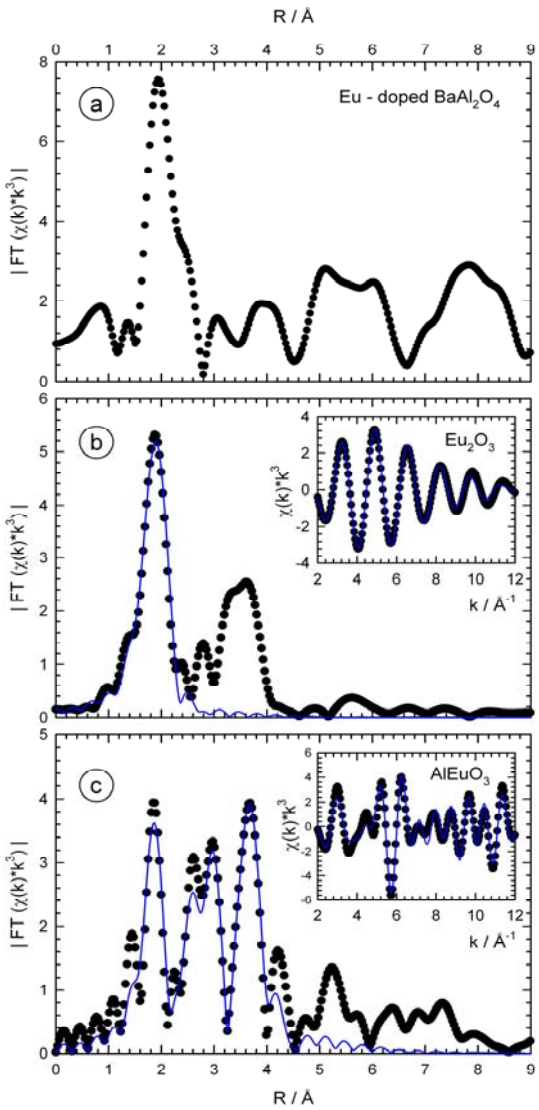

Fig. 2. *(a)* Magnitude of the Fourier-transform of the k^3-weighted EXAFS fine structure $|FT(\chi(k)*k^3)|$ for Eu-doped $BaAl_2O_4$ at the Eu L_3-edge. *(b)* Experimental $|FT(\chi(k)*k^3)|$ (•) and fit (—) for Eu_2O_3. *(c)* Experimental $|FT(\chi(k)*k^3)|$ (•) and fit (—) for $AlEuO_3$. The insets in *(b)* and *(c)* depict the filtered and back-transformed data, as well the respective fits. The k-range for the Fourier transform is 1.7 $Å^{-1}$ < k < 11.8 $Å^{-1}$, and the R-range for the back-transform into k-space and fitting is 1.25 Å < R < 2.56 Å for Eu_2O_3 and 1.3 Å < R < 4.8 Å for $AlEuO_3$.

It is obvious that the radial distribution functions of Eu-doped $BaAl_2O_4$ in Fig. 2(a) and those of Eu_2O_3 and $AlEuO_3$ differ substantially. This agrees with the conclusions from the XANES data, that no substantial amounts of Eu_2O_3 and $AlEuO_3$ are present in the doped samples. Furthermore, comparing Fig. 2(a) and Fig. 1, the shape of the radial distribution functions for the Eu-doped sample obtained at the Ba L_3- and the Eu L_3-edge are quite similar, which suggests that the short range order structure around Ba and Eu are very similar. Thus it is likely to assume that Eu is substituted for Ba in the $BaAl_2O_4$ host lattice. A quantitative fitting of the data using the structure of $BaAl_2O_4$ is currently under way, and results will be published soon.

Acknowledgement

We gratefully acknowledge the DELTA machine group for providing synchrotron radiation reliably.

References

[1] D. Lützenkirchen-Hecht, B. Gržeta, M. Vrankić, S. Bosnar, A. Šarić, D. Petrov, R. Wagner, DELTA annual report (2016) 91.
[2] M. Peng, G. Hong. J. Luminescence 127 (2007) 735.
[3] D. Lützenkirchen-Hecht, R. Wagner, S. Szillat, A.K. Hüsecken, K. Istomin, U. Pietsch, R. Frahm. J. Synchrotron Rad. 21 (2014) 819.
[4] A.L. Ankudinov, B. Ravel, J.J. Rehr, S.D. Conradson. Phys. Rev. B 58 (1998) 7565.
[5] B. Ravel, M. Newville. J. Synchrotron Rad. 12 (2005) 537.

Investigation of Ce speciation in zirconolite glass ceramics for UK plutonium disposition

Stephanie M. Thornber, Martin C. Stennett, and Neil C. Hyatt.

NucleUS Immobilisation Science Laboratory, Department of Materials Science and Engineering, The University of Sheffield, Mappin Street, Sheffield, S1 3JD, UK.

Scientific motivation

The UK holds a stockpile of more 120 tons of separated civil plutonium, which will increase to over 140 tons at the end of nuclear fuel reprocessing in 2020. Up to 10% of this stockpile is likely to be declared as waste since it is unsuitable for fabrication as mixed $(U,Pu)O_2$ fuel for use in light water reactors (due to contamination by Fe, Cr, Am, Cl). We are currently developing glass-ceramic materials for immobilisation of this waste plutonium. In these materials, a crystalline ceramic phase, $CaZrTi_2O_7$ – zirconolite, incorporates Pu in solid solution by crystallisation from an alumina-silicate glass phase which incorporates the associated contaminants. Using CeO_2 as a PuO_2 surrogate, we have investigated the partitioning of Ce between glass and ceramic phase(s) present. The phases present depend both on the glass formulation and which crystallographic site in the zirconolite structure is targeted as the host for the Ce. Ce L_3 X-ray Absorption Spectroscopy (XAS) was used to understand the effect of Ce speciation and local co-ordination environment on partitioning of Ce within these glass-ceramic systems.

Experimental

All samples were batched with the same starting formulation, comprising 30 wt% glass of target composition $Na_2Al_2Si_6O_{16}$, with 70 wt% ceramic forming oxides. The sample matrix investigated the success of Ce incorporation on the Ca and / or Zr sites. The stoichiometry of the ceramic phase for each sample targeted either Ce^{4+} substitution on the Ca^{2+} site (sample A), Ce^{3+} on the Ca^{2+} and Zr^{4+} sites (sample B), or Ce^{4+} substitution on the Zr^{4+} site (sample C). The formulation of sample A, required Al^{3+} substitution on the Ti^{4+} sites for charge compensation, for which additional Al_2O_3 was added. The formulation of sample B did not necessitated charge compensation. In the formulation of sample C, charge compensation was designed to be achieved by equimolar substitution of Ca^{2+} / Ce^{3+} and Zr^{4+} / Ce^{3+}. Table 1 lists the formulations for each sample.

Table 1: All samples consist of 30 wt% glass $Na_2Al_2Si_6O_{16}$. Target zirconolite stoichiometries, Ce oxidation states and relevant wt % of each oxide are given.

Sample	Target ceramic composition	Weight percent of Oxides (wt%)							Target Ce oxidation state
		SiO_2	Na_2O	Al_2O_3	CaO	ZrO_2	TiO_2	CeO_2	
A	$Ca_{0.8}Ce_{0.2}ZrTi_{1.6}Al_{0.4}O_7$	20.62	3.55	9.90	8.95	24.60	25.51	6.87	4+
B	$Ca_{0.9}Ce_{0.1}Zr_{0.9}Ce_{0.1}Ti_2O_7$	20.62	3.55	5.83	9.98	21.93	31.59	6.81	3+
C	$CaZr_{0.8}Ce_{0.2}Ti_2O_7$	20.62	3.55	5.83	11.25	19.78	32.06	6.91	4+

Powder samples were prepared by milling the starting precursors which were then calcined at 600 °C before being packed into stainless steel cans and hot isostatically pressed (HIPed). Representative material was recovered from the HIP cans, powdered, and prepared into transmission samples for measurement at the Ce L_3 absorption edge. The powdered material was dispersed into a polyethylene glycol matrix and cold uniaxially pressed to yield thin but strong pellets; the exact quantity of specimen powder to achieve one absorption length was used. Data was also acquired on a range of standard materials to assist in finger-printing of the Ce oxidation state and coordination environment. Analysis was performed using the Athena and Artemis suite of programs. The X-ray absorption near edge structure (XANES) was analysed to qualitatively identify and compare characteristic features to infer the average Ce oxidation states and co-ordination environment.

Results

The glass-ceramic stoichiometries targeted Ce incorporation on either the Ca^{2+} site as Ce^{4+}, the Zr^{4+} site as Ce^{4+}, or both the Ca^{2+} and Zr^{4+} sites as Ce^{3+} (samples A, B and C, respectively). Ce L_{III} edge XANES spectra of Ce^{3+} (e.g. $CePO_4$ with the monazite structure) and Ce^{4+} (e.g. CeO_2) species are characterised by a white line comprising one and two intense features, respectively. The Ce L_3 XANES data compared with the standards (figure 1) shows clear contributions in the white line from both Ce^{3+} and Ce^{4+} in all samples. The glass-ceramic stoichiometries chosen targeted Ce incorporation on either the Ca^{2+} site as Ce^{4+}, the Zr^{4+} site as Ce^{4+}, or both the Ca^{2+} and Zr^{4+} sites as Ce^{3+} (samples A, B and C, respectively). Sample A showed a predominance of Ce^{4+}, whilst samples B

and C showed a predominance of Ce^{3+}. Observation from X-ray diffraction (XRD) and scanning electron microscopy (SEM) showed that the stronger Ce^{3+} signal in samples B and C correlated with the formation of a Ce-bearing perovskite phase in the samples, $(Ca,Ce)TiO_3$. Ce^{3+} has a similar ionic radius to Ca^{2+} and thus can reside in the 12-fold coordinated A-site in the perovskite structure. The formation of perovskite is favourable over Ce^{3+} substitution into the Zr site in the zirconolite structure ($CaZrTi_2O_7$) which has an ionic radii mismatch of ca. 37%. The predominance of Ce^{4+} and lack of perovskite formation in sample A confirmed retention of Ce^{4+} in the sample and successful incorporation of Ce into zirconolite.

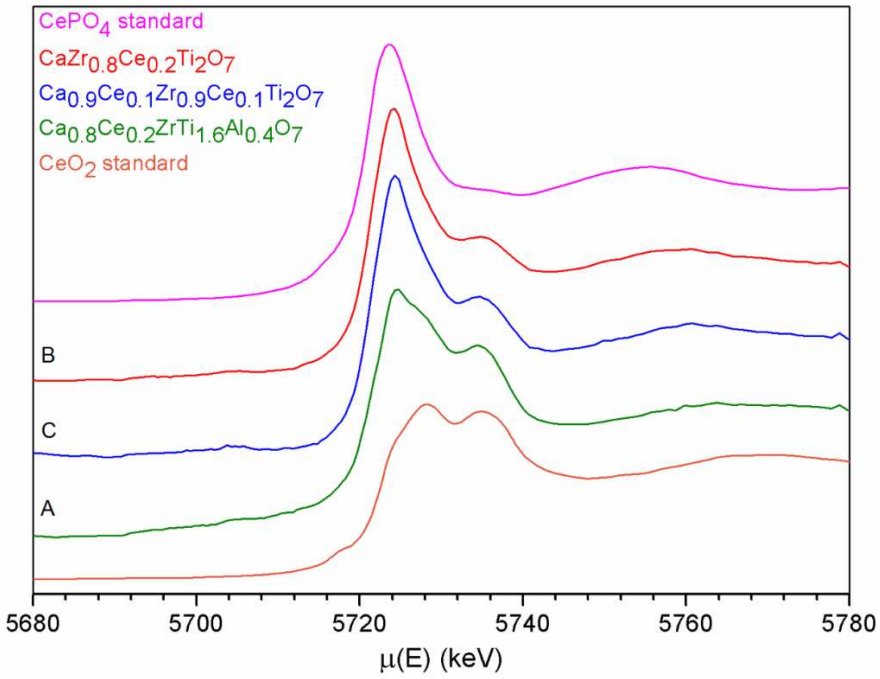

Figure 1: Ce L_3 edge spectra from glass ceramic samples given in Table 1 and reference standards.

Scientific output

We expect that the experiment will produce at least one full good quality journal paper (e.g. submitted to J. Nucl. Mater. or Int. J. Appl. Glass Sci.). This experiment will contribute data to the PhD thesis of co-experimenter Ms. Stephanie Thornber, who has fabricated and characterised the samples to be studied. She was present at the experiment to learn practical data acquisition skills; this has allowed her to apply the theoretical understanding developed through taught courses at the University of Sheffield.

EXAFS investigations of Niobium processing in N_2-atmospheres

J. Kläs, R. Wagner, R. Frahm, D. Lützenkirchen-Hecht

Fakultät 4-Physik, Bergische Universität Wuppertal, Gaußstr. 20, 42097 Wuppertal, Germany

Many treatments of metals and alloys are conducted at high temperatures, employing various gases in order to obtain tailored properties of the materials. In particular, niobium metal may be exposed to N_2 for T > 800°C leading to NbN surfaces layers depending on the temperature [1]. Such an approach has been successfully used for high-temperature nitriding of superconducting Nb-cavities used in accelerator structures, leading to substantially improved RF-superconductivity in mid acceleration fields recently [2]. While electrical and especially superconducting properties have intensively been investigated in the past (see, e.g. [1, 2]), structural studies are rare up to now, and no in-situ experiments have been conducted so far. We have therefore realized a dedicated processing chamber for this BMBF-funded research project (see Fig. 1). The chamber is equipped with a turbomolecular pump and a ceramic heater with several heat shields to enable temperatures of up to 1200 °C under a base vacuum pressure of 10^{-6} mbar. Large Kapton windows cooled with compressed air are used as X-ray windows for the incident, transmitted and scattered radiation and X-ray fluorescence measurements, and process gas (usually high-purity N_2) is introduced via a fine leak valve. The upper part of the chamber is water-cooled to withstand high temperatures and nitrogen-containing gas atmospheres. Promising results have already been obtained during the first experiments with synchrotron radiation.

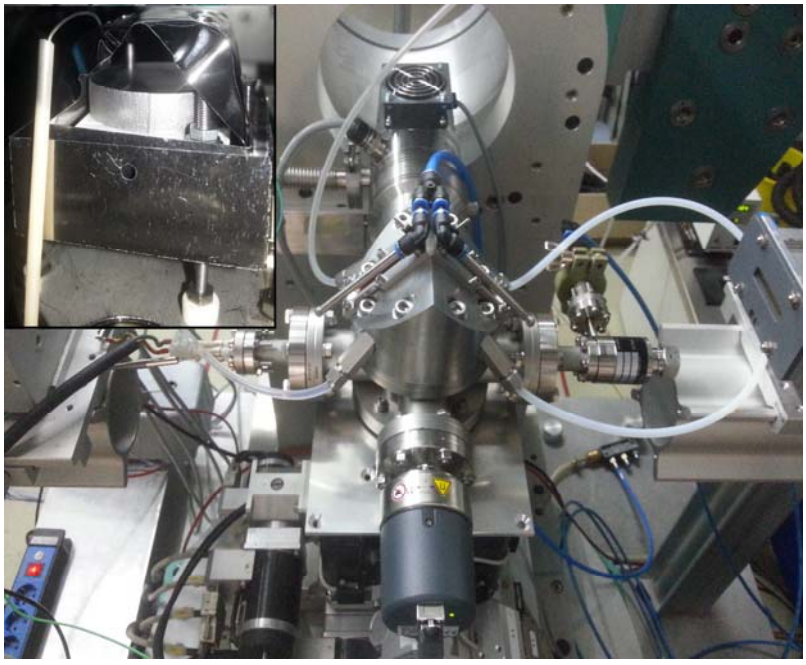

Fig. 1: Photo of the processing chamber mounted on top of the positioning stages on the diffractometer at DELTA BL8. The chamber features a ceramic heater with heat shields to provide temperatures of up to 1200 °C. The upper, water-cooled part of the chamber is equipped with two large-area Kapton windows for incident and scattered X-rays. Compressed air is used to cool the windows. The inset of the figure shows the heater with temperature sensor, heat shielding and a polished Nb sample ready for processing. Vacuum is generated by a turbo molecular pump and the Nitrogen gas quantity is controlled by fine leak valves.

The first experiments were performed with niobium foils which were heated up to 900 °C under vacuum conditions for about an hour until pressure levels in the chamber have recovered, followed by N_2 gas exposure for different periods of time. The samples were investigated with transmission mode EXAFS at the Nb K-edge (18986 eV) making use of the Si(311)-monochromator at BL8. The Nb-samples were measured in-situ at high temperatures as well as after subsequent cooling to liquid nitrogen temperature. Fig. 2 displays the influence of different processing times on the absorption fine structure of Nb foils measured in transmission geometry after processing at 900 °C in an N_2 atmosphere of $5x10^{-3}$ mbar, and cooling to liquid nitrogen temperature (77 K) for the EXAFS measurements. An irreversible decrease in amplitude with time is obvious for all coordination shells, as well as a slight shift of the peaks to higher radial distances can be observed. The latter effect seems to be strongest for the third shell peak at about 3.6 Å radial distance. Taking into account the

bcc crystal structure of Niobium, one may expect interstitial nitrogen atoms occupying vacancies in the scattering path of the third shell. This may give reason for the third shell to be most sensitive.

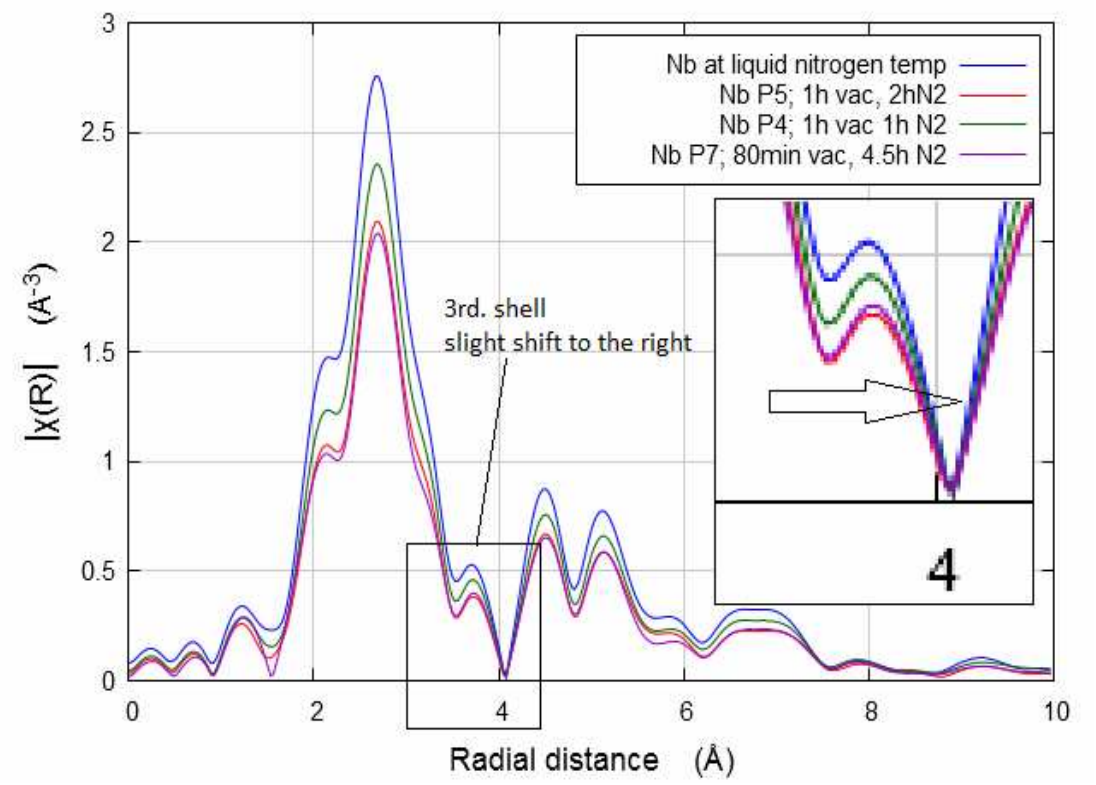

Fig. 2: Magnitude of the Fourier-transform of the k^3-weighted EXAFS fine structure oscillations $|FT(\chi(k)*k^3)|$ for Nb-metal foils of 25 μm thickness heat-treated in N_2-gas atmospheres ($5x10^{-3}$ mbar) at 900 °C for various times as indicated. K-range for the Fourier-transform 1.8 $Å^{-1}$ < k < 15 $Å^{-1}$.

Fitting of the data was performed using metallic Nb structure parameters for the first 5 shells in a cluster containing about 58 atoms, with free running fit parameters for path length and disorder parameters. Good agreement between the experimental data and the fit can be achieved up to a radial distance of about 6 Å for all N_2-treatments, however, the third peak at about 3.7 Å is in general hard to model quantitatively by the fits, especially after prolonged heating for 2 hours and more. To be able to analyse the shift and the reduction of the third shell more precisely, appropriate structure models including nitrogen on different positions in the Nb lattice for fitting the data will be tested in the future.

Acknowledgement

We gratefully acknowledge the DELTA machine group for providing synchrotron radiation reliably.

References

[1] P. Dhakal, et al, Phys. Rev. Special Top. Acc. Beams 16 (2013) 42001
[2] A. Grasselino, A. Romanenko, D. Sergatskov, et al., Supercond. Sci. Technol. 26 (2013) 102001

Notes

Notes